Axion Like Particles Production via Photon Fusion at Belle II

Dipartimento di Matematica e Fisica
Dottorato di Ricerca in Fisica (XXXV cycle)

Alessio Mastroddi
ID number

Advisor
Prof. Roberto Franceschini

Academic Year 2022/2023

Thesis not yet defended

Axion Like Particles Production via Photon Fusion at Belle II
PhD thesis. Roma Tre University of Rome

This thesis has been typeset by LaTeX and the Sapthesis class.

Author's email: alessio.mastroddi@uniroma3.it

Abstract

We consider an axion-like particle produced via Vector Boson Fusion (VBF) at Belle2 in both its possible decay states, visible and invisible. We start from a theoretical tractation of the VBF, computing the full cross section and comparing it to the Equivalent Photon Approximation (EPA) in order to check its goodness. We find that usual methods of integration via polar coordinates are insufficient for a fully analytical calculation, so we refer to the technique of Gram Determinants. Once all properties of EPA and VBF are studied, we put them to use in the phenomenological section. Firstly we consider the visible decay channel for the ALP $a \to \gamma\gamma$. In this case the detector acceptance at Belle II is too small for the VBF to be competitive; we then propose a simple upgrade to the detector, allowing for mostly collinear leptons to be visible, which greatly improves the sensitivity to a VBF produced ALP decaying into photons. Finally, we consider the invisible decay channel, proposing a nearly background-free search. This search leverages dedicated kinematic variables, whose behaviour and performance we test under a simplified, yet realistic, treatment of detector effects. We find that at the Belle II experiment the e^+e^- + invisible channel has the potential to be as sensitive as mono-γ for all the ALP mass range that can be probed by Belle II and can significantly improve the bounds expected for O(GeV) ALP mass. This demonstrates that new searches based on high signal purity channels can give comparable or better bounds than searches based on more traditional large-background final states.

Contents

Chapter 1

Introduction

1.1 Beyond the Standard Model

The discovery of the Higgs boson in 2012 [1, 2] marked a crucial point for our comprehension of elementary particle physics. The observation of a scalar resonance by the experiments ATLAS and CMS has been another confirmation of the Standard Model (SM) [3, 4, 5], and completed the picture of one of the most successful theories in particle physics. There are, however, still questions that remain unanswered within the SM. Some of those come from experimental results, most notably the nature of Dark Matter, that composes the vast majority of all matter content of the universe, or the neutrino masses, which are predicted to be zero in the SM. Some other are more theoretical, regarding unsatisfactory explanations for the values of some observables; some examples are the hierarchy problem, referring to the unexplained strong hierarchy of fermion masses, and the strong CP problem, which will be discussed in the following subsection.
Whichever the reason, it is clear that the SM is not the end of the story: these shortcomings are strong hints that New Physics (NP) is needed; the absence of any signals from the LHC points to this NP living at very high energies, or being very weakly coupled to the SM, or both.

In this thesis we will study the production of Axion Like Particles (ALP) at Belle II, in Japan. We will investigate if the Vector Boson Fusion (VBF) production channel is justifiably neglected in current literature, and we will propose new results for the exclusion bounds of the ALP couplings in both the visible and invisible decay. More in detail, section 1.2 will be dedicated to a concise introduction and to the motivations for using ALPs in our SM extension; in chapter 2 we will discuss the validity of the Equivalent Photon Approximation and how the properties of VBF reflect on ALP production processes; in chapters 3 and 4 we respectively consider the case of an ALP decaying into visible SM particles or invisible particles (possibly Dark Matter).

1.2 Axions and Axion-Like Particles

In order to describe the axion properties, one needs to understand why the axion was proposed in the first place. The so called strong CP problem stems from the

apparent absence, in the SM lagrangian, of the CP violating term

$$\mathcal{L}_{\not{C}\not{P}} \supset \theta \frac{g_s^2}{32\pi^2} G^{a,\mu\nu} \tilde{G}^a_{\mu\nu}, \tag{1.1}$$

where $G^a_{\mu\nu}$ is the gluon field strength, g_s is the strong coupling and θ is a parameter determining the strength of this CP violating term. Since this operator contributes to the electric dipole moment of the neutron [6], one can estimate the value of θ in the SM from the measure of the neutron electric dipole moment (EDM), finding $\theta < 10^{-10}$. Since θ is a free parameter, there is no "natural" explanation for its smallness.

A possible solution to the strong CP problem comes from the axion. We will not give here a full review of the history and the properties of this particle, since it goes beyond our goal; we will instead quickly show its main properties and explain why this kind of particle is especially interesting. For the interested reader, some complete reviews are [7, 8].

The axion was first proposed by Peccei and Quinn in [9] as pseudo-Goldstone bosons of a spontaneously broken $U(1)_{PQ}$ symmetry. This particle could dinamically solve the strong CP problem in QCD [10, 11], hence why it is also referred to as the QCD-axion. In short, the effective lagrangian of the axion field is

$$\mathcal{L}_a = \frac{1}{2}(\partial_\mu a)^2 + \mathcal{L}(\partial_\mu a, \psi) + \frac{g_s^2}{32\pi^2} \frac{a}{f_a} G\tilde{G}, \tag{1.2}$$

where we have the usual kinetic term, an interaction term between the axion and fermions and an interaction term with gluons. f_a is an energy scale, called the axion decay constant; this lagrangian is endowed with a quasi shift symmetry $a \to a + \kappa f_a$ (more details in [7]), which leaves the action invariant up to the term

$$\delta S = \frac{g_s^2 \kappa}{32\pi^2} \int G\tilde{G}. \tag{1.3}$$

Since κ is a free parameter, it can be chosen to remove the θ term of the SM lagrangian, thus solving dinamically the strong CP problem.

From chiral perturbation theory, one is also able to find the predicted value of the axion mass [10], namely

$$m_a \sim 5.7 \left(\frac{10^{12}\ \text{GeV}}{f_a} \right) \mu\text{eV}. \tag{1.4}$$

From its inception, a number of different axion models were proposed, the most important of which are the Kim [12] Shifman-Vainshtein-Zakhariv [13] (or KSVZ) and the Dine-Fischler-Srednicki [14] Zhitnitsky [15] (or DFSZ) models. The difference in these models only stems from which couplings are allowed to the axion.

The KSVZ model extends the SM with a heavy vectorlike quark $Q = Q_L + Q_R$ and a complex scalar ϕ, singlet under all the SM groups. The KSVZ lagrangian reads

$$\mathcal{L}_{KSVZ} = |\partial_\mu \phi|^2 + \bar{Q} i \not{D} Q - y_Q \bar{Q}_L Q_R \phi - \lambda_\phi \left(|\phi|^2 - \frac{\langle \phi \rangle^2}{2} \right)^2 + \text{ h.c.}, \tag{1.5}$$

where the last term denotes that a spontaneous symmetry breaking by the scalar potential. This lagrangian features the $U(1)_{PQ}$ symmetry

$$\phi \to e^{i\alpha}\phi, \quad Q \to e^{-i\alpha\gamma_5}Q. \tag{1.6}$$

If we write the scalar field ϕ in its non linear realization,

$$\phi = \frac{1}{\sqrt{2}}(v_a + \rho_a)e^{ia/v_a}, \tag{1.7}$$

the axion field a corresponds to the Goldstone mode. One can check that an axial transformation of the type

$$Q \to e^{-i\gamma_5 \frac{a}{2v_a}}Q \tag{1.8}$$

causes a shift in the action which is

$$\delta S_{KSVZ} = \frac{g_s^2}{32\pi^2}\frac{a}{v_a}\int G\tilde{G}, \tag{1.9}$$

exactly what is needed to cancel the θ term. In this model, the axion can only couple to quarks.
The DFSZ model instead includes two Higgs doublets H_u, H_d and a SM singlet complex scalar ϕ. In these model, the axion comes from the diagonalization of the full scalar potential, since in principle the Goldstone modes of all scalars contribute to the physical axion. In fact, one can write the three scalar field in their non linear realization (neglecting radial modes that do not contain the axion) as

$$H_u \supset \frac{v_u}{\sqrt{2}}e^{i\frac{a_u}{v_u}}\begin{pmatrix}1\\0\end{pmatrix}, \quad H_d \supset \frac{v_d}{\sqrt{2}}e^{i\frac{a_d}{v_d}}\begin{pmatrix}0\\1\end{pmatrix}, \quad \phi \supset \frac{v_\phi}{\sqrt{2}}e^{i\frac{a_\phi}{v_\phi}}, \tag{1.10}$$

and one gets for the physical axion [7]

$$v_a^2 = v_\phi^2 + v^2(\sin 2\beta)^2, \tag{1.11}$$

with $v = 246$ GeV, $v_u/v = \sin\beta$, $v_d/v = \cos\beta$. Of course, if $v_\phi \gg v_{u,d}$, the axion basically comes only from ϕ. The axion couplings to fermions is obtained by substituting the non linear forms of the scalars in the Yukawa lagrangian; for this reason, both quark and leptons can couple directly to the axion. For the full details on these models, we point to the reviews in [7, 8].

In all these years of existence, experiments have shut down a large fraction of the parameter space allowed to the axions, as shown in figs. 1.1 and 1.2 [16], mostly due to the fact that its couplings to matter are correlated. In particular, the most common probe to the axion sector, $g_{a\gamma\gamma}$ is related to the axion mass via the relation $g_{a\gamma\gamma} \sim 1/f_a$.

If one takes inspiration from the QCD axion but breaks the correlation between couplings (and does not care about solving the strong CP problem), one can define a new particle, called Axion-Like-Particle (ALP in short). In this case, the ALP lagrangian reads

$$\mathcal{L}_{ALP} \supset \frac{1}{2}M_a^2 a^2 + \frac{g_{a\gamma\gamma}}{4f}aF\tilde{F}, \tag{1.12}$$

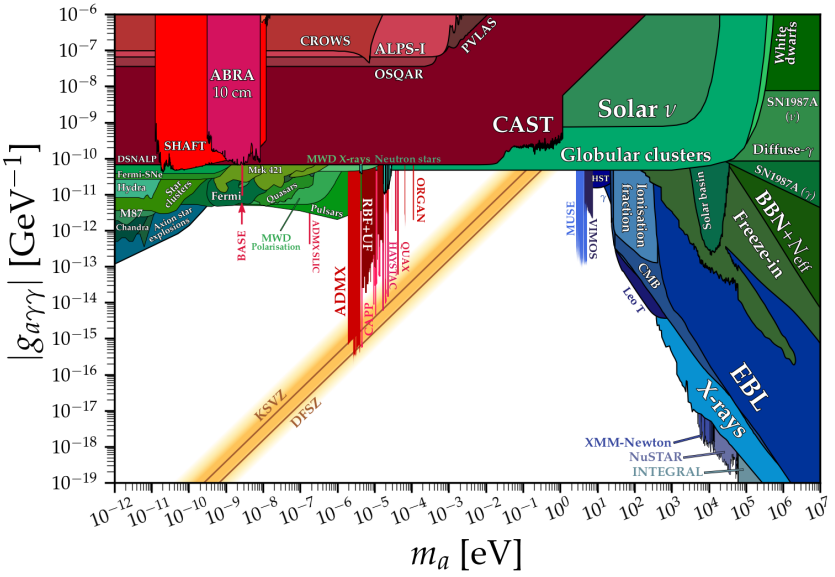

Figure 1.1. Excluded regions for the axion mass m_a and photon coupling $g_{a\gamma\gamma}$ from different experiments [16].

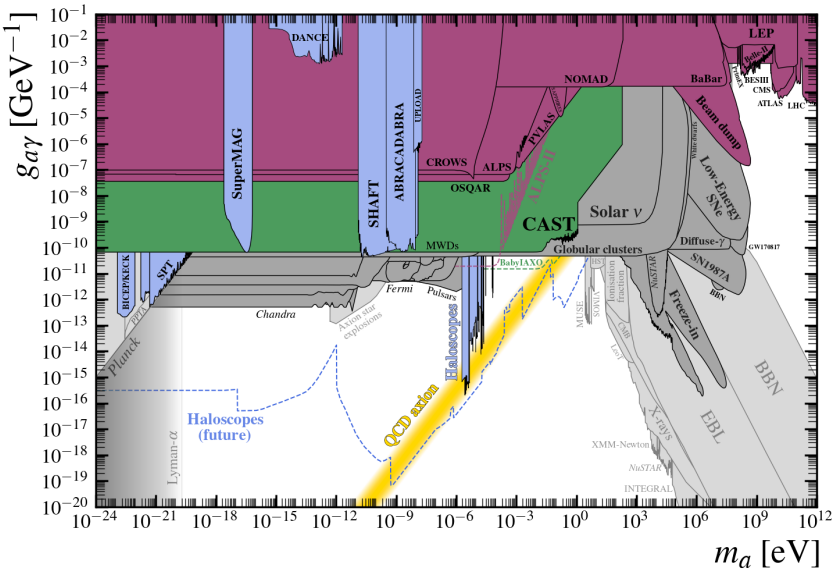

Figure 1.2. Excluded regions for the axion mass m_a and photon coupling $g_{a\gamma\gamma}$ from different experiments with future predicted exclusions [16].

where the ALP mass M_a and the energy scale f are completely unrelated (and different from the axion parameters m_a, f_a).
ALPs retain all the interesting properties of the QCD axion, but it's not constrained in an extremely narrow parameter space; for this reason, ALPs have been part of a lot of different UV completions of the SM. For example, low mass ALPs ($M_a <$ 1MeV) are particularly interesting for cosmology [17], being proposed as a viable cold Dark Matter (DM) candidate [18, 19] or as a portal to a DM particle [20, 21, 22] that can satisfy both freeze-out and direct detection bounds; they can affect Big Bang Nucleosynthesis (BBN) and the Cosmic Microwave Background (CMB) [23]; they have been also proposed to explain how some classes of stars cool down over-efficiently [24]. For higher masses (M_a in the MeV to GeV range), ALPs are mostly irrelevant for astrophysics, but have some interesting applications in particle physics [25, 26, 27, 28, 29, 30, 31, 32, 33], in particular for explaining the anomalous magnetic moment of the muon [32, 34, 35], as a possible solution to the hierarchy problem [36] via the relaxation mechanism, gaining the name *relaxion* [37] . Beyond that range, ALPs also can emerge from string theory [38] or supersymmetric theories [39].

In this work we will consider the same ALP interactions of [40], where the ALP only couples to electroweak gauge bosons. Explicitly, the Lagrangian reads

$$\mathcal{L} \supset \frac{1}{2}\partial_\mu a \partial^\mu a - \frac{1}{2}M_a^2 a^2 - \frac{c_B}{4f_a} a B^{\mu\nu}\tilde{B}_{\mu\nu} - \frac{c_W}{4f} a W_i^{\mu\nu}\tilde{W}^i_{\mu\nu}, \tag{1.13}$$

where

$$\tilde{B}^{\mu\nu} = \frac{1}{2}\varepsilon^{\mu\nu\rho\sigma}B_{\rho\sigma}, \tag{1.14}$$

and analogously for $\tilde{W}^{\mu\nu}$. M_a and f stand for the ALP mass and decay constant, which are independent from one another. This Lagrangian does not contain all of the terms one would expect from a general EFT description of the ALP interactions; however, we will not consider ALP interactions with SM fermions or gluons.[1] Those interactions usually lead to tightly constrained flavour changing processes [20, 33], while ALPs mainly coupled to EW bosons are not. Couplings to the Higgs boson are also not included; those come in the form of dimension 6 operators, which would be already suppressed; moreover, since we will work at Belle II energies ($\sqrt{s} \sim 10$ GeV) those interactions are effectively non-existent.
After electroweak symmetry breaking, the Lagrangian becomes

$$\mathcal{L} \supset -\frac{g_{a\gamma\gamma}}{4} a F^{\mu\nu}\tilde{F}_{\mu\nu} - \frac{g_{a\gamma Z}}{4} a F^{\mu\nu}\tilde{Z}_{\mu\nu} - \frac{g_{aZZ}}{4} a Z^{\mu\nu}\tilde{Z}_{\mu\nu} - \frac{g_{aWW}}{4} a W^{\mu\nu}\tilde{W}_{\mu\nu}, \tag{1.15}$$

with

$$g_{a\gamma\gamma} = \frac{c_B \cos\theta_W{}^2 + c_W \sin^2\theta_W}{f_a}, \quad g_{a\gamma Z} = \frac{\sin 2\theta_W (c_W - c_B)}{f_a}, \tag{1.16}$$

where θ_W is the weak mixing angle. From eq. (1.16), if c_B and c_W are independent parameters, one can find the interesting case $c_B \approx c_W$, which means $g_{a\gamma\gamma} \gg g_{a\gamma Z}$.

[1] This is only true at tree level. Interactions with SM fermions will appear at one loop, and interactions with gluons is generated at two loops. However, these couplings are too small to contribute to our study.

In this case the ALP couples mainly with photons, and this is the situation we will consider throughout this work. For the sake of simplicity, we will also explicitly put $g_{a\gamma Z} = g_{aZZ} = g_{aWW} = 0$. Once again, given the centre of mass energy available at Belle II this approximation is acceptable since Z and W production is effectively 0. The $a\gamma\gamma$ coupling is especially important since it determines the lifetime of the ALP. In our model, in fact, the photon is the only SM particle the ALP can decay to, with its width equal to

$$\Gamma_a = \frac{g_{a\gamma\gamma}^2 M_a^3}{64\pi}. \tag{1.17}$$

It is worth noting that for very small values of $g_{a\gamma\gamma} \ll 10^{-3}$ GeV^{-1} and $M_a \ll 1$ GeV this decay width can become extremely small, meaning that the decay length can become larger than the detector. Using some benchmark values, we can express the ALP decay length in terms of its lifetime as

$$c\tau_a \simeq 0.4 \text{ mm} \left[\frac{1 \text{ GeV}}{m_a}\right]^3 \left[\frac{10^{-5} \text{ GeV}^{-1}}{g_{a\gamma\gamma}}\right]^2 . \tag{1.18}$$

For sufficiently light ALP masses ($\mathcal{O}(0.1 \text{ GeV})$), this distance becomes quickly macroscopic; for reference, the shortest distance between the interaction point and the electromagnetic calorimeter (ECL) at Belle II is about 1 m [41]. That case cannot be included with the $a \to \gamma\gamma$ decay, but will be included in the "invisible" ALP decay (chapter 4). Indeed, we will assume in that case that the ALP is coupled directly to Dark Matter, with a lagrangian of the form

$$\mathcal{L} = \frac{1}{2}(\partial_\mu a)^2 - \frac{m_a^2}{2}a^2 - \frac{g_{a\gamma\gamma}}{4}aF_{\mu\nu}\tilde{F}^{\mu\nu} + \frac{i}{2}\bar{\chi}\gamma^\mu\partial_\mu\chi + \frac{M_\chi}{2}\bar{\chi}\chi + \frac{g_{a\chi\chi}}{2}M_\chi a\bar{\chi}\gamma_5\chi \ , \tag{1.19}$$

where χ, the Dark Matter particle, is a Majorana fermion.

Chapter 2

Validity of EPA

Since the main objective of this work is to investigate the possibility of studying ALP production via Vector Boson Fusion (VBF) at Belle II, we will dedicate this first chapter to review some of the most important properties of such processes, and show some original results in the field of the Equivalent Photon Approximation (EPA).

2.1 EPA state of the art

The Equivalent Photon Approximation is a useful tool that allows to compute scattering amplitudes involving virtual photons emitted by the initial state by approximating them with real photons.
The first appearance of this concept goes all the way back to Fermi [42], who was investigating the excitation and ionization of atoms due to bombardment of high energy electrons. He compared this effect to the effect of shining light onto an atom, which would ionize if the photon frequency was high enough.
Let us briefly review Fermi's results. Consider a particle with electric charge q, moving with velocity $\vec{\mathbf{v}}$; taking a point in space P, we want to compute the spectral distribution of the electric field in P (see image 2.1). For simplicity, let us assume that the particle is moving along the x axis; the minimal distance from the point P will be called b, and we will say that this point will be reached at $t = 0$. After some time t, we can compute the components of the electric field $\vec{\mathbf{E}}$ in P:

$$E_x = \frac{qvt}{(b^2 + v^2t^2)^{3/2}}, \quad E_y = \frac{qb}{(b^2 + v^2t^2)^{3/2}}. \tag{2.1}$$

We can expand E_x and E_y in Fourier series considering times $T/2 \leq t \leq T/2$, with T that will eventually go to infinity. We then get

$$E_x = \sum_{n=0}^{\inf} a_n \sin 2\pi n \tfrac{t}{T}, \quad E_y = \sum_{n=0}^{\inf} b_n \cos 2\pi n \tfrac{t}{T}, \tag{2.2}$$

where

$$a_n = \frac{2qv}{T} \int_{-T/2}^{T/2} \mathrm{d}t \frac{t \sin 2\pi n \frac{t}{T}}{(b^2 + v^2t^2)^{3/2}}, \quad b_n = \frac{2qb}{T} \int_{-T/2}^{T/2} \mathrm{d}t \frac{\cos 2\pi n \frac{t}{T}}{(b^2 + v^2t^2)^{3/2}}. \tag{2.3}$$

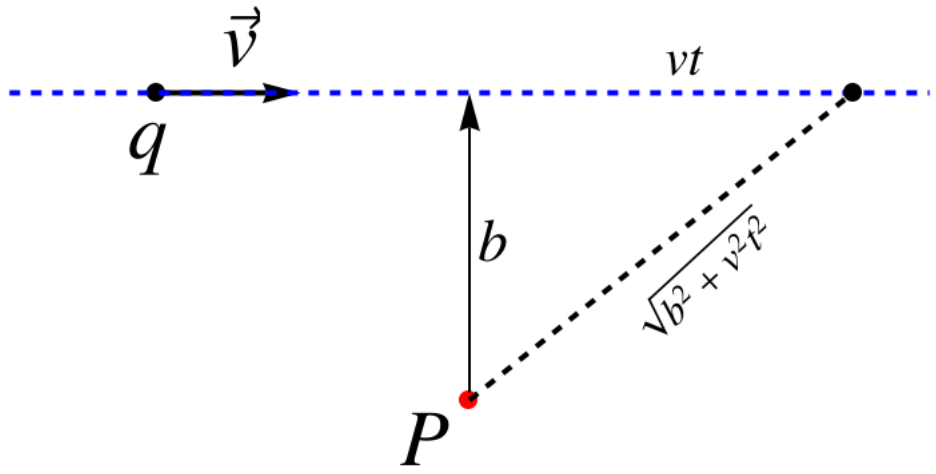

Figure 2.1. A charged particle with electric charge q moving with velocity $\vec{\mathbf{v}}$. b is the smallest distance from the point P.

Fermi noticed that the Fourier decomposition of E_x, the component collinear to the motion of the electrically charged particle, was equal to the electric field of a light wave with intensity $\frac{c}{4\pi}\frac{a_n^2}{2}$ and frequency $\nu = \frac{n}{T}$, and then used this result to compute spectral lines and ionization of various atoms. We will not report those results, but it is important to note that, even with classical calculations, it is possible to approximate the effect of a fast charged particle with the flux of photons distributed in a spectrum of frequencies.
About a decade later, Weizsacker [43] and Williams [44] developed this concept, utilizing it to compute the cross section in interactions of relativistic particles; in their semiclassical calculation, they find the equivalent photon spectrum $n(\omega)$. The same results were then obtained by use of Feynman diagrams [45], and the range of validity of this approximation was discussed at length in [46] by Budnev *et al.* We will now derive explicitly the EPA following this last review. Following the classical presentation, we concentrate on a Deep Inelastic Scattering (DIS) process of the form

$$e^- p \to e^- + X. \tag{2.4}$$

Since EPA treats virtual photons as real, the requirements for this approximation to hold are that the photon is almost on mass shell and that the contribution of the longitudinal polarization to the cross section is negligible. Let us call q the four-momentum of the photon, and define Λ as a process dependent cutoff such that for $|q^2| < \Lambda^2$ the EPA is a good approximation [1]. We can write the cross section of the $e^- p$ scattering as

$$\mathrm{d}\sigma_{ep} = \frac{4\pi\alpha_{\mathrm{EM}}}{4\sqrt{(pP)^2 - p^2P^2}} M^{*\nu} M^{\mu} \frac{\rho^{\mu\nu}}{-q^2} (2\pi)^4 \delta^{(4)}(p + P - p' - K) \mathrm{d}\Gamma \frac{\mathrm{d}^3 p'}{2E'(2\pi)^3}, \tag{2.5}$$

[1] The requirement of $|q^2| < \Lambda^2$ is only there to remind us that the virtuality of the photon should be small for the effective approach to work. Assuming this condition is met, all results do not depend on the explicit value of Λ.

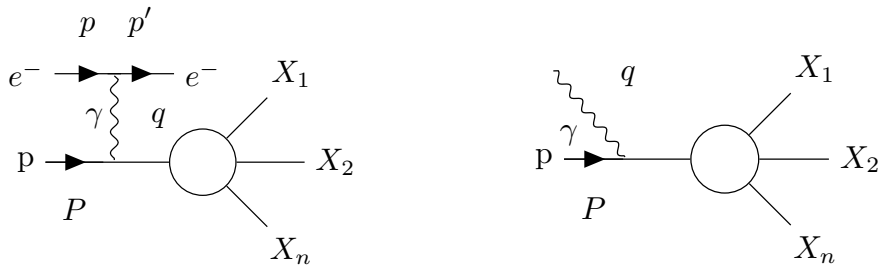

(a) Full process **(b)** Equivalent photon approximation

Figure 2.2. Depiction of the full process of an electron recoiling against a nucleus (left) and the EPA process (right). The virtual photon of the full process is approximated to a real photon that interacts with the nucleus.

where M^μ parametrizes the photon-nucleus interaction, Γ is the phase space of all the produced particles with total momentum K and

$$\rho^{\mu\nu} = \frac{1}{-2q^2}\,\mathrm{Tr}\left[(\not{p}+m_e)\gamma^\mu(\not{p}'+m_e)\gamma^\nu\right] = -\left(g^{\mu\nu}-\frac{q^\mu q^\nu}{q^2}\right)-\frac{(2p-q)^\mu(2p-q)^\nu}{q^2}. \tag{2.6}$$

The cross section in 2.5 is written in a way that makes clear the introduction of the EPA. In fact, one can think of the collision of photons with the protons, and then the number of photons in a volume $\mathrm{d}^3q = \mathrm{d}^3p'$ will be proportional to $\rho^{\mu\nu}\mathrm{d}^3q/q^2$, which is why we refer to $\rho^{\mu\nu}$ in eq. 2.6 as the density matrix of the virtual photon. Integrating out the produced particles, we are left with a tensor $W^{\mu\nu}$ defined as

$$W^{\mu\nu} = \frac{1}{2}\int M^{*\nu}M^\mu(2\pi)^4\delta^{(4)}(q+P+K)\mathrm{d}\Gamma; \tag{2.7}$$

according to the optical theorem, this quantity is the absorptive part of the γp forward amplitude. This tensor can only depend on q^μ, P^μ and $g^{\mu\nu}$; to take gauge invariance ($q^\mu W^{\mu\nu} = W^{\mu\nu}q^\nu = 0$), it is useful to introduce the following linear combinations:

$$Q^\mu = \sqrt{\tfrac{-q^2}{(pP)^2-p^2P^2}}\left[P^\mu - q^\mu\tfrac{(qp)}{q^2}\right],\ q\cdot Q = 0,\ Q^2 = 1; \tag{2.8}$$

$$R^{\mu\nu} = R^{\nu\mu} = -g^{\mu\nu} + \tfrac{(qP)(q^\mu P^\nu + q^\nu P^\mu - q^2P^\mu P^\nu - P^2q^\mu q^\nu)}{(qP)^2-q^2P^2}; \tag{2.9}$$

$$q^\mu R^{\mu\nu} = Q^\mu R^{\mu\nu} = 0. \tag{2.10}$$

$R^{\mu\nu}$ and Q^μ are related to the virtual photon polarizations: in fact, in the γp centre of mass frame, when $\vec{\mathbf{q}} = -\vec{\mathbf{P}}$, we find that

$$\varepsilon(0)^\mu = iQ^\mu, \qquad \varepsilon^{*\mu}(+)\varepsilon^\nu(+) + \varepsilon^{*\mu}(-)\varepsilon^\nu(-) = R^{\mu\nu}(q,P), \tag{2.11}$$

with $\varepsilon(0,\pm)$ respectively the scalar and transverse photon polarizations.
Now we can write

$$\begin{aligned} W^{\mu\nu} &= R^{\mu\nu}W_T(q^2,qP) + Q^\mu Q^\nu W_S(q^2,qP), \\ W_{S,T} &= 2\sqrt{(qP)^2-q^2P^2}\ \sigma_{S,T}\ , \end{aligned} \tag{2.12}$$

where we can explicitly separate the transverse and scalar absorption cross sections. Plugging all this into 2.5, we find

$$\mathrm{d}\sigma = \frac{\alpha_{\mathrm{EM}}}{4\pi^2|q^2|}\sqrt{\frac{(qP)^2 - q^2P^2}{(pP)^2 - p^2P^2}}(2\rho^{++}\sigma_T + \rho^{00}\sigma_S)\frac{\mathrm{d}^3p'}{E'}, \tag{2.13}$$

with

$$2\rho^{++} \quad = \rho^{\mu\nu}R^{\mu\nu} = \tfrac{(2pP-qP)^2}{(qP)^2-q^2P^2} + 1 + \tfrac{4m_e}{q^2}, \tag{2.14}$$

$$\rho^{00} \quad = \rho^{\mu\nu}Q^\mu Q^\nu = 2\rho^{++} - 2 - \tfrac{4m_e}{q^2}. \tag{2.15}$$

In order to understand clearly which is the dominant term in section 2.1, let us make a final change of variable, which is especially useful in the Lab frame (where $\vec{\mathbf{P}} = 0$):

$$\omega = \frac{qP}{m_P}, \quad \mathrm{E} \quad = \frac{pP}{m_P}. \tag{2.16}$$

In the lab frame, in fact, E coincides with the electron energy and ω with the photon energy.
Since $W^{\mu\nu}$ is regular for $q^2 \to 0$, given the definition of Q^μ that is overall proportional to q^μ/q^2, we must impose

$$W_S \propto \sigma_S \sim q^2; \tag{2.17}$$

for small values of q^2, the scalar cross section decreases while the transverse cross section σ_T approaches the real photon absorption cross section. This gives us the opportunity to approximate $\sigma \simeq \sigma_T$ at low q^2. While $|q^2| \ll \omega^2$, from section 2.1

$$2\rho^{++} = \frac{(2E-\omega)^2}{\omega^2} + 1 + \frac{4m_e^2}{q^2}; \tag{2.18}$$

moreover, if we call $q = xp$, where x is the momentum fraction carried by the photon, we also have $\omega = xE$; we can find the dominant term in section 2.1 by introducing x in eq. (2.18):

$$2\rho^{++} = \left(\tfrac{2E}{\omega} - 1\right)^2 + 1 + \frac{4m_e}{q^2} = (2x - 1^2) + 1 + \frac{4m_e^2}{q^2} = 2 + \frac{4m_e^2}{q^2} - 2x + 4x^2, \tag{2.19}$$

and this implies

$$\rho^{00} = 2\rho^{++} - 2 - \frac{4m_e^2}{q^2} = -2x + 4x^2. \tag{2.20}$$

This shows how the transversal term is actually dominant for small x, and we can approximate the ep cross section with that of a real photon interacting with a proton times a probability density function:

$$\mathrm{d}\sigma_{ep} = \sigma_{\gamma p}(\omega)\mathrm{d}n(\omega, q^2), \tag{2.21}$$

$$\mathrm{d}n = \frac{\alpha}{2\pi E^2}\rho^{++}\omega\mathrm{d}\omega\frac{\mathrm{d}\left(-q^2\right)}{|q^2|} = \frac{\alpha}{4\pi E^2}\left[\frac{(2E-\omega)^2}{\omega^2 - q^2} + 1 + \frac{4m^2}{q^2}\right]\frac{\omega\mathrm{d}\omega\mathrm{d}\left(-q^2\right)}{|q^2|}. \tag{2.22}$$

Once again we repeat that this approximation is accurate up to terms of order $\mathcal{O}\left(\frac{|q^2|}{\Lambda^2}\right)$. Integrating over q^2, we get

$$N(\omega)\frac{\mathrm{d}\omega}{\omega} = \int_{q^2_{min}}^{q^2_{max}} \mathrm{d}n(\omega, q^2), \tag{2.23}$$

$$N(\omega) = \frac{\alpha}{\pi}\left[\left(1 - \frac{\omega}{E} + \frac{\omega^2}{2E^2}\right)\ln\frac{q^2_{\max}}{q^2_{\min}} - \left(1 - \frac{\omega}{2E}\right)^2 \ln\frac{\omega^2 + q^2_{\max}}{\omega^2 + q^2_{\min}} - \frac{m_e^2\omega^2}{E^2 q^2_{\min}}\left(1 - \frac{q^2_{\min}}{q^2_{\max}}\right)\right], \tag{2.24}$$

where

$$q^2_{\min} = \frac{m_e^2\omega^2}{E(E-\omega)}\left[1 + \mathcal{O}\left(\left(\frac{m_e^2}{(E-\omega)^2}\right)\right)\right] \leq -q^2 \leq q^2_{\max} \leq 4E(E-\omega). \tag{2.25}$$

The explicit value for $q^2_{\max}$ comes either from the experiment, or is imposed by the hard cutoff Λ.
A more precise treatment of the integration boundary of q^2 was studied in [47]. They trade the electron energy with the quantity

$$y = \frac{P\cdot q}{P\cdot p} = 1 - \frac{P\cdot p'}{P\cdot p}, \tag{2.26}$$

which is just the fraction of longitudinal momentum carried by the photon. Defining θ as the electron deflection angle, knowing that it is small when the EPA is valid, they find

$$q^2 = -\frac{m_e^2 y^2}{1-y} - \frac{E(1+\beta)(A^2 - m_e^2)^2}{4A^3}\theta^2 + \mathcal{O}\left(\theta^4\right), \tag{2.27}$$

with $\beta = \sqrt{1 - 4m_e^2/E^2}$, $A = E(1+\beta)(1-y)$. The integration extrema are now easily found: the value of $q^2_{\max}$ is obtained by taking $\theta = 0$, while $q^2_{\min}$ is obtained when θ equals its maximum value, θ_c. Assuming $\theta_c \ll 1$, we have

$$q^2_{\max} = -\frac{m_e^2 y^2}{1-y}, \tag{2.28}$$

$$q^2_{\min} = -\frac{m_e^2 y^2}{1-y} - E^2(1-y)\theta_c^2 + \mathcal{O}\left(E^2\theta_c^4, m_e^2\theta_c^2, \frac{m_e^4}{E^2}\right). \tag{2.29}$$

We can rewrite eq. 2.22 in terms of y as

$$f_\gamma^{(e)}(y) = \frac{\alpha_{\mathrm{EM}}}{2\pi}\left\{2(1-y)\left[\frac{m_e^2 y}{E^2(1-y)^2\theta_c^2 + m_e^2 y^2} - \frac{1}{y}\right] + \frac{1+(1-y)^2}{y}\log\frac{E^2(1-y)^2\theta_c^2 + m_e^2 y^2}{m_e^2 y^2} + \mathcal{O}\left(\theta_c^2, m_e^2/E^2\right)\right\}. \tag{2.30}$$

This equation can be interpreted as the probability density function of a photon of longitudinal momentum fraction y inside an incoming electron of energy E. We should note that this result was obtained by assuming a collinearity between the incoming and outgoing electron (or the incoming electron and the virtual photon); for this reason we cannot increase *a priori* the critical angle θ_c.

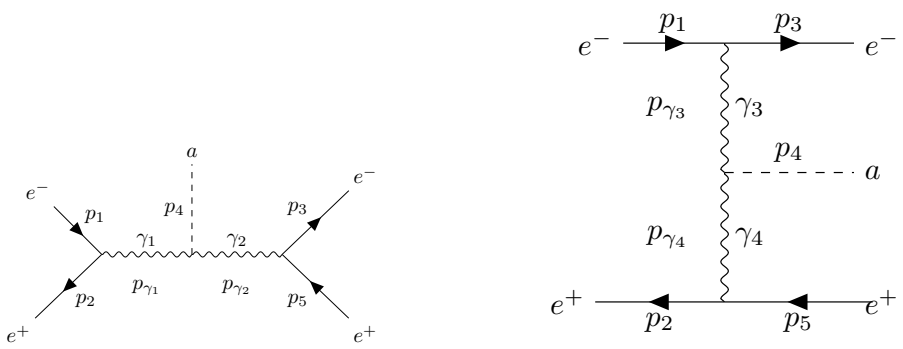

(a) s-channel **(b)** t-channel

Figure 2.3. The two Feynman diagrams involved in the process $e^+e^- \to e^+e^-a$.

2.2 Where does the EPA hold?

We now come to our original contribution to the topic, which is to explore the boundaries of the EPA, and to see exactly when it breaks down, specifically in ALP production. Since we are ultimately interested in ALP production via photon fusion at Belle 2, we will limit ourselves to studying the VBF process $e^+e^- \to e^+e^-a$. In order to see when this approximation stops working, we need to have a handle on the full cross section (hence why we need to specify a process), so that we can compare this result with the one obtained by means of EPA. However, this hypothesis does not depend in any way on the Lorentz nature of the particles involved. In fact, we could assume to have a completely scalar theory, with only trilinear couplings allowed; the diagrams appearing in the process are the same, but now each propagator will be simplified to $\frac{1}{p^2-m^2}$, and the trilinear couplings become dimensional. This trick can be justified also thinking back to the computation by Fermi, of fig. 2.1. In fact, in that case we never needed to impose that the equivalent photon was a spin-1 particle. This choice of only using scalar makes all the computations easier and more concise; in the end, we are not interested in complications, we wanto to explore the properties of the EPA and of collinearity.
Let us call this toy model the "scalar Standard Model" (sSM), and let us compute the ALP production cross section in this simplified setting. In the center of mass reference frame, the initial momenta will be

$$\mathbf{p_1} = \begin{pmatrix} \frac{\sqrt{s}}{2} \\ 0 \\ 0 \\ \frac{\sqrt{s}}{2}\beta \end{pmatrix}, \mathbf{p_2} = \begin{pmatrix} \frac{\sqrt{s}}{2} \\ 0 \\ 0 \\ -\frac{\sqrt{s}}{2}\beta \end{pmatrix}, \beta = \sqrt{1 - \frac{4m^2}{s}}, \tag{2.31}$$

where m denotes the electron mass.
For the outgoing momenta, we can always rotate the axes around the beam direction in order to have one of the outgoing particles with a null component of the momentum in either the x or y direction; the other two particles must be instead the most general ones, with the constraint that the sum of their three-momenta

must vanish due to the conservation of the four-momentum (the initial state is at rest in this reference frame). Since in all our calculation the particle representing the ALP is always integrated away (we are interested in differential cross sections for the final electrons) we write only the final momenta for the final electrons, and the remaining momentum can be obtained from four-momentum conservation:

$$\mathbf{p_3} = \begin{pmatrix} E_3 \\ 0 \\ p_3 \sin\theta_3 \\ p_3 \cos\theta_3 \end{pmatrix}, \ \mathbf{p_5} = \begin{pmatrix} E_5 \\ p_5 \sin\theta_5 \sin\phi \\ p_5 \sin\theta_5 \cos\phi \\ p_5 \cos\theta_5 \end{pmatrix}, \ p_i = \sqrt{E_i^2 - m^2}. \tag{2.32}$$

Now we can write the amplitude for each of the channels (the couplings are left implicit):

$$\mathcal{M}_s = \frac{1}{(\mathbf{p_1} + \mathbf{p_2})^2} \frac{1}{(\mathbf{p_3} + \mathbf{p_5})^2}, \ \mathcal{M}_t = \frac{1}{(\mathbf{p_1} - \mathbf{p_3})^2} \frac{1}{(\mathbf{p_2} - \mathbf{p_5})^2}; \tag{2.33}$$

finally, the cross section will be

$$\sigma = \int \frac{\mathrm{d}^3 p_3}{2E_3} \frac{\mathrm{d}^3 p_4}{2E_4} \frac{\mathrm{d}^3 p_5}{2E_5} \frac{1}{2s(2\pi)^5} |\mathcal{M}|^2 \delta^4(\mathbf{p_{in}} - \mathbf{p_{out}}), \tag{2.34}$$

where $\mathcal{M} = \mathcal{M}_s + \mathcal{M}_t$ and all the couplings are left implicit for ease of notation.
Let's start by considering only the dominant contribution to the total cross section, the t-channel. This diagram represents exactly the process in which the EPA can work; if the produced particle mass is no longer small ($M \lesssim \sqrt{s}$), q^2 becomes larger and larger. This can conflict with the approximation of small q^2, one of the basis of the EPA. For this reason, let us focus on this mass region, to see if there are still collinearity effects. In particular, we want to go to the extreme point, in which the mass of the ALP is so close to the energy threshold that the final state electrons are non-relativistic; if even in this region the collinearity approximation still holds, then we can conclude that there are no problems in using it "carelessly" in all of the phase space.
Suppose then $M_a \sim \sqrt{s}$, or more explicitly, $M_a = \sqrt{s} - 2m(1+\alpha)$: α is basically a measure of how much phase space is left after all the final state is produced at rest. If $\alpha \ll 1$, the ALP is certainly non relativistic (some more precise calculations are needed for the electrons); instead, if we let α grow much larger than 1, we go back to the more usual case of a massive ALP but not necessarily a non relativistic one. Let us restrict to the situation in which $\alpha \ll 1$: of course, since the remaining energy is much smaller than the ALP mass, we can write the non relativistic expansion for the energy of the ALP:

$$E_a = E_4 = \sqrt{p_4^2 + M^2} \approx M + \frac{p_4^2}{2M}. \tag{2.35}$$

Then, when we integrate the three-momentum delta in eq. (2.34), we will have $\vec{\mathbf{p_4}} = -(\vec{\mathbf{p_3}} + \vec{\mathbf{p_5}})$, and we can rewrite 2.35 as

$$E_a \approx M + \frac{(p_3 + p_5)^2}{2M} \cdot \frac{m^2}{m^2} = M \left(1 + \frac{(p_3 + p_5)^2}{2m^2} \frac{m^2}{M^2}\right). \tag{2.36}$$

Since in the following we will consider also the leptons to be non relativistic, and we will then expand in the small parameter p_3/m, it is clear that the correction to the ALP energy due to its momentum is much much smaller than any reasonable order of expansion in p_3/m, given the presence of the term m^2/M^2 [2]. So, every time we encounter E_a, we can substitute directly M and the error we are making is much smaller than the ones we will introduce in the following.
With this in mind, integrating the $\delta^3(\vec{\mathbf{p}}_{in} - \vec{\mathbf{p}}_{out})$, we are left with

$$\begin{aligned}\sigma &= \int \frac{\mathrm{d}^3p_3}{2E_3}\frac{\mathrm{d}^3p_5}{2E_5}\frac{1}{2s}\frac{1}{2M}|\mathcal{M}_t|^2\delta(E_{in}-E_{out}) \\ &= \int \frac{1}{16sM(2\pi)^5}\frac{1}{(2m^2-\sqrt{s}(E_3-\cos\theta_3 p_3\beta))^2}\frac{1}{(2m^2-\sqrt{s}(E_5+\cos\theta_5 p_5\beta))^2}\times \\ &\times \delta(\sqrt{s}-M-E_3-E_5)\frac{\mathrm{d}^3p_3}{E_3}\frac{\mathrm{d}^3p_5}{E_5}\end{aligned} \tag{2.37}$$

Then, using the usual substitution to "spherical coordinates", we rewrite $\mathrm{d}^3p = p^2\mathrm{d}p\mathrm{d}\cos(\theta)\mathrm{d}\phi = pE\mathrm{d}E\mathrm{d}\cos\theta\mathrm{d}\phi$, to get to

$$\begin{aligned}\sigma &= \frac{1}{16sM(2\pi)^4}\int \mathrm{d}\cos\theta_3\mathrm{d}\cos\theta_5\mathrm{d}E_3\mathrm{d}E_5\delta(2m(1+\alpha)-E_3-E_5)\times \\ &\times \frac{p_3}{(2m^2-\sqrt{s}(E_3-\cos\theta_3 p_3\beta))^2}\frac{p_5}{(2m^2-\sqrt{s}(E_5+\cos\theta_5 p_5\beta))^2} = \\ &= \int \mathrm{d}\cos\theta_3\mathrm{d}\cos\theta_5\mathrm{d}E_3\frac{p_3\sqrt{(2(\alpha+1)m-E_3)^2-m^2}}{256\pi^4 s\left(\sqrt{s}-2(\alpha+1)m\right)\left(2m^2-\sqrt{s}(E_3-\beta\cos\theta_3 p_3)\right)^2}\times \\ &\times \frac{1}{\left(2m^2-\sqrt{s}\left(\beta\cos\theta_4\sqrt{(2(\alpha+1)m-E_3)^2-m^2}-E_3+2(\alpha+1)m\right)\right)^2},\end{aligned} \tag{2.38}$$

where we first integrated in ϕ (integrates to 2π since it does not appear in the integrand) and then we integrated the delta of the energy, substituting $E_5 = 2m(1+\alpha) - E_3$. Even with all of the simplifications we introduced, this integral is far from trivial. In fact, it turns out that it is not possible to obtain a fully analytical result in this way, due to the fact that whatever variable we choose to integrate next will give rise to elliptical integrals which are only known numerically. Approaching the calculations in spherical coordinates is rather typical. Therefore we have invested some time and effort to show that elliptical integrals are inevitable. Appendix A gives a rather complete exposition of our attempts in spherical coordinates, for the interested reader.

2.3 Introduction to Gram determinants for analytical cross section

In order to regain control over the analiticity of the result, it is clear that we cannot use standard methods of integration that relies on a change to spherical coordinates.

[2] Numerically, for Belle-II, $\sqrt{s} \sim 10.58$ GeV, so this factor is less than 10^{-8}.

Instead, we will make use of a different technique, introduced in the '60s [48, 49, 50] that is **generalized Mandelstam variables** (GMV). These in turn are strictly related to mathematical objects, called Gram Determinants, which can describe in a very compact way the boundary of the phase space of any process.
Let us start from some useful definitions. Given a vector space, and two sets of elements in this space $\{p_1, \dots, p_n\}$, $\{q_1, \dots, q_n\}$, we can define the Gram matrix as

$$M\begin{pmatrix}\{p_1,\dots,p_n\},\\ \{q_1,\dots,q_n\}\end{pmatrix} = \begin{pmatrix} p_1\cdot q_1 & \dots & p_1\cdot q_n \\ \vdots & \vdots & \vdots \\ p_n\cdot q_1 & \dots & p_n\cdot q_n \end{pmatrix}, \tag{2.39}$$

where the $\cdot$ denotes the scalar product in such vector space. A Gram Determinant (GD) is the determinant of a Gram matrix:

$$G\begin{pmatrix}\{p_1,\dots,p_n\},\\ \{q_1,\dots,q_n\}\end{pmatrix} = \det M\begin{pmatrix}\{p_1,\dots,p_n\},\\ \{q_1,\dots,q_n\}\end{pmatrix}. \tag{2.40}$$

If the two entries are the same, we are dealing with a **symmetric Gram Determinant**

$$\Delta_n(\{p_1,\dots,p_n\}) = G\begin{pmatrix}\{p_1,\dots,p_n\},\\ \{p_1,\dots,p_n\}\end{pmatrix}, \tag{2.41}$$

and we call n the dimension of Δ_n. In our case, the vector space will be the Minkowski space, and the set of vectors will be four-momenta.

2.3.1 Gram Determinants as area of generalized triangles

These mathematical quantities are not completely abstract; they are in fact linked to the area of hypertriangles. For example, Δ_2 is the area of a triangle. In order to see so, we need Hero's formula for the area of a triangle of sides length x, y, z

$$A = \frac{1}{4}\sqrt{-\lambda(x^2, y^2, z^2)}, \tag{2.42}$$

where λ is nothing more than the triangular λ function appearing in phase space calculations

$$\lambda(x, y, z) := x^2 + y^2 + z^2 - 2xy - 2xz - 2yz. \tag{2.43}$$

One can check that choosing appropriately x, y, z, Δ_2 and $\lambda(x, y, z)$ are related:

$$x := m_1^4 + (p_1\cdot p_2)^2,\ y := m_2^4 + (p_1\cdot p_2)^2,\ z := (m_1^2 - p_1\cdot p_2)^2 + (m_2^2 - p_1\cdot p_2)^2$$
$$\Rightarrow 4\Delta_2(p_1, p_2)^2 = -\lambda(x, y, z). \tag{2.44}$$

In the same way, with some more work, we can relate Δ_3 to the area of a tetrahedron. First we need to define another quantity introduced by Tartaglia to compute the area of a general tetrahedron given its edges:

$$\mathcal{G}(x, y, z, u, v, w) := \begin{pmatrix} \begin{vmatrix} 0 & 1 & 1 & 1 & 1 \\ 1 & 0 & u & y & v \\ 1 & u & 0 & w & x \\ 1 & y & w & 0 & z \\ 1 & v & x & z & 0 \end{vmatrix} \end{pmatrix}. \tag{2.45}$$

Once again, if we take the vertices of a tetrahedron to be [3]

$$v_1 = (0, 0, 0); \tag{2.46}$$
$$v_2 = (0, 0, u); \tag{2.47}$$
$$v_3 = y(\sin\theta_y, 0, \cos\theta_y); \tag{2.48}$$
$$v_4 = v(\sin\theta_v \cos\phi, \sin\theta_v \sin\phi, \cos\theta_v), \tag{2.49}$$

with θ_v, θ_y, ϕ solutions of the equations

$$w = \|v_2 - v_3\| \tag{2.50}$$
$$x = \|v_2 - v_4\| \tag{2.51}$$
$$z = \|v_3 - v_4\|, \tag{2.52}$$

Δ_3 can be related to the area of the tetrahedron $\mathcal{G}$:

$$\Delta_3(p_1, p_2, p_3) = -\frac{1}{2}\mathcal{G}((p_1 + p_2)^2, (p_1 - p_3)^2, (p_1 + p_2 - p_3)^2, m_1^2, m_2^2, m_3^2). \tag{2.53}$$

2.3.2 From polar coordinates to Gram Determinants

Take some four-momenta p_i in polar coordinates, with mass m_i, energy E_i, polar angle θ_i and azimuthal angle ϕ_i. Define their sum as p_0, with mass m_0, and suppose to be in the rest frame of p_0. Then, one gets

$$m_i = \sqrt{\Delta_1(p_i)} \tag{2.54}$$
$$|\vec{\mathbf{p_i}}| = \frac{\sqrt{-\Delta_2(p_0,p_i)}}{m_0} \tag{2.55}$$
$$|\sin\theta_{ij}| = m_0\sqrt{\frac{\Delta_3(p_0,p_i,p_j)}{\Delta_2(p_0,p_i)\Delta_2(p_0,p_j)}} \tag{2.56}$$
$$\left|\sin\phi_{(ij),(ik)}\right| = \left[\frac{\Delta_4(p_0,p_i,p_j,p_k)\Delta_2(p_0,p_i)}{\Delta_3(p_0,p_i,p_j)\Delta_3(p_0,p_i,p_k)}\right]^{\frac{1}{2}}, \tag{2.57}$$

where θ_{ij} is the angle between p_i and p_j, while $\phi_{(ij),(ik)}$ is the angle between the (p_i, p_j) and (p_i, p_k) planes. From these equations, one also gets the following conditions for the Gram determinants:

$$\Delta_1(p_i) \geq 0 \tag{2.58}$$
$$\Delta_2(p_i, p_j) \leq 0 \tag{2.59}$$
$$\Delta_3(p_i, p_j, p_k) \geq 0 \tag{2.60}$$
$$\Delta_4(p_0, p_i, p_j, p_k) \leq 0. \tag{2.61}$$

How can we define the boundary of integrations after this change of variables? Without going into further details, which can be found in [48, 49], Gram determinants are especially useful in this situation too. It can be shown, in fact, that the full phase space boundary is defined by all the nodes of the largest Gram Determinant one can define in a given scattering. This set of points is called the **Kibble curve**.

[3] An attentive reader may note that these vertices could be the three momenta of particles coming from a decay or a scattering; that is exactly what we are going to use in the following discussion.

2.3.3 Generalized Mandelstam variables

Mandelstam variables are introduced in any QFT book ([51] for example) since they are extraordinarily effective in describing $2 \to 2$ scatterings. In fact, for a scattering like $p_1 + p_2 \to p_3 \to p_4$, the usual definition of Mandelstam variables is

$$s = (p_1 + p_2)^2, \quad t = (p_1 - p_3)^2, \quad u = (p_1 - p_4)^2; \tag{2.62}$$

from four-momentum conservation, one gets also the property

$$s + t + u = m_1^2 + m_2^2 + m_3^2 + m_4^2 =: K. \tag{2.63}$$

In a $2 \to 2$ scattering, the largest Gram Determinant we can build is Δ_3, which, as we have seen in eq. (2.53), can be also expressed as $\mathcal{G}(s, t, m_4^2, m_1^2, m_2^2, m_3^2)$. The scattering phase space will be defined by $\mathcal{G} \geq 0$, while the Kibble curve (its boundary) by the equation

$$-2\mathcal{G} = stu - (\alpha s + \beta t + \gamma u) = 0, \tag{2.64}$$

with

$$K\alpha = (m_1^2 m_2^2 - m_3^2 m_4^2)(m_1^2 + m_2^2 - m_3^2 - m_4^2), \tag{2.65}$$
$$K\beta = (m_1^2 m_3^2 - m_2^2 m_4^2)(m_1^2 + m_3^2 - m_2^2 - m_4^2), \tag{2.66}$$
$$K\gamma = (m_1^2 m_4^2 - m_2^2 m_3^2)(m_1^2 + m_4^2 - m_2^2 - m_3^2). \tag{2.67}$$

A depiction of the Kibble curve and of the allowed phase space is in fig. 2.4. The area identified by $\mathcal{G} = 0$ is a disconnected union of four regions. Three of these correspond to each channel of the $2 \to 2$ scattering; for example, the s region is located in the portion of the s, t plane with $s \geq (m_1 + m_2)^2$, $t \leq (m_1 - m_3)^2$. The central pink region instead represents the phase space of the $1 \to 3$ decay, and it is nothing else than the allowed phase space of a Dalitz plot.

If we go back to our $2 \to 3$ scattering, we can still utilize Mandesltam variables, but this time we need 5 of them since there are 5 degrees of freedom. Given the scattering $p_1 + p_2 \to p_3 + p_4 + p_5$, with $p_i^2 = m_i^2$, we have

$$s = (p_1 + p_2)^2, \quad s_1 = (p_3 + p_4)^2, \quad s_2 = (p_4 + p_5)^2 \tag{2.68}$$
$$t_1 = (p_1 - p_3)^2, \quad t_2 = (p_2 - p_5)^2. \tag{2.69}$$

This is not the only choice possible, and in fact it is useful to define other variables (that are of course combinations of s, s_1, s_2, t_1, t_2) like

$$u_1 = (p_3 + p_5)^2, \quad u_2 = (p_1 - p_5)^2, \quad u_3 = (p_2 - p_3)^2, \tag{2.70}$$
$$u_4 = (p_2 - p_4)^2, \quad u_5 = (p_1 - p_4)^2. \tag{2.71}$$

With these variables, the matrix elements in 2.33 become

$$\mathcal{M}_s = \frac{1}{su_1}, \quad \mathcal{M}_t = \frac{1}{t_1 t_2}. \tag{2.72}$$

The phase space allowed in this case is determined by the equation $\Delta_4 \leq 0$.

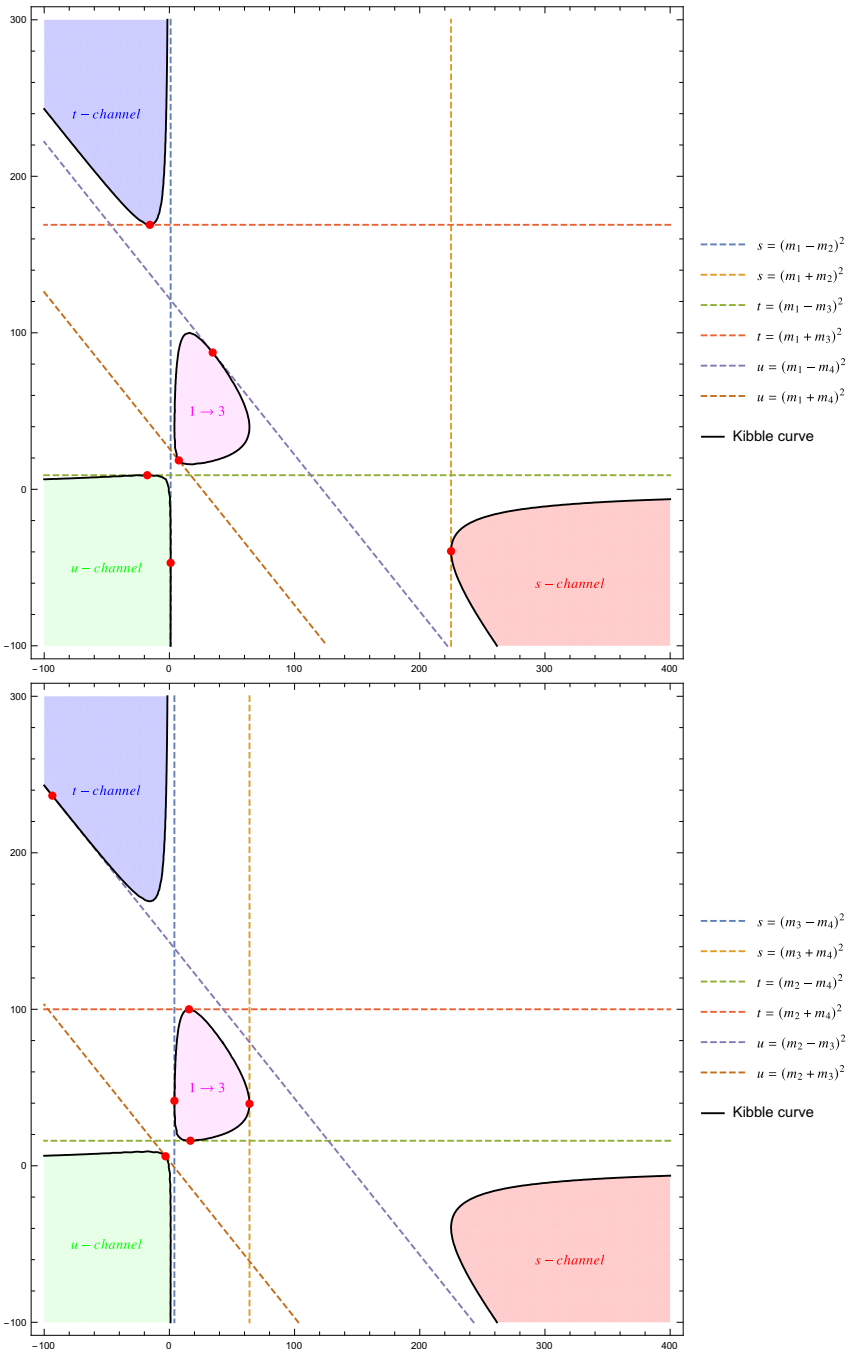

Figure 2.4. Allowed phase space and Kibble curve in the s, t plane for masses $m_1 = 8, m_2 = 7, m_3 = 5, m_4 = 3$ in arbitrary units. We divided the asymptotes in two figures for ease of visualization. The red dots are tangency points; the central pink region is the allowed phase space for a $1 \to 3$ scattering; the other infinite regions are the allowed phase space for the s, t, u channel respectively.

Let us now go back to eq. 2.34, and see why we introduced all these notions. We can easily integrate away p_4 using the Dirac δ (since it does not appear in the matrix element):

$$\int \frac{\mathrm{d}^3 p_4}{2E_4}\delta^{(4)}(p_1+p_2-p_3-p_4-p_5) = \tag{2.73}$$

$$\int \mathrm{d}^4 p_4 \delta(p_4^2-m_4^2)\theta(p_4^0)\delta^{(4)}(p_1+p_2-p_3-p_4-p_5). \tag{2.74}$$

This leaves us with a one dimensional $\delta(f)$, where the argument is explicitly

$$f = (p_1+p_2-p_3-p_5)^2 - m_4^2 = \tag{2.75}$$

$$= s - 2\sqrt{s}(E_3+E_5) + m_3^2 + m_5^2 + 2(E_3E_5 - |\vec{\mathbf{p_3}}||\vec{\mathbf{p_5}}|\cos\theta_{35}), \tag{2.76}$$

and $\cos\theta_{35} = \cos\theta_3\cos\theta_5 + \sin\theta_3\sin\theta_5\cos\phi$.
This function is linear in $\cos\phi$; we can get rid of the integration in $\mathrm{d}\phi$ then by using the properties of the δ function, obtaining

$$\int \mathrm{d}\phi\delta(a\cos\phi - b) = \frac{1}{|a|\sqrt{(1-\left(\frac{b}{a}\right)^2}}. \tag{2.77}$$

Notice that the δ is verified if $\cos\phi = b/a$; then, the expression under the square root is none other than $\sin^2\phi$, for which we can use the definition of eq. 2.57 and obtain

$$a^2\left[1-\left(\frac{b}{a}\right)^2\right] = \frac{-4\Delta_4}{\lambda(s,m_1^2,m_2^2)}. \tag{2.78}$$

Now let's change all the other variables to the generalized Mandelstam set:

$$\mathrm{d}E_3\mathrm{d}\theta_3\mathrm{d}E_5\mathrm{d}\theta_5 = \mathrm{d}s_1\mathrm{d}s_2\mathrm{d}t_1\mathrm{d}t_2|J| \tag{2.79}$$

$$|J| = \frac{1}{16\lambda(s,m_1^2,m_2^2)}. \tag{2.80}$$

Finally, the cross section can be rewritten in terms of Mandelstam variables (ignoring the couplings) as

$$\sigma = \int \mathrm{d}s_1\mathrm{d}s_2\mathrm{d}t_1\mathrm{d}t_2 \frac{1}{32(2\pi)^4 f\sqrt{\lambda(s,m_1^2,m_2^2)}}\frac{\theta(-\Delta_4)}{\sqrt{-\Delta_4}}|\mathcal{M}|^2, \tag{2.81}$$

where

$$|\mathcal{M}|^2 = |\mathcal{M}_s|^2 + |\mathcal{M}_t|^2 + \mathcal{M}_s\mathcal{M}_t^* + \mathcal{M}_s^*\mathcal{M}_t. \tag{2.82}$$

We can now proceed to integrating. We will stick to the sSM case, so that the matrix element is very simplified; a more general discussion goes beyond the scope of this thesis. The s channel integration is not particularly difficult, and in fact can be done even in spherical coordinates; for this reason, all the following discussion relates to the integration of the t-channel only.

t-channel integration

The first integration we want to make is that of s_2; we know the t-channel does not depend on it, so we only need to compute

$$I_{s_2} = \int \mathrm{d}s_2 \frac{\theta(\Delta_4)}{\sqrt{-\Delta_4}}. \tag{2.83}$$

Δ_4 is a polynomial in s_2, more specifically a parabola; it is useful to rewrite it in terms of its roots $s_2^{\pm}$:

$$\Delta_4 = as_2^2 + bs_2 + c = a(s_2 - s_2^-)(s_2 - s_2^+). \tag{2.84}$$

Following the procedure of [48], we can write the discriminant of this equation as

$$b^2 - 4ac = 64\Delta_3(p_1, p_2 - p_5, p_5)\Delta_3(p_1, p_2 - p_5, p_3) \tag{2.85}$$

$$= 4\mathcal{G}_1(s, t_2, s_1, m_2^2, m_1^2, m_5^2)\mathcal{G}_2(t_1, s_1, t_2, m_3^2, m_1^2, m_4^2), \tag{2.86}$$

and this means that the following integration boundaries will be dictated by $\mathcal{G}_{1,2} \leq 0$ in order for the solution to exist.
We refer to the tabulated integrals in [52] to compute the integral in 2.83 (or one can check with Mathematica); the result is surprisingly simple, and is

$$I_{s_2} = \frac{\pi}{\sqrt{a}}. \tag{2.87}$$

Then we only need to recover the coefficient of the second degree term of s_2 in Δ_4; one can easily check that

$$a = \frac{\lambda(s_1, t_2, m_1^2)}{16}. \tag{2.88}$$

Limiting ourselves to the t-channel cross section, in which $\mathcal{M}_t = \frac{1}{t_1 t_2}$ eq. 2.81 reads

$$\sigma_t = C \int \frac{\mathrm{d}t_1 \mathrm{d}t_2}{t_1^2 t_2^2} \mathrm{d}s_1 \frac{\theta(-\mathcal{G}_1)\theta(-\mathcal{G}_2)}{\sqrt{\lambda(s_1, t_2, m_1^2)}}, \tag{2.89}$$

where the Heavyside θ are needed to ensure the existence of a solution, and we collected all constant factors inside C. Let us write explicitly the expressions for $\mathcal{G}_{1,2}$ since they will be useful later:

$$\mathcal{G}_1 = \tfrac{m_e^2 s_1^2}{2} - s_1\left(\tfrac{st_2}{2} + m_e^4\right) + \tfrac{1}{2}\left[m_e^6 - 3m_e^2 st_2 + st_2(s + t_2)\right], \tag{2.90}$$

$$\mathcal{G}_2 = \tfrac{t_1 s_1^2}{2} - \tfrac{1}{2}s_1\left(M_a^2 + 2m_e^2 + t_2 - t_1\right)^2 + \\ + \tfrac{1}{2}\left[M_a^4 m_e^2 + m_e^4 t_1 + m_e^2 t_2(t_2 - t_1) + M_a^2(t_1 t_2 - m_e^2(t_1 + 2t_2))\right], \tag{2.91}$$

and we remark that in general $\mathcal{G}_{1,2}$ are **quadratic** functions of t_1 (and of any other s and t).

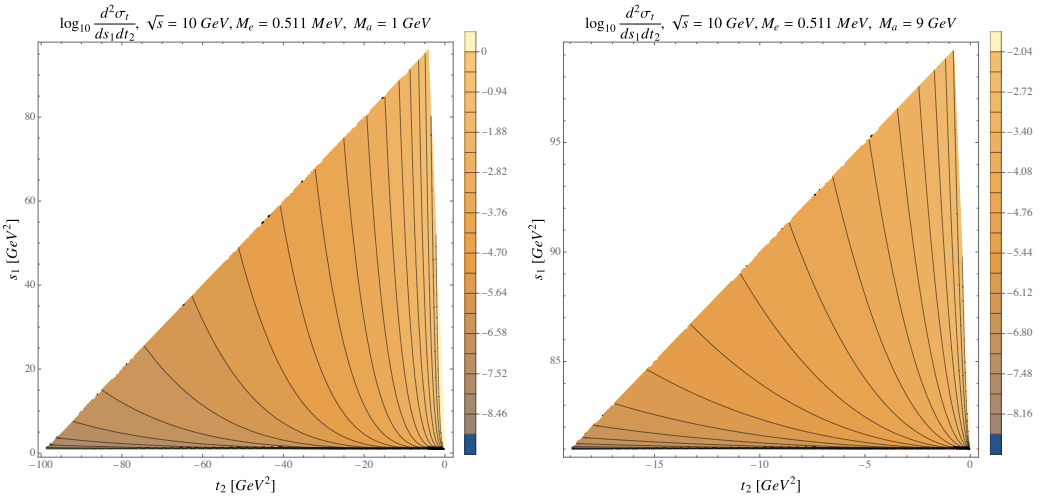

(a) $M_a = 1$ GeV **(b)** $M_a = 9$ GeV

Figure 2.5. $\frac{\mathrm{d}^2\sigma_t}{\mathrm{d}t_2\mathrm{d}s_1}$ for two benchmark values of M_a. We can see how the maximal contributions come from the regions of minimal s_1 and maximal t_2.

Differential cross sections

Let us first compute $\frac{\mathrm{d}^2\sigma_t}{\mathrm{d}t_2\mathrm{d}s_1}$, by integrating in t_1, in order to get an idea of where the cross section will be pointing to. Since only $\mathcal{G}_2$ depends on t_1, the domain of integration is

$$\mathcal{G}_2 = \frac{s_1^2}{2}(t - t_1^-)(t - t_1^+) \leq 0, \quad t_1^- \leq t_1 \leq t_1^+ \leq 0. \tag{2.92}$$

Once again, $t_1^\pm$ are the roots of eq. 2.91 while solving for t_1. Explicitly, they read

$$\begin{aligned} 2s_1 t_1^\pm = {} & s_1 t_2 - s_1^2 + M_a^2\,(s_1 - t_2) + M_e^2\left(M_a^2 + 2s_1 + t_2\right) - M_e^4 + \\ & \pm\sqrt{\lambda\,(s_1, M_e^2, M_a^2)\,\lambda\,(s_1, t_2, M_e^2)}. \end{aligned} \tag{2.93}$$

Notice that the possible divergence $t_1 = 0$ is always excluded. In fact, it would need $t_2 = M_a^2 > 0$, which is not possible, since $t_2 \leq 0$. The same argument can be repeated for t_2, for symmetry reasons. Our cross section then becomes

$$\begin{aligned} \sigma_t &= C \int \frac{\mathrm{d}t_2 \mathrm{d}s_1}{t_2^2} \frac{\theta(-\mathcal{G}_1)}{\sqrt{\lambda(s_1, t_2, m_e^2)}} \int \frac{\mathrm{d}t_1}{t_1^2}\theta(-\mathcal{G}_2) \\ &= \frac{C}{m_e^2} \int \mathrm{d}t_2 \mathrm{d}s_1 \theta(-\mathcal{G}_1) \frac{\lambda(s_1, M_a^2, m_e^2)}{t_2^2 (t_2 - M_a^2)^2}, \end{aligned} \tag{2.94}$$

where in the last equality we have integrated t_1 between its boundaries (defined by $\theta(\mathcal{G}_2)$) $t_1^- \leq t_1 \leq t_1^+$. We can plot this doubly differential cross section to have an idea of which regions of the phase space contribute the most. The most important regions for the cross section, independently from the mass, are the ones with small s_1 and maximal t_2.

The expressions obtained thanks to the Gram Determinants, while not completely

formal, allows us to carry out more analytical integrations. Indeed, we can integrate s_1 and obtain $\mathrm{d}\sigma/\mathrm{d}t_1$. From eq 2.90, the domain of s_1 is

$$s_1^+ \leq (m_e^2 + M_a^2) \leq s_1 \leq s_1^- \leq (\sqrt{s} - m_e)^2, \tag{2.95}$$

and the integration yields

$$\begin{aligned}\frac{\mathrm{d}\sigma_t}{\mathrm{d}t_2} = \frac{C}{M_e^2}\frac{1}{t_2^2\left(t_2 - M_a^2\right)^2}\Bigg[&\frac{1}{2}\sqrt{\lambda\left(s_1^-, M_a^2, m_e^2\right)}\left(s_1^- - \left(M_a^2 + m_e^2\right)\right) \\ &-2\left(M_a m_e\right)^2 \log\left(\frac{\sqrt{\lambda\left(s_1^-, M_a^2, m_e^2\right)} + s_1^- - \left(M_a^2 + m_e^2\right)}{2M_a m_e}\right)\Bigg].\end{aligned} \tag{2.96}$$

We are able to compute analytically the differential cross section, which can be extremely useful to compare to experimental data. Moreover, it does not usually happens that one is able to get a closed form for a $2 \to 3$ scattering cross section while considering **explicit masses**.

Let us shift our attention to $\frac{\mathrm{d}^2\sigma_t}{\mathrm{d}t_1\mathrm{d}t_2}$, which is the most interesting distribution for the t-channel.
Starting from eq. 2.89, we need to first integrate s_1:

$$\int \mathrm{d}s_1 \theta(-\mathcal{G}_1)\theta(-\mathcal{G}_2) = \int_{f(t_1,t_2)}^{g(t_1,t_2)} \mathrm{d}s_1. \tag{2.97}$$

Both $\mathcal{G}_{1,2}$ in fact depend on s_1; the first task is to find what the integration boundary is. To do so, we need to simultaneously satisfy $\mathcal{G}_i = 0,\ i = 1, 2$. We will extend the procedure carried out for massless particles in [48] to the case of massive particles, with $m_1 = m_2 = m_3 = m_5 = m_e$ and $m_4 = M_a$.
Define $s_{1,i}^{\pm}$ the roots of $\mathcal{G}_i$ when solved for s_1. We have

$$\begin{aligned}s_{1,1}^{\pm} &= \frac{2m_e^4 + st_2 \pm \sqrt{\lambda\left(s, m_e^2, m_e^2\right)\lambda\left(t_2, m_e^2, m_e^2\right)}}{2m_e^2} \\ s_{1,2}^{\pm} &= \frac{M_a^2 t_1 + 2m_e^2 t_1 - t_1 t_2 \pm \sqrt{\lambda\left(s, m_e^2, m_e^2\right)\lambda\left(t_1, t_2, M_a^2\right)}}{2t_1}.\end{aligned} \tag{2.98}$$

Which of thee solutions are acceptable? As in [48], on the boundary at least one of the following conditions is true:

$$s_{1,1}^+ = s_{1,2}^-, \tag{2.99}$$
$$s_{1,2}^+ = s_{1,1}^-, \tag{2.100}$$
$$t_1 = \max t_1 = (m_1 - m_3)^2, \tag{2.101}$$
$$t_2 = \max t_2 = (m_2 - m_5)^2, \tag{2.102}$$
$$\lambda(t_1, t_2, m_4^2) = 0. \tag{2.103}$$

Eq. 2.103 needs at least one of t_1, t_2 to be positive, which is not possible. Eqs (2.101) and (2.102) also lead to unphysical results: when substituting $t_1 = t_2 = 0$ in the

boundary conditions $\mathcal{G}_i = 0$, one gets

$$\mathcal{G}_1(t_2 = 0) = \frac{m_e^2}{2}(s_1 - m_e^2)^2 \tag{2.104}$$

$$\mathcal{G}_2(t_1 = 0) = \frac{m_e^2}{2}(t_2 - M_a^2)^2. \tag{2.105}$$

In both cases we are outside the boundary defined by the Heavyside θ. This only leaves (2.99) and (2.100). Looking explicitly at $\mathcal{G}_{1,2}$ as a polynomial in s_1, it can be shown that both functions only have one positive root in s_1. Explicitly,

$$\begin{aligned}
\mathcal{G}_1 &= \frac{m_e^2 s_1^2}{2} - s_1\left(\frac{st_2}{2} + m_e^4\right) + \frac{1}{2}\left(m_e^6 - 3m_e^2 st_2 + st_2\,(s + t_2)\right) \\
\mathcal{G}_2 &= \frac{t_1 s_1^2}{2} - \frac{1}{2}s_1\left(M_a^2 + 2m_e^2 + t_2 - t_1\right) \\
&\quad + \frac{1}{2}\left(M_a^4 m_e^2 + m_e^4 t_1 + m_e^2 t_2\,(t_2 - t_1) + M_a^2\left(t_1 t_2 - m_e^2\,(t_1 + 2t_2)\right)\right);
\end{aligned} \tag{2.106}$$

to find which solution is acceptable, we can expand in the small parameter $\epsilon = \frac{m_e}{\sqrt{s}}$, finding the two solutions

$$s_{1,1}^- = s + t_2 + \mathcal{O}(\epsilon^2), \tag{2.107}$$

$$s_{1,1}^+ = -s - t_2 + \mathcal{O}(\epsilon^2). \tag{2.108}$$

So the only true condition on the boundary is eq. 2.100. Let us write also the approximate value of $s_{1,2}^+$:

$$s_{1,2}^+ = \frac{M_a^2}{2} + m_e^2 + \frac{\sqrt{4m_e^2 - t_1}\sqrt{M_a^4 - 4M_a^2 t_1}}{2\sqrt{-t_1}} + \mathcal{O}(\epsilon). \tag{2.109}$$

For each value of t_2, t_1 will be bounded by some values depending on t_2; $t_1^{\min}(t_2)$ and $t_1^{\max}(t_2)$ come from the two solutions to the equation $s_{1,1}^- = s_{1,2}^+$; in fig. 2.6 we see that $s_{1,1}^- \geq s_{1,2}^+$ for all t_2. Integrating in s_1, assuming that the matrix element does not depend on it, yields

$$\boxed{\frac{\mathrm{d}^2\sigma}{\mathrm{d}t_1\mathrm{d}t_2} \propto \frac{|\mathcal{M}|^2}{4\sqrt{\lambda(s, m_1^2, m_2^2)}} \log\left(\frac{s_{1,1}^- - t_2 - m_1^2 + \sqrt{\lambda(s_{1,1}^-, t_2, m_1^2)}}{s_{1,2}^+ - t_2 - m_1^2 + \sqrt{\lambda(s_{1,2}^+, t_2, m_1^2)}}\right).} \tag{2.110}$$

Even if it does not seem like it, this function is symmetrical under the exchange $t_1 \leftrightarrow t_2$. A depiction of what regions are the most important for the cross section is given in fig. 2.7. It is clear that the most important contribute to the cross section comes from the region of the phase space closest to the divergence; it is also clear that a kinematical cut on final particles (in energy or in angle) can drastically cut the cross section by making impossible for the top-right region of 2.7 to be populated. This same cut would have little to no effect in the s-channel; this is one of the reasons why VBF processes at Belle II have not been considered in the literature (more details in the following chapters).
An interesting point to make is to find out which configuration of four-momenta

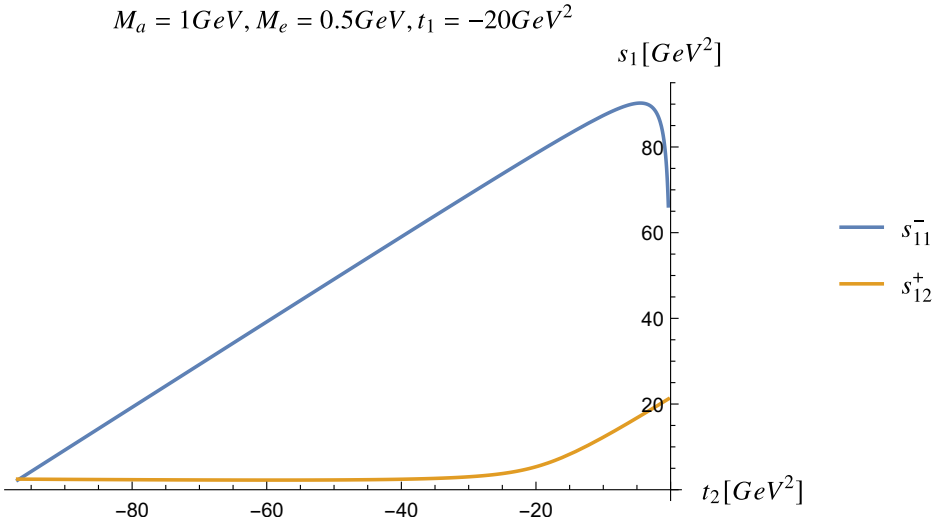

Figure 2.6. A plot showing $s_{1,1}^- \geq s_{1,2}^+$. The two intersection points define the boundary of integration. This specific configuration assumes $s = 100$ GeV^2, $M_a = 1$ GeV, $m_e = 0.5$ GeV, $t_1 = -20$ GeV^2.

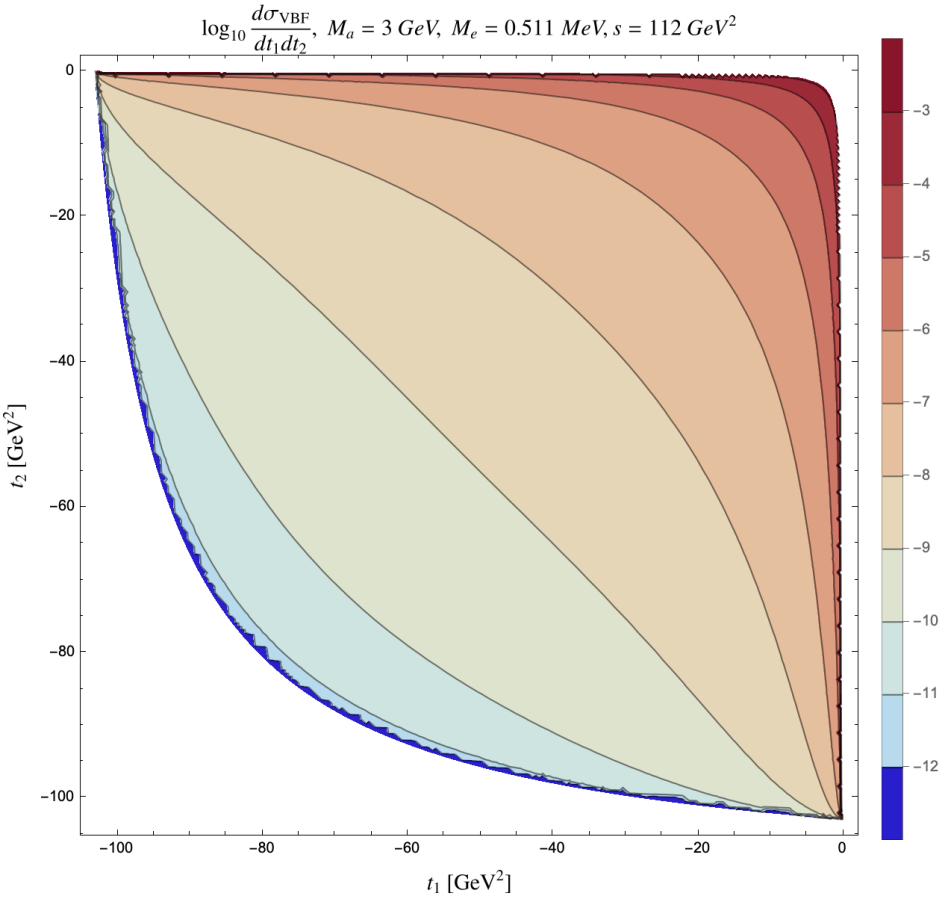

Figure 2.7. $\log_{10} \frac{\mathrm{d}^2\sigma_t}{\mathrm{d}t_1 \mathrm{d}t_2}$. The parameters used are $s = 112$ GeV^2, $M_a = 3$ GeV, $m_e = 0.511$ MeV. The clearly preferred direction is the one that minimizes both $|t_1|$ and $|t_2|$.

corresponds to the "maximal" contribution to the cross section, the top-right corner of 2.7. Take the usual four-momenta p_i, each with velocity β_i and Lorentz factor γ_i. In the centre of mass frame,

$$\vec{\beta}_1 = -\vec{\beta}_2 = \vec{\beta}; \quad \gamma_1 = \gamma_2 = \gamma. \tag{2.111}$$

We can rewrite explicitly $t_{1,2}$ in terms of these quantities:

$$t_1 = (p_1 - p_3)^2 = 2m_e^2\Big[1 - \gamma\gamma_3(1 - \vec{\beta}\cdot\vec{\beta}_3)\Big] \tag{2.112}$$

$$t_2 = (p_2 - p_5)^2 = 2m_e^2\Big[1 - \gamma\gamma_5(1 + \vec{\beta}\cdot\vec{\beta}_5)\Big]. \tag{2.113}$$

The only way for $t_1 = t_2$ is $\vec{\beta}_3 = -\vec{\beta}_5 = \vec{\beta}_F$, which implies $\gamma_3 = \gamma_5 = \gamma_F$. Four-momentum conservation will then imply

$$\vec{\beta}_4 = 0, \quad \gamma_F = \frac{\sqrt{s} - M_a}{2m_e} : \tag{2.114}$$

the most favorable region is the one in which the ALP is produced at rest, while the leptons are back to back, with polar angle θ as close to the beam axis as possible.

2.4 Asymmetry and collinearity

Now that we were able to finally compute the analytical cross section for the (scalar) VBF process, it is time to see when the approximation of collinearity fails. Until now, the results we showed were already mostly known in the literature; the following discussion is a completely new contribution to answer our original question: when does the approximation of collinearity between the incoming electron and the virtual photon stops working?
In the series of pictures of fig. 2.8 we show the behaviour of $\frac{\mathrm{d}^2\sigma_t}{\mathrm{d}E_5\mathrm{d}\cos\theta_5}$; this is none other than $\frac{\mathrm{d}^2\sigma_t}{\mathrm{d}s_1\mathrm{d}t_2}$ of section 2.3.3 recast back into polar coordinates. This is not just an academic exercise: it helps us show that there exist some region of the phase space in which the collinearity does not exist at all. What we see is that even for very high ALP masses, very close to $\sqrt{s}$, as long as the final leptons can still be ultra-relativistic, they will tend to be collinear to the beam axis. At some point however, the ALP becomes so massive that the final leptons become non relativistic, and the ALP being basically still means that the $2 \to 3$ process becomes a quasi-$2 \to 2$ process, which of course is isotropic in the polar angle of the leptons.
Another interesting quantity we can define is the **asymmetry**: given a function $f(\cos\theta, \vec{x})$, monotonic in $\cos\theta$ and with $\vec{x}$ any other variable,

$$\mathcal{A} = \frac{f(c_+, \vec{x}) - f(c_-, \vec{x})}{f(c_+, \vec{x}) + f(c_-, \vec{x})}, \tag{2.115}$$

where $c_\pm$ are respectively the maximum and minimum value of $\cos\theta$ allowed. If $\mathcal{A}$ is close to ± 1, f is anisotropic, with the privileged direction identified by $c_\pm$. Instead $\mathcal{A} \to 0$ means that f is isotropic.
Since we have seen how collinearity is lost for $M_a \simeq \sqrt{s}$, we can estimate, using the

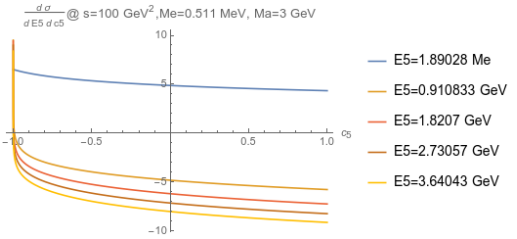

(a) $M_a = 3$ GeV $\ll \sqrt{s}$. Strong preference for $\cos\theta_5 \to -1$.

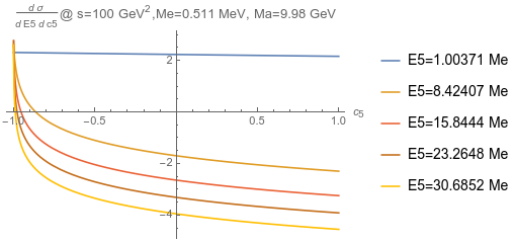

(b) $M_a = 9.98$ GeV. Even if $M_a \lesssim \sqrt{s}$, the electrons are ultra-relativistic. Still clear preference for $\cos\theta_5 \to -1$.

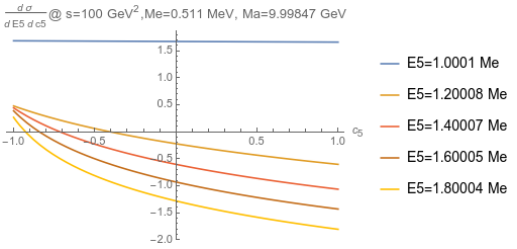

(c) $M_a = \sqrt{s} - 3m_e$. Non relativistic final leptons, no longer a clear preference for $\cos\theta_5 \to -1$

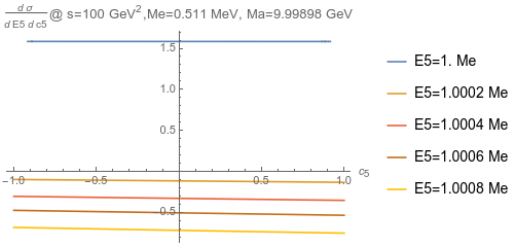

(d) $M_a = \sqrt{s} - (2 + 10^{-3})m_e$. Non relativistic final leptons,the phase space is almost completely closed. No privileged direction.

Figure 2.8. $\log_{10} \frac{\mathrm{d}^2\sigma_t}{\mathrm{d}E_5 \mathrm{d}\cos\theta_5}$ computed in $s = 100$ GeV^2 and different values of M_a. Each figure has multiple curves at fixed E_5 to map the full behaviour of the lepton.

asymmetry, what is the critical mass beyond which no collinearity appears. Let us introduce a small parameter, α, that may be used for a series expansion. We can parametrize the ALP mass as

$$M_a = \sqrt{s} - 2(1+\alpha)m_e, \tag{2.116}$$

with M_a large enough that the final positron p_5 is always non relativistic ($\beta_5 < 0.3$ in all the phase space), we can see that we must consider $\alpha < 0.024$. Taking the fully analytical doubly differential cross section $\frac{\mathrm{d}\sigma_t}{\mathrm{d}E_5 \mathrm{d}\cos\theta_5}$ (section 2.3.3)as f in eq. 2.115, and expanding in terms of the small parameters $\epsilon = m_e/\sqrt{s}$ and β_5 one gets

$$\mathcal{A} = -2\beta_5(1 + 3\epsilon + \mathcal{O}\left(\epsilon^2\right)) + \mathcal{O}\left(\beta_5^3\right), \tag{2.117}$$

which shows the linear dependence of the asymmetry on β_5. If we instead compute the same asymmetry, but with $E_5 = \max E_5$, and then expand in α, we get

$$a \simeq -\frac{4}{1 - 3\epsilon + 2\epsilon^2}\sqrt{\alpha(1 - \epsilon - 4\epsilon^2 + 4\epsilon^3)} + \mathcal{O}(\alpha). \tag{2.118}$$

Inverting this equation we find a function $\alpha(a)$; selecting $|a| = 1/3$ as the threshold after which the usual EPA [46] is a completely wrong estimate of the cross section, we find the interval of α, and hence of ALP mass for which we cannot approximate the full cross section with the EPA.

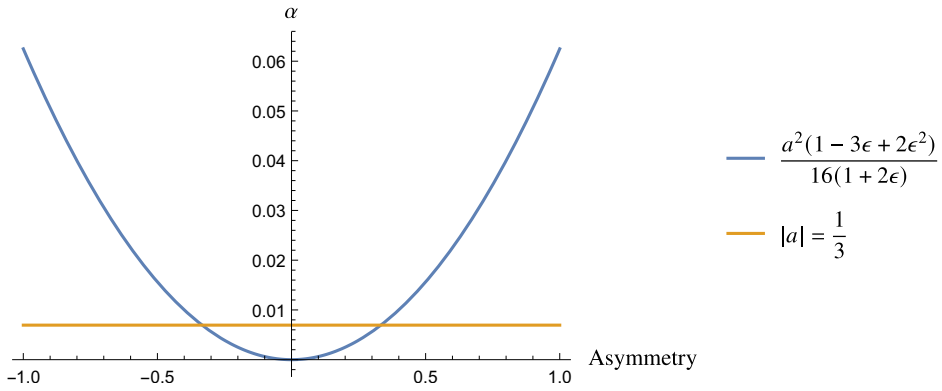

Figure 2.9. All values of α under the yellow line have an asymmetry factor $|a| \leq 1/3$. This is our threshold for claiming that the EPA is not a viable approximation. The blue line is the function $\alpha(a)$ defined in 2.118

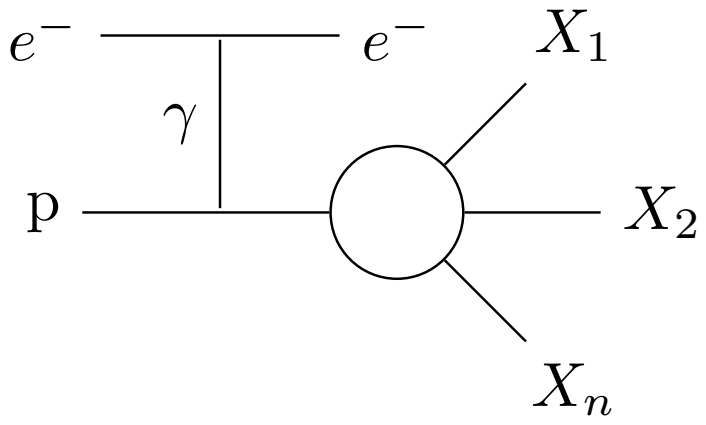

Figure 2.10. $ep \to eX$ in the sSM

2.5 Generalizing EPA to different spins

Before comparing the results of the EPA with the analytical cross section, we need to take a step back to eq. 2.30. This equation was obtained in the full theory, containing fermions and vectors. Our theory is only composed of scalars, and we need to find "our" PDFs; for this reason, we will repeat the same procedure of the authors of [47] for the mock scattering $ep \to eX$ in the sSM.
Define $p\,(p')$ the momentum of the incoming (outgoing) electron, k the momentum of the parton interacting in the process and $q = p - p'$ (see fig. 2.10). Up to implicit coupling, the scattering amplitude is

$$\mathcal{M} \sim \frac{1}{q^2}. \tag{2.119}$$

The cross section will then be

$$\mathrm{d}\sigma = \frac{\mathrm{d}^3 p'}{(2\pi)^3 2E'} \frac{1}{4k\cdot p}\frac{1}{q^4} W \times (\text{couplings})^4, \tag{2.120}$$

where W contains the interaction between the virtual photon and the composed body. In general, $W = W(q^2, k\cdot q)$. Let us now change variables, from (p', θ) to (q^2, y) with

$$y = \frac{k\cdot p}{k\cdot q}. \tag{2.121}$$

The differential becomes

$$\frac{\mathrm{d}^3 p'}{E'} = \pi \mathrm{d}q^2 \mathrm{d}y, \tag{2.122}$$

so that the cross section is

$$\mathrm{d}\sigma = \mathrm{d}q^2 \mathrm{d}y \frac{1}{16\pi^2}\frac{y}{4q^4}\frac{W(q^2, k\cdot q)}{k\cdot q}, \tag{2.123}$$

where we set all couplings to 1 for brevity. Integrating over q^2 yields

$$\mathrm{d}\sigma = \mathrm{d}y \frac{y}{64\pi^2}\left(-\frac{1}{q^2_{\max}} + \frac{1}{q^2_{\min}}\right)\frac{W(q^2, k\cdot q)}{k\cdot q}. \tag{2.124}$$

One should note that the cross section for a real photon scattering on the nucleus can be written as

$$\mathrm{d}\sigma(\gamma p \to X) = \frac{W(q^2, k\cdot q)}{4k\cdot q}; \tag{2.125}$$

comparing to eq. 2.124, we can extract the scalar PDF

$$\mathrm{d}\sigma(ep \to eX) = \mathrm{d}\sigma(\gamma p \to X) \times f_s(y)\mathrm{d}y, \quad \boxed{f_s(y) = \frac{y}{16\pi^2}\left(\frac{1}{q^2_{\min}} - \frac{1}{q^2_{\max}}\right).} \tag{2.126}$$

We remark that the values of $q^2_{\min}$, $q^2_{\max}$ do not depend on the Lorentz nature of the particle, since they come from purely kinematical considerations. Even for the scalar PDF, the region of validity in q^2 is the same of eqs. (2.28) and (2.29).

2.6 Comparison EPA-analytical cross section

We can implement eq. 2.126 to compute the *equivalent scalar approximation* (ESA) for the process $e^+e^- \to e^+e^-a$ in the sSM. Namely, we will compute

$$\sigma(e^+e^- \to e^+e^-a) \to \int \sigma(\gamma\gamma a) f_s(y_1) f_s(y_2) \mathrm{d}y_1 \mathrm{d}y_2. \tag{2.127}$$

Let us define $q_{1,2}$ the four momenta of the two virtual photons, and k the ALP four-momentum. In our scalar theory, the scattering amplitude is just the coupling constant, $\lambda_{a\gamma\gamma}$. Interpreting y_i as the fraction of momentum carried by the virtual photon γ_i, with $y_i \in [0, 1]$ the cross section becomes

$$\sigma = \int \frac{\mathrm{d}^3 k}{2E_k(2\pi)^3}\frac{\lambda^2_{a\gamma\gamma}}{2y_1 y_2 s}(2\pi)^4\delta^4(q_1 + q_2 - k) = \frac{2\pi}{2y_1 y_2 s}\delta(2q_1\cdot q_2 - M_a^2), \tag{2.128}$$

where we used the property

$$\frac{\mathrm{d}^3k}{2E_k} = \mathrm{d}^4k\delta(k^2 - M_2). \tag{2.129}$$

Plugging in eq. 2.128 the explicit form of the four-momenta

$$q_{1,2} = y_{1,2}\frac{\sqrt{s}}{2}\begin{pmatrix}1\\0\\0\\\pm1\end{pmatrix}, \qquad 2q_1 \cdot q_2 = y_1 y_2 s, \tag{2.130}$$

we get

$$\sigma_{ESA}(e^+e^- \to e^+e^-a) = \int \mathrm{d}y_1\mathrm{d}y_2 f_s(y_1)f_s(y_2)\frac{\pi}{y_1y_2s}\delta(y_1y_2s - M_2). \tag{2.131}$$

After the first integration in y_2, the presence of the Dirac δ constrains the domain y_1 in the interval $y_1 \in [\frac{M_a^2}{s}, 1]$, and, recovering the coupling constants in 2.126, we can write

$$\sigma_{ESA} = \frac{\lambda_{ee\gamma^4}\lambda_{a\gamma\gamma}^2}{16\pi s}\int\limits_{\frac{M_a^2}{s}}^{1}\mathrm{d}y_1\Omega(y_1) \tag{2.132}$$

$$\Omega\left(y_1\right) := \frac{s(1-y_1)^3\left(sy_1-M_a^2\right)^3\theta_c^4}{(4m_eM_a)^4\pi^3y_1^2\left((2m_ey_1)^2+\left[\theta_c\sqrt{s}(1-y_1)\right]^2\right)\left((2m_eM_a)^2+\left[\theta_c\sqrt{s}(1-y_1)\right]^2\right)}, \tag{2.133}$$

where the critical angle θ_c is defined as in [47]. We don't report here the full integrated cross section since its equation is extremely long (but can be recovered analytically). We write however the leading term of σ_{ESA} when expanded in m_e:

$$\sigma_{ESA} = \lambda_{ee\gamma^4}\lambda_{a\gamma\gamma}^2\frac{s^2 - M_a^4 + 2M_a^2 s\log\left(\frac{M_a^2}{s}\right)}{4(2\pi)^3 s(2M_am_e)^4} + \mathcal{O}\left(m_e^{-3}\right). \tag{2.134}$$

The m_e^{-4} dependence comes from eq. 2.29, where we saw that $q_{\min}^2 \sim m_e^2$.

Finally, we compare the analytical and the approximate cross section in the sSM for $e^+e^- \to e^+e^-a$. As shown in figs. 2.11, 2.12, depending on the critical angle θ_c the agreement between σ_{sSM} and σ_{ESA} is very good up to very high values of M_a. In particular, the bigger θ_c gets, the better agreement there is. However, we must remember that θ_c defines the cone in which virtual photons are emitted and still considered collinear to the electron; this means that for larger θ_c the collinearity approximation error in (2.30) and (2.126) becomes larger.

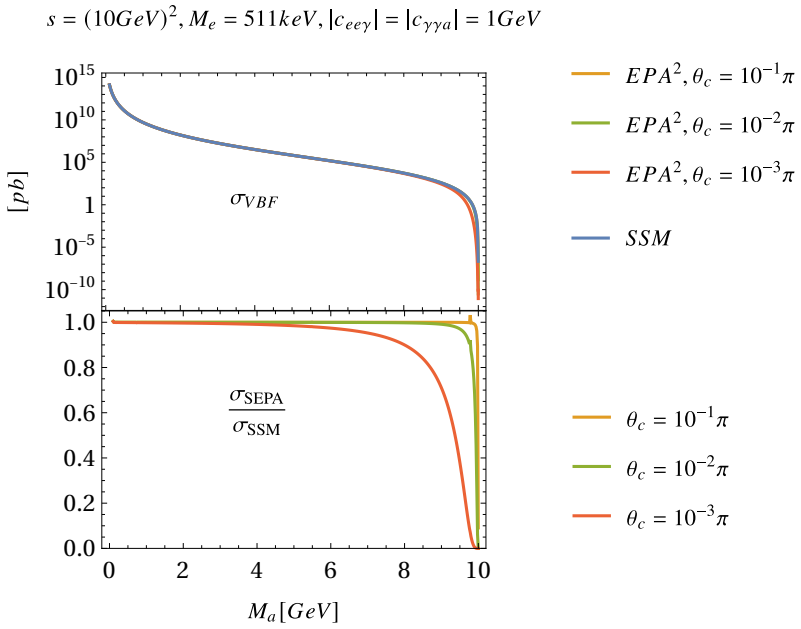

Figure 2.11. In the top panel we plot the full cross section σ_{VBF} (eq. (2.96) integrated) in the sSM and the σ_{ESA} (eq. (2.134)) including all m_e dependence for different values of θ_c. The agreement is very good up to high M_a. In the bottom panel we plot the ratio between the approximate and the full cross section for all ALP masses and for different θ_c. As we see, higher values of θ_c give a better agreement, but may spoil the collinearity approximation.

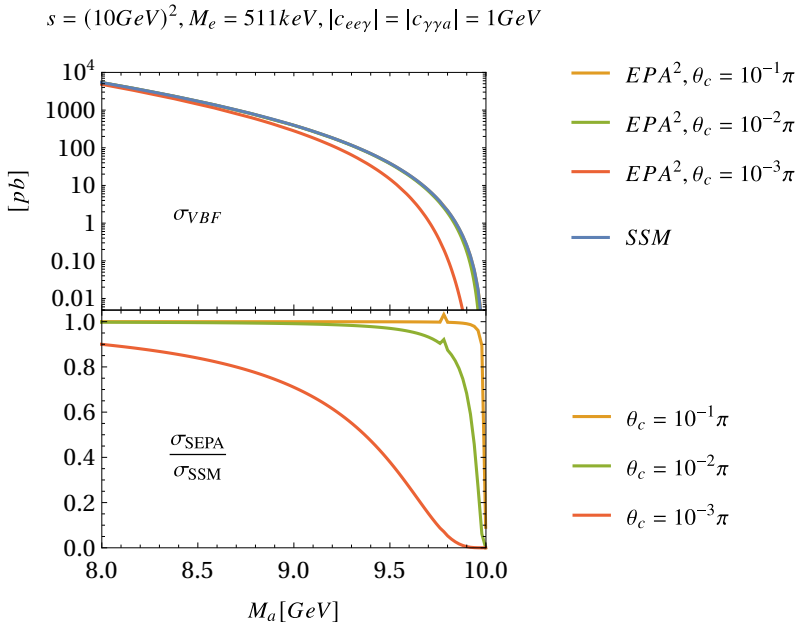

Figure 2.12. A zoom of 2.11 for high ALP masses. The difference between σ_{ESA} and σ_{sSM} becomes more evident.

Chapter 3

Visible ALP searches at Belle II

The process we will study is the ALP production at Belle II. In particular, we will start from reinvestigating the state of the art, *i.e.* the results of [40], including a brief description of the experimental apparatus of Belle II, and then we will go further by analyzing a production channel that was not considered in that work, which is Vector Boson Fusion.

3.1 State of the art

3.1.1 Experimental setup

In order to conduct sensible ALP searches, it is important to understand the experimental setup used at Belle II. All of the technical details and parameters are taken from the Belle II Physics Book [53] and from the Technical Design Report (TDR) [41].
The collider SuperKEKB is a 3 km circumference asymmetric electron-positron collider, located at the High Energy Accelerator Research Organisation in Tsukuba, Japan. It is also called a "B Factory", meaning that the main products of the collisions are B-mesons. In contrast with LHC, which can probe directly the TeV mass scale, SuperKEKB focuses instead in high-precision measurements of rare decays, and CP-violation in heavy quarks and leptons. Its goal is to probe New Physics at even higher mass scales through the indirect effects of new particles in higher order processes. The expected integrated luminosity is 50ab^{-1}. The center of mass energy of this collider is $\sqrt{s} = 10.583$ GeV, very close to the $\Upsilon(4S)$ resonance; this energy is obtained with two asymmetric beams, with the electron one having an energy of 7 GeV and the positron one having an energy of 4 GeV. This choice guarantees to record as many boosted $\Upsilon(4S) \to B^0\bar{B}^0$ decays as possible, but is completely irrelevant for our studies.
The main experimental apparatus we are interested in is the Belle II Electromagnetic Calorimeter (ECL); the final state of our processes will in fact only contain photons or electrons, and the correct identification and measurements of these particles will be crucial. The ECL is composed of CsI cells, shaped like truncated pyramids. The smallest base faces the beam pipe, with a square surface of $6 \times 6\text{cm}^2$; their height is

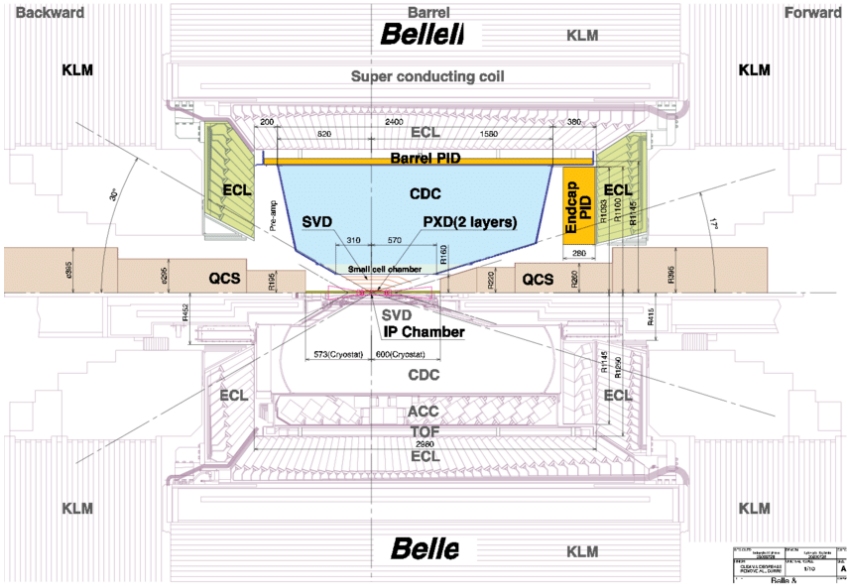

Figure 3.1. A schematic view of the Belle II detector. The ECL coverage has a gap between barrel and endcaps, that we will neglect; moreover, there are explicit arrows denoting the boundaries of the visible region for the polar angle of leptons, in the range $[17°, 150°]$.

about 16 radiation length. [1] We show a schematic view of the experimental setup [54] in fig. 3.1; even if the ECL is not uniform in its coverage, we will neglect blind spots and consider the polar angle acceptance (in the Lab frame) to be $[17°, 150°]$.

The minimal energy requested by the trigger to accept a photon candidate is, in the center of mass, $E^*_\gamma \geq 0.25$ GeV; the electromagnetic shower caused by the photon can be enclosed in a square of 5×5 cells, with the central cell being the most excited by the incoming photon. The energy resolution of the Belle II ECL is

$$\frac{\sigma_E}{E} = \sqrt{\left(\frac{0.066\%}{E}\right)^2 + \left(\frac{0.81\%}{\sqrt[4]{E}}\right)^2 + (1.34\%)^2}, \tag{3.1}$$

with the first term describing the "stochastic term", arising from statistical fluctuations in measurements of two particles with the same energy; the second term describes the "noise", that takes into account pile-ups and general noise from the electronics; finally, the constant term describes nonuniformities in the response of the detector. These can come from various causes, such as geometric imperfections of the calorimeter, from temperature gradients, from radiation damage and so on. We will assume, in the following, that the invariant mass reconstruction resolution follows a similar equation with the same parameters, due to the angular resolution being much more precise than the energy resolution.

[1] A radiation length is the mean distance over which a high energy electron remains with a fraction of $\frac{1}{e}$ of its initial energy due to Bremsstraahlung

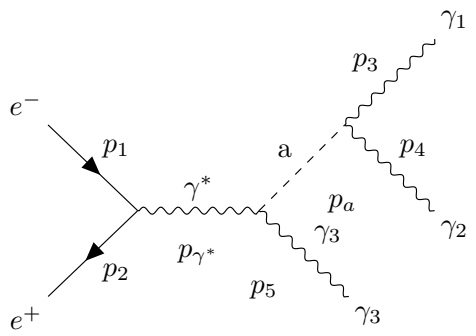

Figure 3.2. Feynman diagram of the signal process $e^+e^- \to a\gamma$, $a \to 2\gamma$, also called "ALP-strahlung".

3.1.2 Repeating ALP-strahlung results

The state of the art results in ALP searches at Belle II are presented in [40]. There, the authors only consider the process

$$e^+e^- \to \gamma\, a, \tag{3.2}$$

which they call "ALP-strahlung" (see fig. 3.2), and then divide the study in two cases: one in which the ALP decays into two detectable photons, $a \to \gamma\gamma$, which will be called *visible decay*, and one in which the decay products of the ALP are not detectable (for example, the final state is composed of dark matter particles), which will be called *invisible decay*.
The first step of our work was the complete reproduction of the visible reach of [40]. We wrote the BSM model containing the ALP with the Mathematica package FeynRules [55], which produced the UFO output needed for MadGraph [56] to simulate the events. As explained, the signal we generated was

$$e^+e^- \to a\,\gamma, \;\; a \to \gamma\gamma, \tag{3.3}$$

whose Feynman diagram is in fig. 3.2, while the only background we need to consider is in fig. 3.3.

$$e^+e^- \to 3\gamma. \tag{3.4}$$

Given the low center of mass energy, we can quickly expedite the simulation process by neglecting the ALP-Z interaction, which would otherwise contribute negligibly but would greatly increase the number of diagrams entering the simulation.
Our goal is to find out, for every ALP mass $M_a \in [0, \sqrt{s}]$, which is the value of the ALP-photon coupling, $g_{a\gamma\gamma}$ that would exclude, at 95% confidence level, the presence of said ALP. Of course, in order to find the strongest possible exclusion bound, we should find a way to greatly reduce the background, while at the same time maintaining the signal at the same size. This can be achieved, for example, by selecting only events that lie in a small interval around the ALP mass M_a. This cut is justified by the very narrow width of the ALP in our model: since it can only decay in 2 photons, the total width reads

$$\Gamma_a = \frac{g^2_{a\gamma\gamma} M_a^3}{64\pi}, \tag{3.5}$$

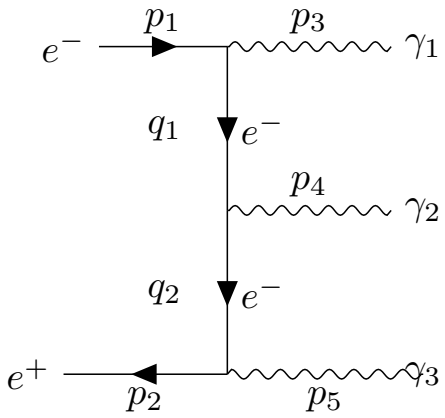

Figure 3.3. Feynman diagram of the background process $e^+e^- \to 3\gamma$.

and with some benchmark numbers, like $g_{a\gamma\gamma} = 10^{-4}$ GeV^{-1} and $M_a = 1$ GeV, we get $\Gamma_a \sim 50$ meV. We will then choose, following the investigation of the authors in [40], to consider only events that lie in an asymmetric bin around the value of the ALP mass, namely $[M_a - 3\sigma_m, M_a + 1.5\sigma_m]$, where σ_m is the same as 3.1. Due to the smallness of the ALP width, we will ensure that the signal will be fully included in this bin, while the background will be (hopefully) significantly cut.
Another important consideration regards the kinematics of our signal: the ALP-strahlung $ee \to a\gamma$ is a $2 \to 2$ process, which means that the energy of the recoiling photon is fixed to

$$E_\gamma = \frac{s - M_a^2}{2\sqrt{s}}. \tag{3.6}$$

Once again, by carving an appropriate slice around this energy value for the recoiling photon, we should be able to keep all of the signal while cutting the background.
The final observable used in [40] is the *helicity angle*, a quantity used mainly when there is an intermediate resonance. Let us briefly define this angle. Suppose you have the process $I \to R\, f_1,\ R \to f_2 f_3$. We call $p^R_{f_2}$ the four-momentum of the final particle f_2 in the rest frame of the resonance R. Similarly, we call p^I_R the four momentum of the resonance R in the rest frame of the original decaying particle I.[2] For clarity, we show a picture of the four-momenta in the two different frames in fig. 3.4. The helicity angle of f_2 is then defined as

$$\cos\theta_{f_2} = \frac{\vec{\mathbf{p}}^R_{f_2} \cdot \vec{\mathbf{p}}^I_R}{\left\|p^R_{f_2}\right\| \|p^I_R\|}. \tag{3.7}$$

If one knows which final particles come from the resonance, the computation of the helicity angle is straightforward. In our case, this does not happen. The full process is $ee \to 3\gamma$, and we need to reconstruct which photons come from the

[2]Note that this is, up to a sign in the vector part of the four-momentum, the same of p^R_I, the four-momentum of I in the rest frame of R.

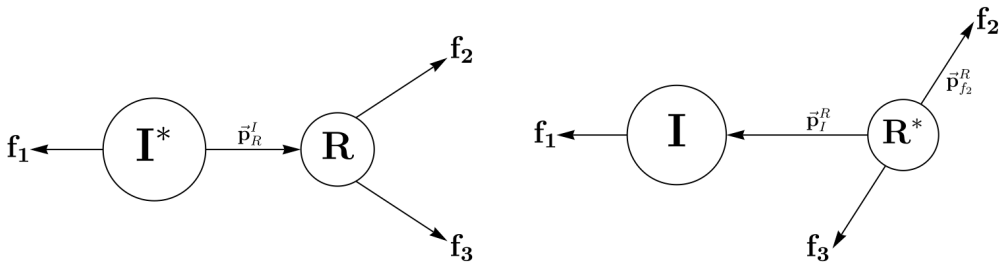

(a) I at rest. **(b)** R at rest

Figure 3.4. Four-momenta for the process $I \to Rf_1, R \to f_2 f_3$

ALP and which is the recoiling one. Following [40], we will employ two different strategies depending on the ALP mass that we describe in section 3.1.4).

3.1.3 Event Simulation

As stated before, we simulate both signal and background events with the Monte-Carlo event generator MG5_aMC@NLO [56], in the following simply called MadGraph. With this tool we can generate only events that would be detected at the experiment, allowing us to spare time by not checking if the event is actually visible in the analysis step. The user interface only allows to define symmetric cuts in the center of mass; more complicated cuts can be defined by some more or less straightforward tweaking of the fortran code in the aptly named "cuts.f" file. This will be needed for some of our analysis of the following sections, and will be explicitly stated when used.
Since our process does not care about any boosts that the asymmetric collider provides, we actually generated processes both in the Laboratory frame (with asymmetric beam energies) and in the center of mass, to double check that everything was working as intended.
The ECL is excited only by particles of energy (in the center of mass) $E^* \geq 0.25$ GeV, and this holds for both photons and leptons. The angular coverage, instead, is in the range $[17°, 150°]$ ($[22°, 158°]$) for the polar angle in the Lab (CoM), and the full $[0, 2\pi]$ for the azimuthal angle, once again for both photons and leptons (see fig. 3.1 for the schematics). This cut can be translated in a pseudorapidity acceptance range, which in the Lab is $\eta \in [-1.317, 1.901]$ ($\eta \in [-1.63, 1.63]$ in the CoM).
The final detector request that we need to implement in our simulation is less straightforward than a simple cut in energy or pseudorapidity, and is related to the spatial resolution of the ECL. From the measurements of the ECL in [41], we see that each crystal covers an azimuthal region of 48 mrad; in the polar direction, since the crystals have different inclinations to offer the largest surface to the interaction point, the coverage of each crystal decreases with the polar angle (fig. 3.1). In order to give a simpler and more conservative estimation, we will consider a constant coverage also in the polar direction, equal to the largest region, which also measures 48 mrad.

In the analysis in [40] it is not clear how the angular resolution is defined. Their request of two photons being separated by at least 5 cells does not specify in which direction this separation must occur. We decided then to analyze both the case in which we ask for n cells of distance in the polar **and** azimuthal direction (which we will call the AND cut), and n cells of distance in the polar **or** azimuthal direction (the OR cut). Explicitly, we require

$$|\theta_1 - \theta_2| > 5L \quad \&\& \quad |\phi_1 - \phi_2| > 5L \tag{3.8}$$

for the AND cut, where L is the crystal angular size, and

$$|\theta_1 - \theta_2| > 5L \quad || \quad |\phi_1 - \phi_2| > 5L \tag{3.9}$$

for the OR cut. The AND cut requires some fortran coding in the "cuts.f", because we need to define the angular distance in both directions $(\Delta\theta, \Delta\phi)$ and then impose the and cut on those quantities; the OR cut instead can be easily implemented making use of an important kinematic quantity, ΔR. We remember that the ΔR between two particles is defined as

$$\Delta R = \sqrt{\Delta\eta^2 + \Delta\phi^2}. \tag{3.10}$$

Since the polar angle θ and the pseudorapidity η are directly related, we can use an appropriate cut in ΔR, which is already coded inside MadGraph, to express the or cut.
Finally, the last consideration to make is that a photon may also impress multiple cells, and in that way it can give more information to the detector and improve the actual angular resolution. For this reason, in our analysis, we will consider different cell separations to see which effect they can have on the final reach.

We recall the ALP interactions after the electroweak symmetry breaking:

$$\mathcal{L}_{\text{ALP}} \supset -\frac{g_{a\gamma\gamma}}{4} a F_{\mu\nu}\tilde{F}^{\mu\nu} - \frac{g_{a\gamma Z}}{4} a F_{\mu\nu}\tilde{Z}^{\mu\nu}, \tag{3.11}$$

where we did not write the aZZ and aWW interactions because they are very suppressed at Belle II energies. We choose to "turn off" the mixed interaction $a\gamma Z$, as explained, because it would just contribute to computation time while being still suppressed with respect to the $a\gamma\gamma$ interaction due to the low center of mass energy, and we fix in our simulation $g_{a\gamma\gamma} = 10^{-4}$ GeV^{-1}. With these parameters, and the detector cuts explained above, we generate 10^4 signal events for various values ALP masses in the range $[0.1, 10]$ GeV.
For the background, we need firstly to define m_{LOW}, the smallest invariant mass for any couple of photons:

$$m^2_{\text{LOW}} = \min m^2_{ij} \; \forall i, j \in [1, 2, 3]. \tag{3.12}$$

We generated in total $1.5 \cdot 10^5$ events divided in "slices" of m_{LOW}. This slicing was necessary for covering in the best possible way all of the phase space; of course, each sliced generation is weighted accordingly to its cross section when they are combined to obtain the full background.

3.1.4 Analysis

Since most of the cuts happened already at generation level, the only selection we still need to implement is the cut on the helicity angles. Following [40], depending on the value of M_a there are two selection rules.

- For small M_a, we start by computing the invariant mass of all the possible photon couples, calling the lowest one m_{LOW}, as in eq. (3.12). We assume the leftover photon is the recoiling one, and we dub it γ_3, while $\gamma_{1,2}$ are the ones which invariant mass is m_{LOW}. We then compute the helicity angle of γ_1 in the rest frame of the ALP, and we introduce the quantity

$$h_1 = \left|\cos\theta_1^{ALP}\right|. \tag{3.13}$$

  An event passes the cut if

$$0 \leq h_1 \leq 0.6 \cup m_{LOW} \in [M_a - 3\sigma_m, M_a + 1.5\sigma_m], \tag{3.14}$$

  where we also selected only the events living in the bin around the ALP mass. These selection are such that the ratio $S/\sqrt{B}$ is maximized. Once again, the mass resolution σ_m is the same as 3.1.

- For large M_a, it is no longer correct to identify the ALP candidate with the smallest possible diphoton mass; we consider then the three possible photon couples, and compute the respective helicity angles. We order them by the absolute value of their cosine $h_{1,2,3}$. We identify the couple giving the smallest helicity angle, h_1, with the photons coming from the ALP, and we call γ_3 the remaining photon. The selection rules, once again chosen to maximize $S/\sqrt{B}$ then are

$$0 \leq h_1 \leq 0.9 \cup E_{\gamma_3} \in [E_{rec} - 3\sigma_E, E_{rec} + 1.5\sigma_E],\ E_{rec} = \frac{s - M_a^2}{2\sqrt{s}}. \tag{3.15}$$

After these cuts, we will have N_s (N_b) MC events for the signal (background), with a cross section $\sigma_s \pm \Delta\sigma_s$ ($\sigma_b \pm \Delta\sigma_b$). We assume the full expected luminosity of Belle II, $\mathcal{L} = 50$ ab^{-1}, and we can compute the expected events at the collider as $S = \sigma_s \cdot \mathcal{L}$ (the same holds for the background events B).
To obtain an exclusion bound on $g_{a\gamma\gamma}$ at 95% CL, we need to find the value of $g_{a\gamma\gamma}$ such that $\frac{S}{\sqrt{B}} = 2$. Since only S depends on $g_{a\gamma\gamma}$, that we fixed during our simulation, we find our bound by solving

$$\left(\frac{g_{a\gamma\gamma}}{g_{a\gamma\gamma}^{MC}}\right)^2 \frac{S}{\sqrt{B}} = 2. \tag{3.16}$$

This quantity is also subjected to an uncertainty, which depends on both the cross section uncertainty $\Delta\sigma$, due to the limited MC sample, and on the number of events ending up in the selected bin, due to the probabilistic nature of the process. Assuming a Poissonian distribution for the number of events, and assuming the luminosity to be exact, we can propagate the errors in the formula above and get

$$\frac{\delta_{g_{a\gamma\gamma}}}{g_{a\gamma\gamma}} = \frac{1}{2}\sqrt{\frac{1}{4N_b} + \frac{1}{N_s} + \frac{\Delta\sigma_b^2}{4\sigma_b^2} + \frac{\Delta\sigma_s^2}{\sigma_s^2}}. \tag{3.17}$$

The equation above makes it clear that greater contributions in the uncertainty arise when there is a low number of events surviving in the bin we chose. This also justifies our efforts to improve the coverage of the phase space by means of multiple sliced simulations, that are able to stabilize and keep low this error.
The results of our analysis are in figs. 3.5 and 3.6. The different colors represent different choices of the angular separation requested in the simulation (1,2 or 4 cells of side 24 mrad), and we repeated the analysis for both the AND and OR cut. We see how this choice is basically irrelevant for intermediate and high masses, and there is a good overlap with the reach produced by the authors of [40]. The minor differences can be explained by a different definition in the exclusion bound (the authors use a 90% CL exclusion) and a different MC simulation for the background, obtained with the software BABAYAGA. We can also see that the difference in cell separation is only appreciable at low masses; this feature can be explained by the fact that a very light ALP is very boosted; its decay products, in turn, will be closer together, and at some point will become indistinguishable (hence why the reach start worsening at some point). Finally, we note how the low mass selection becomes less reliable around $M_a = 5$ GeV, hinting that we need to change to the high mass selection rules for $M_a \gtrsim 5$ GeV.

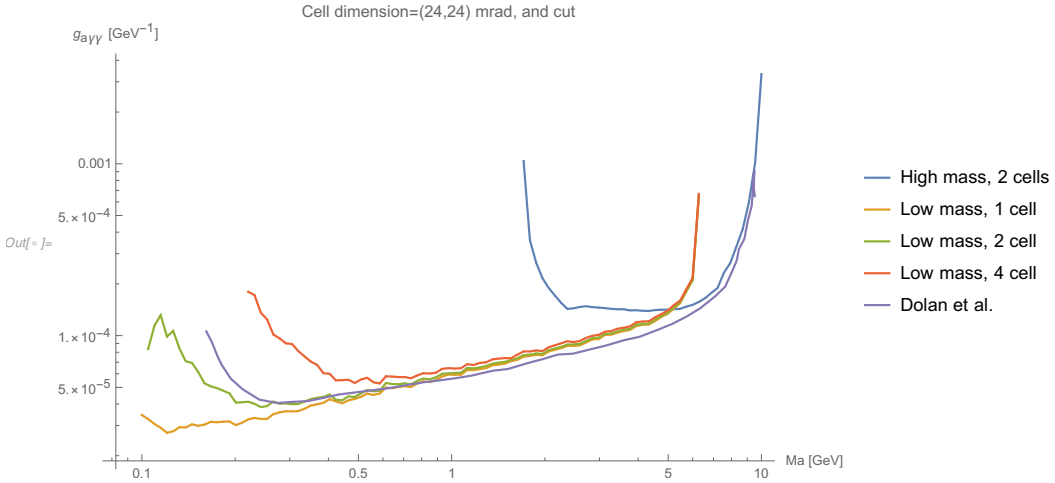

Figure 3.5. Bound on $g_{a\gamma\gamma}$ at Belle II for a luminosity of 50ab^{-1}. Angular resolution defined with the *and* cut. The purple line is taken from [40]; the yellow, green and red lines are computed with angular separation of 24, 48, 96 mrad respectively, and with the low mass cuts. The blue line is computed with the high mass cuts and angular separation of 48 mrad.

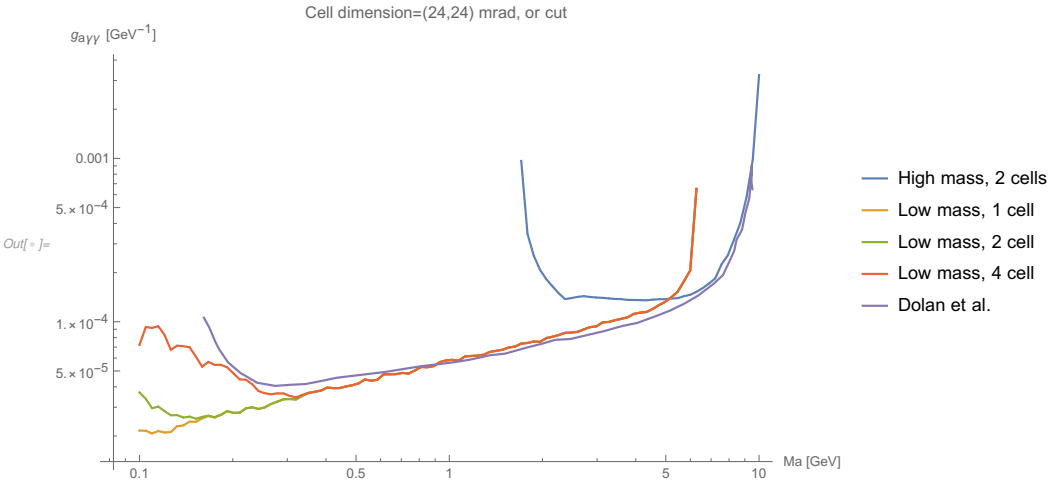

Figure 3.6. Bound on $g_{a\gamma\gamma}$ at Belle II for a luminosity of 50ab^{-1}. Angular resolution defined with the *or* cut. The purple line is taken from [40]; the yellow, green and red lines are computed with angular separation of 24, 48, 96 mrad respectively, and with the low mass cuts. The blue line is computed with the high mass cuts and angular separation of 48 mrad.

3.2 Belle II sensitivity to VBF

In this section we want to investigate the claim of [40] that Vector Boson Fusion (VBF) processes (depicted in fig. 3.7) are negligible with respect to the ALP-strahlung at Belle II when computing the sensitivity to a visible ALP. In previous parts of this work we already showed how the largest contribution to the cross section of VBF processes comes from phase space configurations in which the final leptons are basically collinear with the beam pipe. By construction, Belle II is only sensitive to particles with central rapidities, so we can expect the VBF rate to be suppressed. For this reason, we will first try and optimize a new strategy of event selections sticking with the current detector properties; in the following section we will propose a collinear upgrade of Belle II that will greatly improve the sensitivity to VBF processes.

As already stated in the previous section, for any ALP mass hypothesis we can safely assume that the ALP is very close to its resonance, so the first selection we impose is the "mass bin", meaning the invariant mass of the photon pair, $m_{\gamma\gamma}$ must be compatible with the ALP mass M_a within the detector resolution. Namely, we require

$$m_{\gamma\gamma} \in [M_a - 3\sigma_m, M_a + 1.5\sigma_m]. \tag{3.18}$$

While this selection was almost enough for the ALP-strahlung case (fig. 3.2), we need to push further down the background rate for VBF processes (fig. 3.7). In order to find the best set of event selection criteria we studied different combinations of simple cuts. For each of those, we determined what kind of selection contributed to the largest value of $S/\sqrt{B}$, and we were able to establish the efficiencies of those cuts, thus selecting the simpler ones having the biggest impact on the reach. Of course, not all cuts perform equally at all masses; we split then the search in 4 ALP

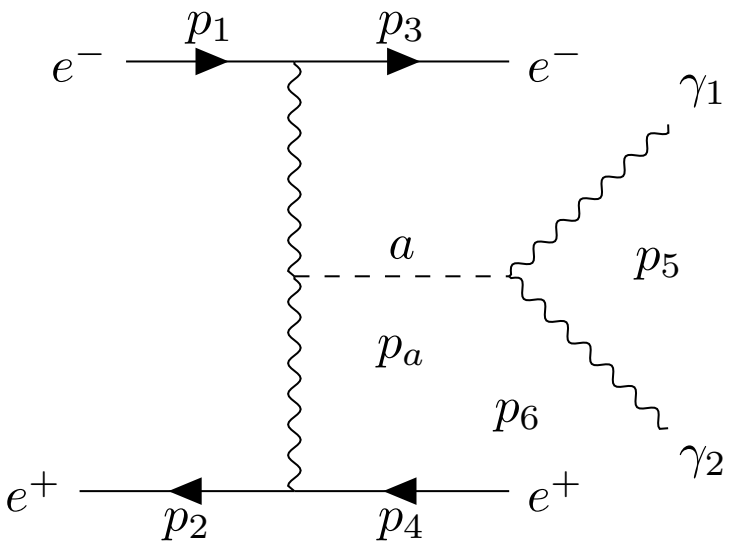

Figure 3.7. Feynman diagram of the signal process $e^+e^- \to e^+e^-a$, also called "VBF".

mass categories, with the final cuts explained in table 3.1.

M_a [GeV]	Observable	Interval
[0, 1]	$\Delta R_{l\gamma}$	[2,4.5]
	$\lvert\eta_{\gamma_1} - \eta_{\gamma_2}\rvert$	[0,0.7]
[1,3]	$\Delta R_{l\gamma}$	[1.5,4.5]
	$\lvert\eta_{\gamma_1} - \eta_{\gamma_2}\rvert$	[0,1.3]
[3,7]	$\Delta R_{l\gamma}$	[1,4.5]
	$\eta^*_{\gamma_1} \cdot \eta^*_{\gamma_2}$	[-0.3,0.3]
[7,$\sqrt{s}$]	$\Delta R_{l\gamma}$	[0.5,5]
	$\eta^*_{\gamma_1} \cdot \eta^*_{\gamma_2}$	[-0.3,0.1]

Table 3.1. We identified 4 regimes for the ALP mass, each having its set of optimizing cuts. $\Delta R_{l\gamma}$ means the angular separation for both the electron and positron from the photon, so we ask for both $\Delta R_{e^-\gamma}$ and $\Delta R_{e^+\gamma}$ to lie in the interval. When present, the asterisk stands for the usual notation of a quantity being measured in the centre of mass.

We can easily notice that most of these cuts have to do with the directions of the photons; in fact, even if the tight mass selection criterion tends to "equalize" many kinematic variables in he signal and the background, the behavior of the photons still differs due to the completely different kinematic origin.
Just as an example, we show the behaviour of the differential cross section with respect to the variable $\Delta R_{l\gamma}$ for an ALP mass $M_a = 8$ GeV for both the signal and the background in fig. 3.8a,3.8b.

After the simulation and the event selection, we are finally able to show the results for an optimized VBF search for the visible ALP at Belle II, see fig. 3.9. We

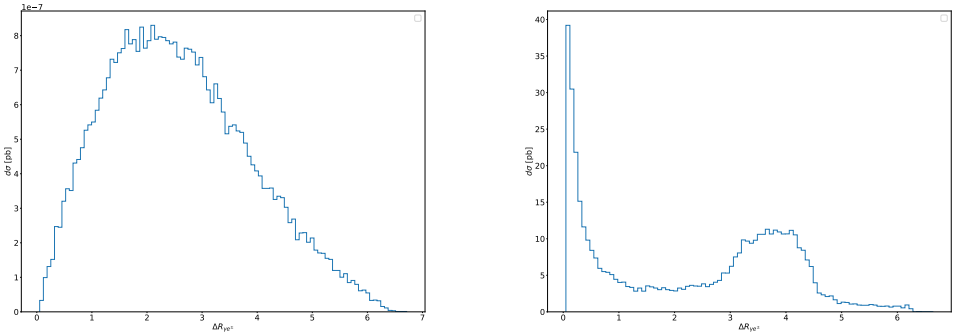

(a) Signal, M_a=8 GeV. **(b)** Background, $M_a = 8$ GeV.

Figure 3.8. Differential cross section with respect to $\Delta R_{l\gamma}$.

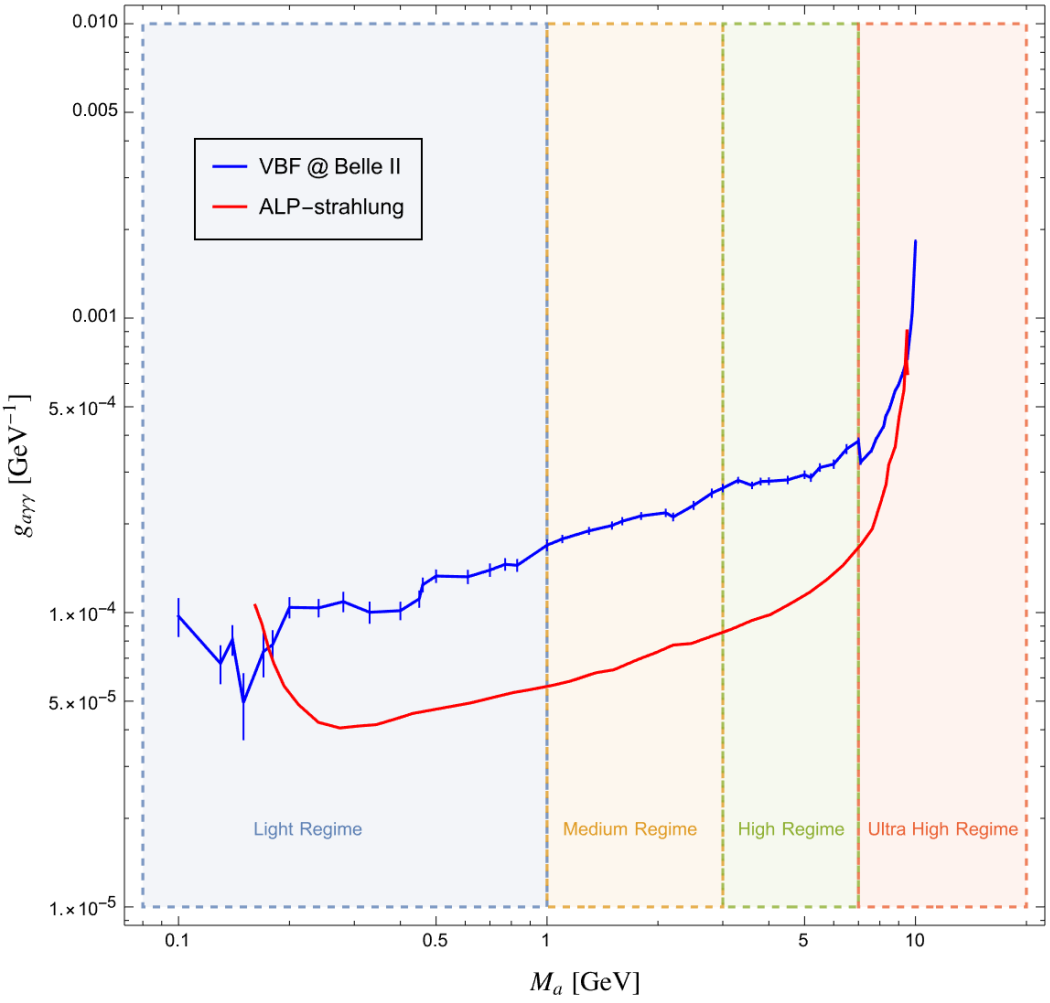

Figure 3.9. Exclusion bound for $g_{a\gamma\gamma}$ at Belle II from ALP-strahlung (yellow line, [40]) and VBF (blue line). The different background colors indicate different mass regimes, with cuts specified in table 3.1.

can see that, for most of the ALP masses, the VBF channel is actually dominated by ALP-strahlung processes; however, at both very high and very low masses, photon fusion becomes more and more important. At low masses this is caused mainly by detector resolution: in the ALP-strahlung the ALP has a very large boost, and the resulting photons will be mostly collinear, and they will not pass the photon separation constraints. At higher and higher masses, instead, it becomes harder and harder to have 3 visible photons in the final state (from the ALP-strahlung), while in the VBF we only have 2 final photons, hence the decrease in sensitivity will be slower.

3.2.1 Possible improvements: the Belle-III case

As we showed in section 2.3.3, in VBF processes the largest contribution to the cross section comes from "forward" configurations, in which the final leptons are mostly collinear with the beam pipe (hence why we call them forward). It seems obvious that the main improvement one can have is to extend the angular acceptance of the leptons to go as close as possible to the beam pipe. This is doable, for example, by using "roman pots" ([57, 58, 59]), small movable sections of the vacuum chambers containing small detectors; these detectors can track the passage of charged particles and their energy, and would not affect in any way the sensitivity to $e^+e^- \to 3\gamma$.
In order to prove this assumption, we simulated signal and background for the fusion processes with different improvements to Belle II. We explored possible extensions of the maximum values of the lepton pseudorapidity, as well as a more precise resolution in the angular distance of the photons. For the angular coverage, the results are given in fig. 3.10. Namely, we asked for $\Delta R_{ll}, \Delta R_{l\gamma}, \Delta R_{\gamma\gamma} \geq 3\,\text{mrad}$ as well as the current value $\Delta R_{ll}, \Delta R_{l\gamma}, \Delta R_{\gamma\gamma} \geq 48\,\text{mrad}$. The only cut we make for computing the reach is the usual mass selection of eq. (3.18), and the results are in fig. 3.10, with the blue line corresponding to an angular separation of 48 mrad. We find that around $\eta_l \sim 4$ the VBF becomes better than the ALP-strahlung; it is also important to note that after a certain value ($\eta_l \sim 10$) it becomes useless to try and improve the detector since the reach becomes basically constant. Inspired by existing detectors (in the experiment ALFA at LHC, [58]), we choose $|\eta_l| \leq 5$, since pushing this boundary becomes very difficult in practice, and we dub this "new" experiment Belle III. Once again, since we are only improving the lepton angular acceptance, the ALP-strahlung sensitivity at Belle III will not change; now we can compare the full cross section, for both strahlung and VBF, in the acceptance of Belle II and III (see fig. 3.11). With the Belle III improvement, the VBF cross section becomes now comparable at all masses with the ALP-strahlung.

We now try and find some optimizing cuts, as in the previous section, that will give us the best reach.
As for the fusion at Belle II, we quickly found out that the best selections came from dividing the ALP masses in four groups, each with its different cuts. They are explicitly stated in table 3.2.
Finally, we can show the result for the exclusion bound on $g_{a\gamma\gamma}$ from the VBF at Belle III (fig. 3.12). We can see that the reach would be far better than the state of the art at all masses, and this result comes just from a simple analysis.

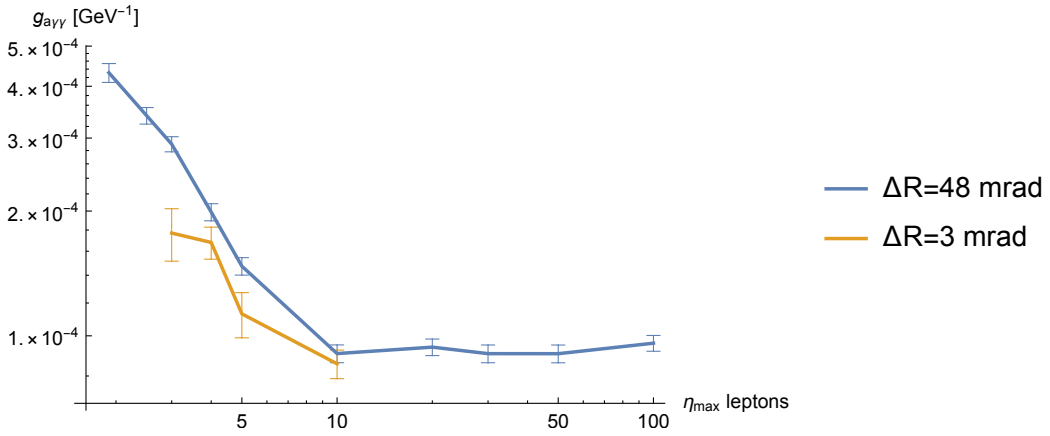

Figure 3.10. Reach for $g_{a\gamma\gamma}$ at $M_a = 8$ GeV at Belle II, with a luminosity of 50 ab^{-1}. The cut in ΔR applies to all couples of leptons and photons as explained in the text. The maximum value for the rapidity applies to both leptons.

M_a [GeV]	Observable	Interval
[0, 1]	$\Delta R_{l\gamma}$	[2.1,6]
[1,5]	$\Delta R_{l\gamma}$	[2.1,6]
	$\eta^*_{\gamma_1} \cdot \eta^*_{\gamma_2}$	[-0.5,0.5]
[5,8]	$\Delta R_{l\gamma}$	[1,6.5]
	$\eta^*_{\gamma_1} \cdot \eta^*_{\gamma_2}$	[-0.4,0.3]
[8,$\sqrt{s}$]	$\Delta R_{\gamma\gamma}$	[3,3.5]
	$\eta^*_{\gamma_1} \cdot \eta^*_{\gamma_2}$	[-0.5,0.1]
	η^*_{γ}	[-1,1]

Table 3.2. We identified 4 regimes for the ALP mass, each having its set of optimizing cuts. As in tab. 3.1,$\Delta R_{l\gamma}$ means the angular separation for both the electron and positron from the photon. When present, the asterisk stands for the usual notation of a quantity being measured in the centre of mass.

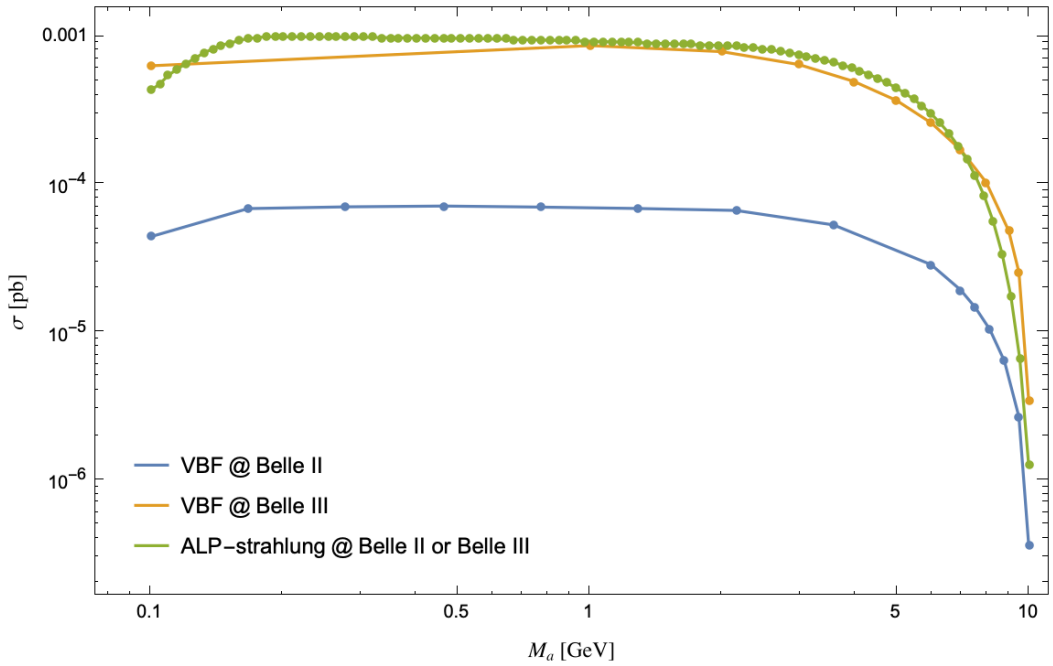

Figure 3.11. Signal cross section for different ALP masses. The blue line is the VBF at Belle II ($|\eta_l| \leq 1.6$), the orange line is the VBF at Belle III ($|\eta_l| \leq 5$) and the green line is the ALP-strahlung (same in both configurations).

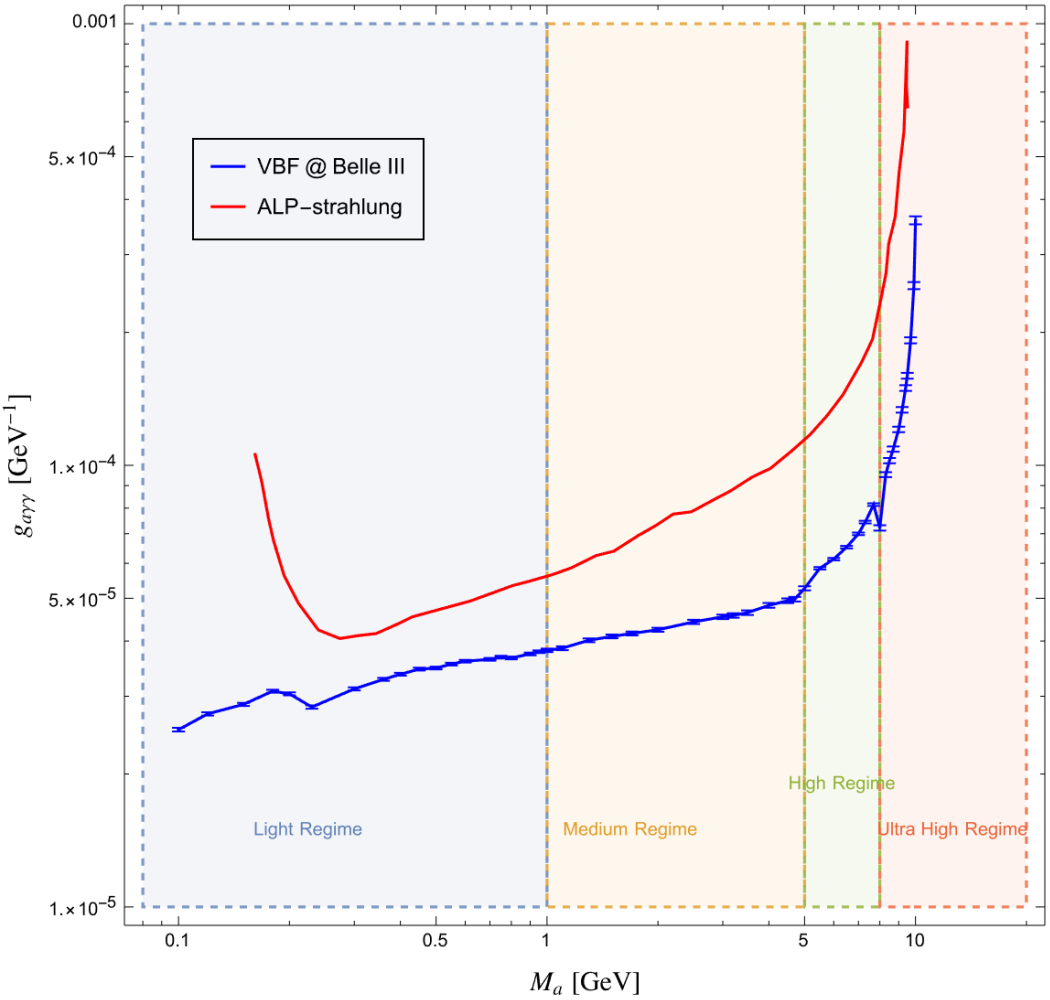

Figure 3.12. Exclusion bound for $g_{a\gamma\gamma}$ at Belle III. The blue line comes from the VBF channel, the yellow line from the ALP-strahlung. The background colors denote different mass regimes, each with their cuts, written in table 3.2.

Chapter 4

Invisible ALP searches at Belle II

4.1 Invisible decay

We will now devote our attention to the *invisible decay* of the ALP, described by the process

$$e^+e^- \to e^+e^- + \text{ inv}, \tag{4.1}$$

where the ALP coming from the signal process $e^+e^- \to e^+e^-a$ either decays outside of the detector, or decays into invisible particles such as Dark Matter.
The signal for this process comes from both the ALP-strahlung (fig. 3.2) and the VBF (fig. 3.7) channel; since we are dealing with invisible decays, and we are unable to differentiate among them, we will refer them in the following as the s- and t-channel respectively.
There are many possible backgrounds to consider; the most important ones come from QED, in particular from

$$e^+e^- \to e^+e^- + n\gamma_{inv}, \tag{4.2}$$

in which there are n invisible photons in the final state. We recall that a photon is considered invisible at Belle II if at least one of the following properties is true:

- its centre of mass energy is below the ECL threshold, namely $E^*_\gamma \leq 0.25$ GeV;
- its polar angle in the Lab frame lies outside the ECL acceptance, *i.e.* $\theta_\gamma \notin [17°, 150°]$.

Another background to consider comes from $\tau\tau$ pair production, and it's described by the process

$$e^+e^- \to \tau^+\tau^-,\ \tau \to \bar{\nu}\nu e, \tag{4.3}$$

where the invisible body is composed of four neutrinos. All other backgrounds are negligible with respect to the signal, when considering $g_{a\gamma\gamma} \sim 10^{-5}$ GeV.

In the following sections, we will first describe how collider effects force us to implement a more original strategy than the visible case, then we will define for each background how to choose appropriate selection rules that can make the background process vanish. Finally, we will show our results and how they compare to the state of the art.

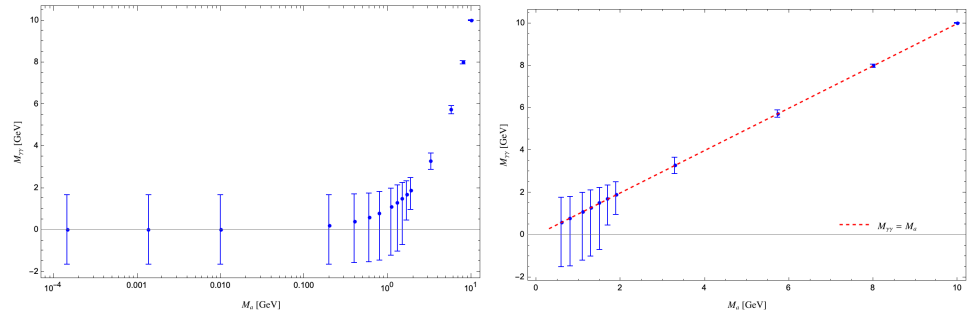

(a) Detector effects on the reconstructed mass $m_{\gamma\gamma}$.

(b) Zoom of fig 4.1a for large values of $m_{\gamma\gamma}$.

Figure 4.1. For each ALP mass generated as an extremely narrow Breit-Wigner distribution, the smearing procedure transforms it into a Gaussian curve. The extremes of the distribution are shown as the lowest and highest point of each bar; small masses are smeared so much that it is impossible to distinguish them from one another. At higher masses, the smearing becomes more contained, and the missing mass becomes useful again in the selection procedure. For those values, $\sigma_M/M < 1$, so we can use the mass bin as a selection rule just like we did in the visible case. In red, we draw the exact correspondence $m_{\gamma\gamma} = M_a$

4.1.1 Collider effects

When dealing with processes involving invisible particles, one should be careful in blindly using the MonteCarlo generated data. In fact, the simulation will produce outputs for an ideal detector, where the four-momenta of particles are defined basically with no error. This is of course unrealistic, but it is a very good approximation when dealing with observables that suffer from very small uncertainties; however, in the invisible case, this is not generally true. The kinematic quantities of invisible particles in fact must be obtained from some combination of the visible ones, and for this reason may be prone to large cancellations. The uncertainty on these quantities, on the other end, can add up. This causes quantities that would be very narrowly distributed from the MC simulation to broaden; the clearest example is the invisible ALP mass. We can compute this quantity only by squaring the missing momentum, which in turn is defined in terms of the incoming and outgoing leptons:

$$M_a^2 = p_{\text{miss}}^2 = (p_{in} - p_{out}^{e^+} - p_{out}^{e^-})^2. \tag{4.4}$$

While before smearing M_a^2 has an extremely narrow width for any value of M_a, detector effects makes so that values of $M_a \lesssim 1$ GeV gain a very broad width, about 2 GeV. This is depicted in figures 4.1a,4.1b.

4.1.2 Signal characterization

Since we cannot use the missing mass to select candidate ALP events (at least for low values of this mass), we need to focus on quantities that are stable under smearing. For example, a remarkable property of our signal is that the signal $e^+e^- \to e^+e^-a$ will have a single invisible body with maximal energy and central rapidity. Moreover, being a single particle, it is also on shell. No background process

can mimic this feature, since the invisible body must be composed of multiple particles. In fig. 4.2 we schematically show what phase space regions are occupied by the signal and by the background before the smearing: the blue triangle contains all the possible phase space for missing energy and momentum when the invisible body is composed of multiple particles; the only boundaries we imposed are

$$\sqrt{s} \geq E_{\text{miss}} \geq |\vec{p}_{\text{miss}}| \tag{4.5}$$

$$E\text{miss}, \vec{p}_{\text{miss}} \geq 0. \tag{4.6}$$

The colored lines represent where a single particle of fixed mass lies in this phase space. Before the smearing, the signal distributions follow very closely the lines, having a very narrow width; after the smearing, these distributions broaden in both directions, but the effect is smaller at higher energies. For all these reasons, we decide to select the signal region depicted in orange in fig. 4.2, which will contain most of the signal and a small background after the smearing; due to its elongated shape, we call it the *cigar* region. Explicitly, this cut has the form

$$10.437 \text{ GeV} - 1.155 E_{\text{miss}} \leq |\vec{\mathbf{p}}_{\text{miss}}| \leq 12.437 \text{ GeV} - 1.155 E_{\text{miss}}. \tag{4.7}$$

It is interesting to see that this apparently strange cut can actually be approximated by a cut in the visible mass $m_e e$ (the mass of the combined visible electrons). In fact, we can write (in the COM)

$$E_{\text{miss}} = \sqrt{s} - E_{vis}, \ |\vec{p}_{\text{miss}}| = -|\vec{p}_{vis}|; \tag{4.8}$$

as well as isolines for a single body of energy E_{miss}, we can draw isolines for a body of energy E_{vis}, which will have the same three-momentum (in absolute value) but are mirrored with respect to the vertical line $E_{\text{miss}} = \sqrt{s}/2$.
We will show now how, for both QED and τ backgrounds, this selection adds up with other, background specific, cuts to completely erase the background. We stress that this result comes from analytical reasons, namely the presence of an unaccessible region of phase space for invisible photons.

4.1.3 QED background

As stated before, the QED background comes from the process

$$e^+e^- \to e^+e^- + n\gamma_{inv}, \tag{4.9}$$

where $n \geq 2$. It is useful to separate the invisible photons in two categories, depending on their energy:

- a **soft** photon has an energy below the ECL threshold, and can have any rapidity. At Belle II, $E^*_\gamma < 0.25$ GeV;
- a **hard** photon has an energy above the ECL threshold, but a pseudorapidity outside of the detector acceptance; at Belle II, $\left|\eta^*_\gamma\right| > 1.6$. If the pseudorapidity is positive, we say that the photon lie in the *forward* cone (around the beam line, with an angle in the centre of mass of 22°); otherwise, it lies in the *backwards* cone.

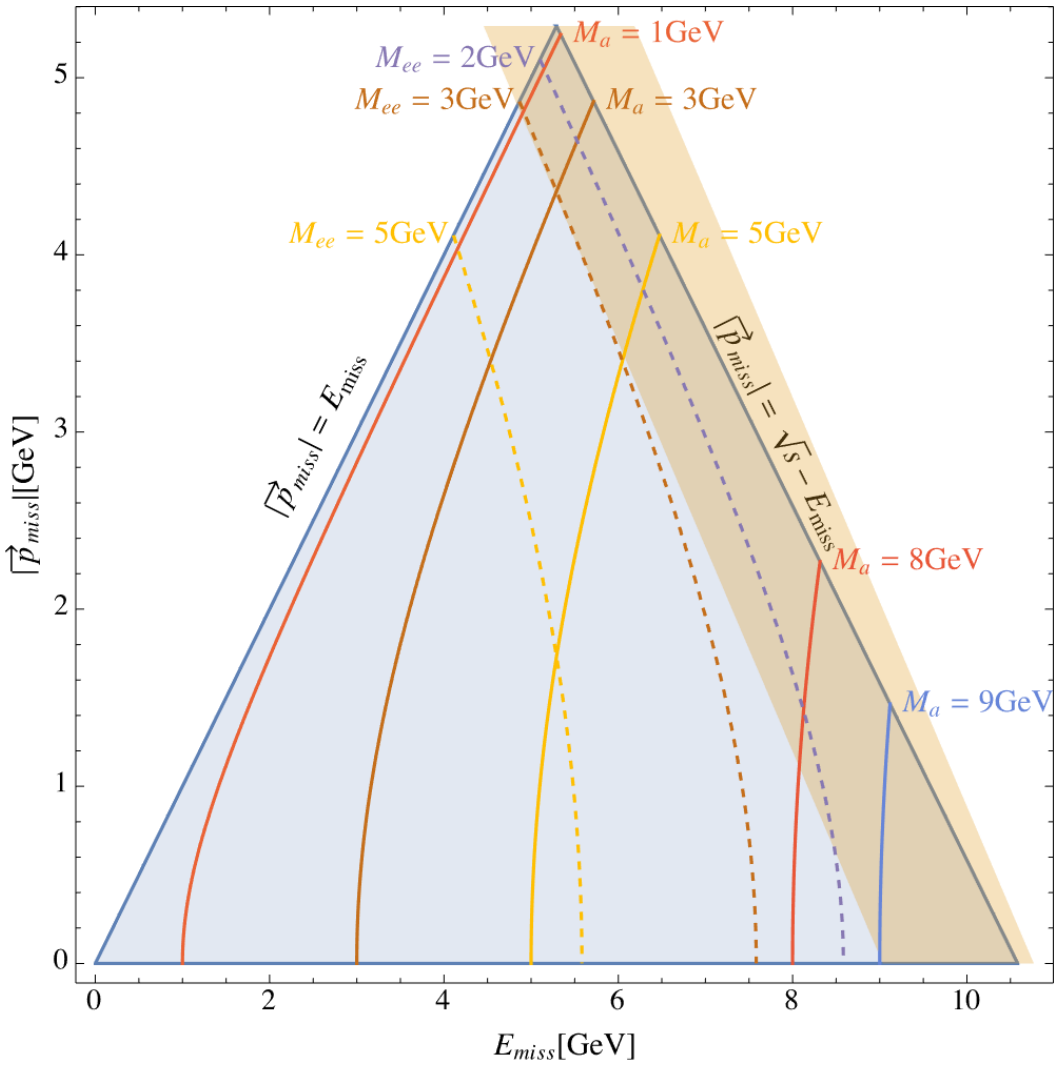

Figure 4.2. Phase space occupied by an invisible body in E_{miss} and $|\vec{\mathbf{p}}_{\text{miss}}|$. The blue region contains all the available phase space when the invisible body is composed of multiple particles; the colored lines represent the allowed phase space for a single invisible particle of fixed mass. The orange area is the signal region, which encloses most of the signal and selects a small part of the background after the smearing. It can also be approximated by a cut in m_{ee}.

In these QED background processes, the total number n of invisible photons is composed of n_S soft and n_H hard photons.

The most relevant soft photons in our considerations however are those whose energy is very close, but still below the threshold; we then stress that the nomenclature "soft" does not imply any need for resummation due to large logarithmic effects that may spoil the convergence of the perturbative series. For this reason, we will conduct our analysis at fixed order n in QED, with $n = n_S + n_H$.

Using the cigar selection defined in the previous section automatically implies that $E_{\text{miss}} > 4.5$ GeV, as shown in fig. 4.2. In the following, this lower bound will always be implied, but in most cases this bound is not very stringent and will be refined by the cigar cut itself.
Since we know that our signal is peaked for central rapidities, we want to know if it is possible to obtain such values for all values of the missing mass. We are particularly interested in the small missing mass case, since that is the most difficult to simulate when imposing central rapidities.

The first possibility happens when all invisible photons are soft. In this case, all rapidities are allowed, and it is easy to check that one can also generate small masses. However, we need to fulfil the requirement

$$E_{\text{miss}} > 4.5 \text{ GeV}, \tag{4.10}$$

so even if all soft photons are just below the energy threshold, we have

$$n_S E_{thr} \geq 4.5 \text{ GeV} \Rightarrow n_S \geq 18. \tag{4.11}$$

Having at least 18 photons in the final state means that this cross section will be completely suppressed with respect to our signal, and we can neglect it.

More interesting properties arise when at least one photon is hard; in this case, as we will show, there is actually a forbidden region for the photons, whose size depends on the number of invisible photons and the kinematic properties of such particles. Computing analytically the boundary of such region is too complicated; however, we can consider all different configurations of photons that may arise, and try to approximate this boundary for each configuration, checking if the region of vanishing rapidity and missing mass is accessible or not.

1 hard photon

When only 1 hard photon is present, the main contribution to the rapidity comes from it. Let us call this photon h_1. The most effective way to have a central rapidity requires that h_1 is as central as possible; since it cannot enter the detector acceptance, its polar angle will be as close to the threshold as possible, so $\theta_{h_1} = \alpha_{thr}$ (without loss of generality, we can consider h_1 to be forward; at Belle II, $\alpha_{thr} = 22°$ in the centre of mass).

On the other hand, soft photons must be the hardest they can on the opposite side to pull the rapidity to 0; all their energies, E_i, $i \in [2, n]$ must be equal to E_{thr}. Moreover, if all the soft photons are aligned, their total invariant mass will automatically vanish.

Suppose now that all soft photons lie at an angle α_s. We can define the four-momenta

$$p_1 = E_1(1, \sin\alpha_1, 0, \cos\alpha_1) \tag{4.12}$$

and

$$p_s = E_s(1, \sin\alpha_s, 0, \cos\alpha_s). \tag{4.13}$$

The missing momentum will be

$$p_{\text{miss}} = p_1 + (n-1)p_s = (E_{\text{miss}}, E_1 \sin\alpha_1 + (n-1)E_{thr}\sin\alpha_s, 0, E_1\cos\alpha_1 + (n-1)E_{thr}\cos\alpha_s), \tag{4.14}$$

where we rotated away the azimuthal component by redefining the axes for simplicity. It is easy to compute the solution to the requirement $\eta^*_{\text{miss}} = 0$:

$$\eta^*_{\text{miss}} = 0 \Leftrightarrow \cos\alpha_s = \cos\alpha_1 \left(1 - \frac{E_{\text{miss}}}{(n-1)E_{thr}}\right). \tag{4.15}$$

From this we can compute the minimal number of soft photon needed for a vanishing missing rapidity, by imposing that the cosine on the left side is in the correct interval:

$$\cos\alpha_s \in [-1, 1] \Leftrightarrow n \geq 1 + \frac{\cos\alpha_1 E_{\text{miss}}}{E_{thr}(1+\cos\alpha_1)}. \tag{4.16}$$

With the explicit Belle II values, we find that $n \gtrsim 10$.

Two hard photons

This case can be split once again in two categories, one of which is trivial. In fact, if both of the hard photons lie in the same cone (say both forward), the smallest possible η^*_{miss} is achieved when both photons are as central as possible, namely $\alpha_1 = \alpha_2 = \alpha_{thr}$. The two photons however will behave as a single hard photon, so the number of soft photons needed for a vanishing rapidity will be obtained as in the previous section.

It is much more interesting to consider what happens when two hard photons lie in opposite cones. Let us start from the simpler case of only two total photons (n=2), and write the four-momenta explicitly:

$$p_1 = E_1(1, s_1, 0, c_1),\ p_2 = E_2(1, s_2 c_\phi, s_2 s_\phi, c_2), \tag{4.17}$$

where we used the notation $s_{1,2} = \sin\theta_{1,2}$, $c_{1,2} = \cos\theta_{1,2}$, $s_\phi = \sin\phi$. At this point we need to explicitly maintain $\phi_1 \neq \phi_2$ since we are interested in the general case; however, we will see that the minimization on the missing mass will automatically set $\phi_1 = \phi_2$. Without losing generality, we can consider $\theta_1 \in [0, \alpha_{thr}]$, $\theta_2 \in [\pi - \alpha_{thr}, \pi]$. The condition for vanishing rapidity is

$$(p_{\text{miss}})_z = (p_1 + p_2)_z = 0, \tag{4.18}$$

but this configuration implies a lower bound on the missing mass, which is

$$\min(m^2_{\text{miss}})_{n_H=2} = 2E_1E_2(1 - \cos(\alpha_2 - \alpha_1)), \tag{4.19}$$

with α_1, α_2 the limiting angles for the forward and backwards cone respectively.
Let's prove this statement. We can use the two constraints on the missing energy and vanishing rapidity to decrease the independent variables of m^2_{miss}: we can in fact write

$$E_2 = E_{\text{miss}} - E_1 \tag{4.20}$$
$$E_1 = -E_2 \frac{\cos\theta_2}{\cos\theta_1} \tag{4.21}$$

where the first equation comes from the definition of missing energy, and the second from imposing $\eta^*_{\text{miss}} = 0$. The missing mass now becomes

$$m^2_{\text{miss}} = m^2_{\text{miss}}(\theta_1, \theta_2, \phi; E_{\text{miss}}) = \tag{4.22}$$
$$= \frac{2E^2_{\text{miss}} \cos\theta_1 \cos\theta_2 (\cos\theta_1 \cos\theta_2 + \sin\theta_1 \sin\theta_2 \cos\phi)}{(\cos\theta_1 - \cos\theta_2)^2}.$$

Since we are interested in finding the extremal points of this function, we need to find where the gradient of this function vanishes. The easiest first step is to consider the derivative with respect to ϕ:

$$\frac{\partial m^2_{\text{miss}}}{\partial \phi} = -\frac{2E^2_{\text{miss}} \cos\theta_1 \cos\theta_2 \sin\theta_1 \sin\theta_2}{(\cos\theta_1 - \cos\theta_2)^2} \sin\phi, \tag{4.23}$$

which clearly vanishes only if $\phi = 0$ or $\phi = \pi$. This latter case however will clearly maximize the missing mass, since it will put the two invisible photons back to back; for this reason, we will only focus on $\phi = 0$ for the following discussion.
We can now explicitly write the remaining two derivatives computed in $\phi = 0$:

$$\left.\frac{\partial m^2_{\text{miss}}}{\partial \theta_1}\right|_{\phi=0} = E^2_{\text{miss}} \cos\theta_2 \cos\tfrac{\theta_1 - \theta_2}{2} \csc\Big(\tfrac{\theta_1 + \theta_2}{2}\Big)^3 \tag{4.24}$$
$$\left.\frac{\partial m^2_{\text{miss}}}{\partial \theta_2}\right|_{\phi=0} = E^2_{\text{miss}} \cos\theta_1 \cos\tfrac{\theta_1 - \theta_2}{2} \csc\Big(\tfrac{\theta_1 + \theta_2}{2}\Big)^3. \tag{4.25}$$

Since we defined $\theta_1 \in [0, \alpha_{thr}]$, $\theta_2 \in [\pi - \alpha_{thr}, \pi]$, there is no way to annihilate these two derivatives. Since the gradient is never 0, we conclude that there are no local minima, and the absolute minimum will be somewhere on the contour of the variables domain. In particular, we need to study the sign of the derivatives to see where the function is increasing or decreasing. In order to do so, it is convenient to introduce a different parametrization with the simple substitutions

$$\theta_1 \to x_1,\ \theta_2 \to \pi - x_2,\ x_{1,2} \in [0, \alpha_{thr}]. \tag{4.26}$$

Since the threshold angle at Belle II is $\alpha_{thr} = 22\,\text{deg} = 0.12$, we can expand the derivatives in powers of x_1, x_2, obtaining

$$\boldsymbol{\nabla} m^2_{\text{miss}} = \begin{pmatrix} \frac{\partial m^2_{\text{miss}}}{\partial x_1} \\ \frac{\partial m^2_{\text{miss}}}{\partial x_2} \\ \frac{\partial m^2_{\text{miss}}}{\partial \phi} \end{pmatrix} = -\frac{E^2_{\text{miss}}}{2} \begin{pmatrix} x_1 + x_2 \cos\phi \\ x_2 + x_1 \cos\phi \\ -x_1 x_2 \sin\phi \end{pmatrix} + \mathcal{O}\Big(x^2_{1,2}\Big). \tag{4.27}$$

On $\phi = 0$, the derivatives with respect to x_1, x_2 are both negative, hence the function is always decreasing in its domain; the absolute minimum will be then obtained for

maximum values of x_1, x_2, which will correspond to the extremal configuration $\theta_1 = \alpha_{thr}$, $\theta_2 = \pi - \alpha_{thr}$, as stated in eq. 4.19.

We have shown now that for two invisible photons in the final state, there will always be some values of m^2_{miss} below $m_{\text{miss}}(x_1 = x_2 = \alpha_{thr}, \phi = 0)$ (as in eq. (4.19)) that cannot be obtained, if we simultaneously ask for $\eta^*_{\text{miss}} = 0$. If this result holds also for three invisible photons, we are able to identify a region of the phase space which is inaccessible to the background [1], while still being populated by the signal.

Three photons

Once again we need to catalogue all the possible energy configurations of the photons (up to renaming of the indices):

- $\gamma_1, \gamma_2, \gamma_3$ all soft; this case does not satisfy the missing energy bound, so we ignore it.
- γ_1 hard, γ_2, γ_3 soft; we studied this configuration in par. 4.1.3.
- γ_1 and γ_2 hard, γ_3 soft;
- $\gamma_1, \gamma_2, \gamma_3$ all hard.

The last configuration will be the focus of next section; for now, let us consider the case of two hard and one soft photons.
Without losing generality, suppose that γ_1 is forward and γ_2 is backwards; moreover, even if the range of the polar angle of γ_3 is all the domain $[0, \pi]$, we can restrict to only consider the soft photon having positive rapidities, which means $\theta_3 \in [0, \pi/2]$.
We need to define the four-momenta of the photons:

$$p_1^{(3)} = E_1^{(3)}(1, s_1^{(3)}, 0, c_1^{(3)}) \tag{4.28}$$

$$p_2^{(3)} = E_2^{(3)}(1, s_2^{(3)} \cos\phi_{12}, s_2^{(3)} \sin\phi_{12}, c_2^{(3)}) \tag{4.29}$$

$$p_3^{(3)} = E_3^{(3)}(1, s_3^{(3)} \cos\phi_{13}, s_2^{(3)} \sin\phi_{13}, c_3^{(3)}) \tag{4.30}$$

$$p_{\text{miss}}^{(3)} = p_1^{(3)} + p_2^{(3)} + p_3^{(3)},\ m_3^2 := (m_{\text{miss}}^{(3)})^2 = (p_{\text{miss}}^{(3)})^2. \tag{4.31}$$

Once again, we used the shortcut notation for the angles as in eq. 4.17, and the superscript (3) denotes quantities in the 3 photon case.
For now, let us set $\phi_{12} = \phi_{13} = 0$, following what we found in the previous case; we claim that this is both the easiest and the minimizing configuration; in the next paragraph we will prove that this is indeed the case. The three body missing mass computed at $\eta^*_{\text{miss}} = 0$ and with a fixed value of E_{miss} will then be

$$m_3^2(\phi_{12} = 0, \phi_{13} = 0, \eta^*_{\text{miss}} = 0) = (m^2_{\text{miss}})_{(2)} + \\ + \frac{8E_3 E_{\text{miss}} \sin\left(\frac{\theta_1-\theta_2}{2}\right) \sin(\theta_1-\theta_2) \sin\left(\frac{\theta_1-\theta_3}{2}\right) \sin\left(\frac{\theta_2-\theta_3}{2}\right)}{(\cos\theta_1 - \cos\theta_3)^2} \tag{4.32}$$

$$- \frac{4E_3^2 \sin^2\left(\frac{(\theta_1-\theta_3)}{2}\right) \sin^2\left(\frac{\theta_2-\theta_3}{2}\right)}{\sin^2\left(\frac{\theta_1+\theta_2}{2}\right)}, \tag{4.33}$$

[1] with 4 or more photons in the final state, the background cross section becomes negligible with respect to the signal cross section with $g_{a\gamma\gamma} = 10^{-5}$. In addition those multiple photons can be clustered reducing to a 3 photon situation.

where $(m^2_{\text{miss}})_2$ has the same analytic form of the squared mass of the two hard photons . The last term is always negative; with our angle definitions, $\theta_1 - \theta_2 < 0$ and $\theta 2 - \theta_3 > 0$, as their respective sines; if $\theta_3 > \theta_1$, the second term in 4.32 is also negative, and the 3 body missing mass can be smaller than the two body one, which breaks our property. However, we must remember that γ_3 is soft, and its energy must be below the ECL threshold; since $(m^2_2) \sim E^2_{\text{miss}}$,

$$\frac{m^2_3 - m^2_2}{E^2_{\text{miss}}} = -\frac{E_3}{E_{\text{miss}}}\kappa + \mathcal{O}\left(\left(\frac{E_3}{E_{\text{miss}}}\right)^2\right), \tag{4.34}$$

where κ is a positive number. We can expect then the correction to the missing mass due to having an extra soft photon to be very small; in fact, plugging in Belle II parameters and setting Emiss = 5 GeV, $\theta_3 = \pi/2$ (which is the worst case scenario) , we get

$$\min m^2_2 = 21.5 \text{ GeV}^2 \;\; \min m^2_3 = 20.9 \text{ GeV}^2. \tag{4.35}$$

In conclusion, adding one soft photon to the final state does indeed reduce the smallest possible missing mass, but there is still some region of the phase space with vanishing rapidity that cannot be accessed by the background. Adding more soft photons reduces the bound on m_{miss} further, but the rate of interactions also drops, and will not be significant for our study.

4.1.4 Inaccessible phase space: a general proof

We now want to demonstrate what we found in the previous paragraphs more formally, and justifying the assumptions we made. We start with a final state comprised of an arbitrary number of hard photons, that can be divided in only two categories: backwards or forward. We want to find what values of m^2_{miss} and η^*_{miss} are actually accessible.

Let us start from the definition of missing momentum:

$$p_{\text{miss}} = \sum_{i=1}^{n} p_i, \quad p_i = E_i \begin{pmatrix} 1 \\ \sin\theta_i \cos\phi_i \\ \sin\theta_i \sin\phi_i \\ \cos\theta_i \end{pmatrix}, \tag{4.36}$$

where $i = 1, 2, \ldots, n$ identifies each invisible photon. We can write the missing mass as

$$m^2_{\text{miss}} = p^2_{\text{miss}} = \left(\sum_{i=1}^{n} p_i\right)^2 = 2\sum_{i=1}^{n}\sum_{j>i} 2p_i \cdot p_j, \tag{4.37}$$

where we used the on-shellness of the photons ($p^2_i = 0 \;\forall i$).
Let us introduce some shorthand notations for compactness:

$$c_i := \cos\theta_i, \;\; s_i := \sin\theta_i, \;\; c_{ij} = c_i c_j + s_i s_j \cos(\phi_i - \phi_j). \tag{4.38}$$

With this, we can rewrite the missing mass as

$$m^2_{\text{miss}} = 2\sum_{i=1}^{n}\sum_{j>i} E_i E_j (1 - c_{ij}); \tag{4.39}$$

each term in this sum is positive, so the minimum for m^2_{miss} must be positive as well. In order to find said minimum, we first compute the gradient and then find out where it vanishes:

$$\boldsymbol{\nabla} m^2_{\text{miss}} = \left(\frac{\partial m^2_{\text{miss}}}{\partial E_i}, \quad \frac{\partial m^2_{\text{miss}}}{\partial \theta_i}, \quad \frac{\partial m^2_{\text{miss}}}{\partial \phi_i}\right), \; i = 1, \dots, n. \tag{4.40}$$

Even if, in principle, we would have to compute $3n$ derivatives, m_{miss} is invariant under the exchange $p_i \longleftrightarrow p_j \; \forall i, j$; this means that we can fix $i = 1$, and study just three derivatives; all the other terms will be obtained directly by an appropriate change of index. We then have

$$\frac{\partial m^2_{\text{miss}}}{\partial E_1} = 2 \sum_{j=2}^{n} E_j (1 - c_{1j}) \tag{4.41}$$

$$\frac{\partial m^2_{\text{miss}}}{\partial \theta_1} = 2 \sum_{j=2}^{n} E_1 E_j (s_1 c_j - c_1 s_j \cos(\phi_1 - \phi_j)) \tag{4.42}$$

$$\frac{\partial m^2_{\text{miss}}}{\partial \phi_1} = 2 \sum_{j=2}^{n} E_1 E_j (s_1 s_j \sin(\phi_1 - \phi_j)). \tag{4.43}$$

The only way to make eq. 4.41 vanish is to put the parenthesis equal to zero; from the definition of c_{ij} in (4.38), this can only happen if $\theta_1 = \theta_j$, $\phi_1 = \phi_j \; \forall j$. Extending this result to all the other photons, we find that we need to have $\theta_i = \theta_j$ and $\phi_i = \phi_j$ to have a vanishing gradient. Incidentally, $\phi_i = \phi_j$ annihilates Eq. (4.43), and, combined with $\theta_i = \theta_j$, also makes Eq. (4.42) vanish. This configuration is the only one in which the gradient is 0, and with a simple substitution one can check that this is in fact the absolute minimum for m^2_{miss}:

$$\min_{\text{unconstrained}} m^2_{\text{miss}} = 0. \tag{4.44}$$

Of course, we could have found this result just by inspection; the missing mass can be zero only if all invisible photons are perfectly collinear to one another, so that the composite body may actually be seen as a new, invisible photon, with energy equal to the total missing energy. Writing explicitly the gradient, however, will be useful for the next step, when we will apply some constraints on the energies and polar angles.

Constrained Minimization

Now we want to show how it is possible to have a lower bound on the missing mass different than zero when we impose some constraints. Let us write explicitly the constraints on the missing energy and rapidity of the invisible body:

$$\begin{cases} \sum_{i=1}^{n} E_i \geq E_{\text{miss},cut} = 5 \text{ GeV} \\ p_{\text{miss},z} = \sum_{i=1}^{n} E_i c_i = 0 \\ \theta_i \in ([0, \alpha_{thr}] \cup [\pi - \alpha_{thr}, \pi] \quad \text{if} \quad E_i \geq E_{thr}) \cup ([0, \pi] \quad \text{if} \quad E_i < E_{thr}). \end{cases} \tag{4.45}$$

An important thing to notice is that these constraints do not involve ϕ; this means that the cylindrical symmetry of the problem remains unspoiled. To find the constrained minimum, we still need to satisfy eq. 4.41-4.43, making sure that the

energies and angles lie in the subspace identified by eq. (4.45). However, since the domain of ϕ is not changed by the constraints, we can still use the previous solution to eq. (4.43), and choose $\phi_i = \phi_j \ \forall i, j$, as we did in section 4.1.3 and eq. (4.23).

Let us only consider configurations in which all n photons are "hard", *i.e.* their energy is above the threshold. This means that we can clearly separate them into "forward" ($\theta_i \in [0, \alpha_{thr}]$), and "backward" ($\theta_i \in [\pi - \alpha_{thr}, \pi]$). We will then have n_F forward and n_B backward photons, with $n_B + n_F = n$; with this, we will show that the minimizing configuration for m^2_{miss} is obtained when we have effectively just one forward an one backward photon, each aligned to the boundary of its visibility, and each with half the total missing energy. This conclusion will hold independently of the number of photons, or the detector characteristics.

We start from the missing mass, which we can split in three parts:

$$m^2_{\text{miss}} = \left(\sum_{i=1}^{n_F} p_i\right)^2 + \left(\sum_{j=1}^{n_B} p_j\right)^2 + 2\sum_{i=1}^{n_F}\sum_{j=1}^{n_B} p_i \cdot p_j =: m^2_F + m^2_B + m^2_{BF}. \tag{4.46}$$

For the minimization of this sum we aim at finding a configuration that minimizes the last term on the constraints while, at the same time, puts at an absolute minimum each of the first two terms. We can do that by exploiting the n_F theta angles that describe the four-momenta of the photons in the forward cone and similarly for the backward photons.
We start from the last term, m^2_{BF}. Explicitly,

$$m^2_{BF} = 2\sum_{i=1}^{n_F}\sum_{j=1}^{n_B} E_i E_j [1 - \cos(\theta_i - \theta_j)]; \tag{4.47}$$

we should note that we set $\phi_i = \phi_j$, so that c_{ij} is simplified. If we try and minimize on the constraints of eq. (4.45) this quantity, we find that the minimum can be obtained when the angular distance $\theta_i - \theta_j$ is minimal, for any two photons. However, we need to remember that, due to our constraints, the photons indexed with i live in the forward cone, those with the index j live in the backward cone. This means that the minimum angular distance cannot vanish, but can only happen if all photons are aligned along the edge of the respective cones. Explicitly, we can write

$$\theta_i = \theta_F = \alpha_{thr} \ \forall i, \qquad \theta_j = \theta_B = \pi - \alpha_{thr} \ \forall j, \tag{4.48}$$

so that

$$\min m^2_{BF} = 2[1 - \cos(\theta_F - \theta_B)] \sum_{i=1}^{n_F}\sum_{j=1}^{n_B} E_i E_j. \tag{4.49}$$

With this choice of angles, we are automatically minimizing the first two terms as well: in fact, if all forward (backward) photons are aligned to one another, we automatically have $m^2_F = 0$ ($m^2_B = 0$). Moreover, this is their absolute minimum; with this in mind, we can state that the angular minimization for the missing mass gives actually the result in eq: 4.49.

Now we also need to consider the energy configuration that minimizes m^2_{BF}; keeping in mind that all forward and backward photons are collinear, we can simplify

this configuration by just taking two composite fourmomenta, which we can write explicitly as

$$p_{F,B} = E_{F,B}(1, \sin\alpha_{thr}, 0, \pm\cos\alpha_{thr}), \qquad E_{F,B} = \sum_{i=1}^{n_{F,B}} E_i. \tag{4.50}$$

Due to the peculiar angular configuration that corresponds to the absolute minimum of m_F^2, m_B^2, m_{BF}^2, the missing mass does not depend any longer on single energies, but is just a function of their sum. We can now trade 2 of the photon energies with the sums E_F, E_B, and solve the constraints using them. In fact, we can rewrite eq. (4.45) as

$$\begin{cases} E_{\text{miss}} = E_F + E_B \\ \cos\alpha_{thr}(E_F - E_B) = 0, \end{cases} \tag{4.51}$$

which are solved by $E_F = E_B = \dfrac{E_{\text{miss}}}{2}$. Then we can write

$$m^2_{\text{miss}} \to 2E_F(E_{\text{miss}} - E_F)[1 - \cos(\theta_F - \theta_B)]; \tag{4.52}$$

if we compute the derivative $\frac{\partial m^2_{\text{miss}}}{\partial E_F}$, we can easily see that it vanishes if $E_F = \frac{E_{\text{miss}}}{2}$, i.e. the constraints are solved onto the minimizing energy configuration. The value of this lower bound is exactly the same as the case with two photons, and reads

$$\min m^2_{\text{miss}} = E^2_{\text{miss}} \cos\alpha^2_{thr} \qquad \blacksquare \tag{4.53}$$

Soft photon effect

As we did explicitly in the three photon case, we want to find out how much the inaccessible phase space changes when we add a number of soft photons in the final state. We already know that the minimum of the missing mass will decrease, and that the maximal effect for this happens when the soft photons are as hard as they can be ($E_{s_i} \lesssim E_{thr}\,\forall i$) while flying perpendicular to the beam axis, so that the constraint $\eta^*_{\text{miss}} = 0$ still holds. Calling n_H, n_s the number of hard and soft photons respectively, we can write the constraints in missing energy and rapidity as

$$E_{\text{miss}} \qquad = \sum_{i=1}^{n_H} E_i + \sum_{j=1}^{n_s} E_j \tag{4.54}$$

$$\eta^*_{\text{miss}} \quad = 0 = \sum_{i=1}^{n_H} E_i c_i + \sum_{j=1}^{n_s} E_j c_j. \tag{4.55}$$

Putting all soft photons perpendicular to the beam axis gives us exactly the same constraints as before (eq. 4.45), but with a reduced E_{miss}:

$$\sum_{i=1}^{n_H} E_i = E'_{\text{miss}} := E_{\text{miss}} - \sum_{j=1}^{n_s} E_j \tag{4.56}$$

$$\sum_{i=1}^{n_H} E_i c_i = 0. \tag{4.57}$$

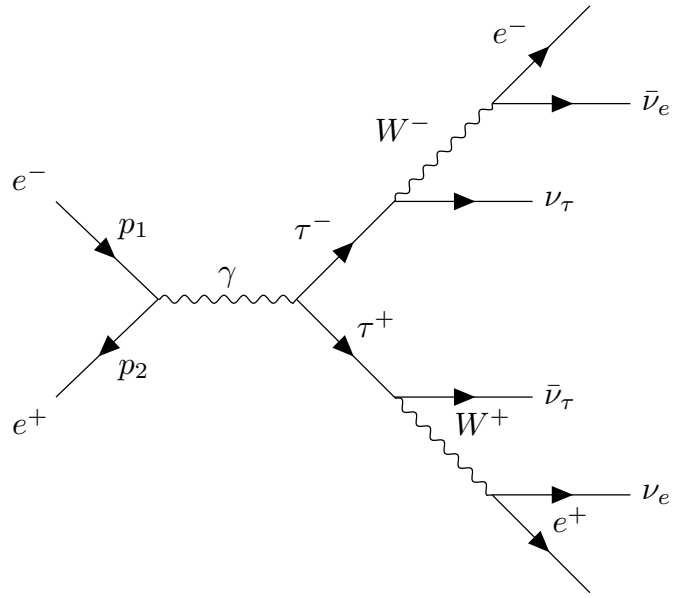

Figure 4.3. Feynman diagram for the process $e^+e^- \to \tau^+\tau^-, \tau^\pm \to e^\pm\nu\bar{\nu}$.

If we now compute the missing mass, remembering that $\theta_s = \pi/2$ for all soft photons, we get the lower bound

$$\min m^2_{\text{miss}} = E^2_{\text{miss}} \cos^2 \alpha_{thr} - 2E_s E_{\text{miss}} \sin \alpha_{thr}(1 - \sin \alpha_{thr}) - E_s^2(1 - \sin \alpha_{thr})^2, \tag{4.58}$$

where we defined $E_s = n_s E_{thr}$. This value is manifestly smaller than eq. 4.53.

In conclusion, we showed that the QED background with n invisible photons indeed has an inaccessible region in the $(m_{\text{miss}}, \eta^*_{\text{miss}})$ space; this region becomes smaller and smaller as n increases, until it vanishes, but it grows in size when increasing the missing energy constraint.

4.1.5 Background from $\tau\tau$

In this section we describe some remarkable features of the $\tau\tau$ background (fig. 4.3) that allow us to render it negligible. Specifically this scattering can be factorised in three simpler processes whose kinematics is principally driven by the smallness of the τ mass with respect to the beam energy.

The first step is to show how we are able to suppress the background when assuming low ALP mass. The crucial observation to remove the $\tau\tau$ background is that they are produced on shell, from which it follows that the final $e^\pm$ energies are correlated.

The $e^+e^- \to \tau^+\tau^-$ scattering can be considered separately from each of the $\tau^\pm$ decays. The $2 \to 2$ scattering has a simple kinematics: in the center of mass (CoM) the τs are back to back, with polar angle θ, and have energy $E^*_\tau = \dfrac{\sqrt{s}}{2}$. Define $\mathcal{F}_{\tau,z}$ the CoM frame rotated such that the τs fly along the z axis. In the τ^- rest frame, a body of mass m_τ decays in two back to back bodies, one e^- of mass M_e

and one (composite) $N^- = (\bar{\nu}_e \nu_\tau)$ of mass $\mu^- \in [0, m_\tau - M_e]$, where the superscript $-$ does not denote an electromagnetic charge, but rather which τ is the parent. The electron and the N^- fly along a line of angle θ_- and, in the τ^- rest frame, their energies are respectively

$$\begin{aligned} E_{e^-}^{(\tau^-)} &= \frac{M_e^2 - \mu_-^2 + m_\tau^2}{2m_\tau} \\ E_{N^-}^{(\tau^-)} &= \frac{-M_e^2 + \mu_-^2 + m_\tau^2}{2m_\tau}. \end{aligned} \tag{4.59}$$

These results are identically valid for the positive branch too. For our considerations, we boost both N^- and N^+ to the $\mathcal{F}$ frame. We do not lose generality by making the following simplifications:

- $M_e \to 0$, because due to the Belle II acceptance the $e^\pm$ energy has a lower bound $E^\pm \geq E_0 = 0.25$ GeV $\gg M_e$;
- a double antler[2] decay instead of the full process: $p_0 \to \tau^+\tau^-, \tau^\pm \to e^\pm N^\pm$, with $p_0 := e^+ + e^-$, where we do not consider that neutral bodies are composite; in other words a $1 \to 4$ decay rather than a $2 \to 6$ complicated scattering;
- the masses of the composite objects $\mu_- = \mu_+ = 0$: as is evident from eqs 4.59, the final electrons are allowed to a bigger phase space in this configuration, while the missing momentum phase space is not shrunk. If we then can find some selection that kills the τ background for $\mu^\pm = 0$, we are sure that backgrounds with $\mu^\pm > 0$ will not populate that phase space. This will serve our aim of setting lower/upper bounds on the observable kinematic quantities.

In this framework we are left with 3 degrees of freedom: the angles of the $e^\pm$ with respect to the direction of flight of the τs and ϕ, the angle among the planes of the decay products of the $\tau^\pm$. Hence in the CoM of Belle II, the final state four-momenta will be:

$$\begin{aligned} p(e^-) &= \frac{m_\tau}{2}\Lambda_-(1, s_-, 0, c_-) \\ p(N^-) &= \frac{m_\tau}{2}\Lambda_-(1, -s_-, 0, -c_-) \\ p(e^+) &= \frac{m_\tau}{2}\Lambda_+(1, s_+c_\phi, s_+s_\phi, c_+) \\ p(N^+) &= \frac{m_\tau}{2}\Lambda_+(1, -s_+c_\phi, -s_+s_\phi, -c_+) \\ p_{\text{miss}} &= p(N^-) + p(N^+), \end{aligned} \tag{4.60}$$

where $\Lambda_\pm$ is the Lorentz matrix that boosts from the $\tau^\pm$ rest frame to the CoM and $s_x = \sin\theta_x, c_x = \cos\theta_x, x = +, -, \phi$, all considered in the appropriate τ rest frame. Two properties emerge from eqs 4.60, affecting respectively the low and high mass selection.

[2]This notation was introduced in [60] to describe a process in which a heavy particle decays into two visible SM particles and two missing particles via two on-shell intermediate particles.

Low mass

For low values of m_{miss}, since the energies of final state $e^{\pm}$ are correlated, in most cases they will not be able to satisfy the constraints imposed by the signal region (see section 4.1.6); in fig. 4.4 we show how the background drastically dies out when we apply the "cigar" selection of the signal region of eq. (4.7). Furthermore, we identify an hyperbolic boundary that can ensure that no $\tau\tau$ events will pass our selection. The reason for this shape can be understood by looking at the approximation of eq. (4.7) with a cut in $m_e e$. In fact, we can always write

$$m_{ee} = E_{e^+} E_{e^-} c_{ee}, \tag{4.61}$$

where $c_e e$ is the cosine of the angle between the two charged leptons. Fixing $m_{ee} \leq \bar{m}_{ee}$ with our cut, we can easily see how we get an hyperbolic relation between the energy of the positron and of the electron, described in eq. (4.69).

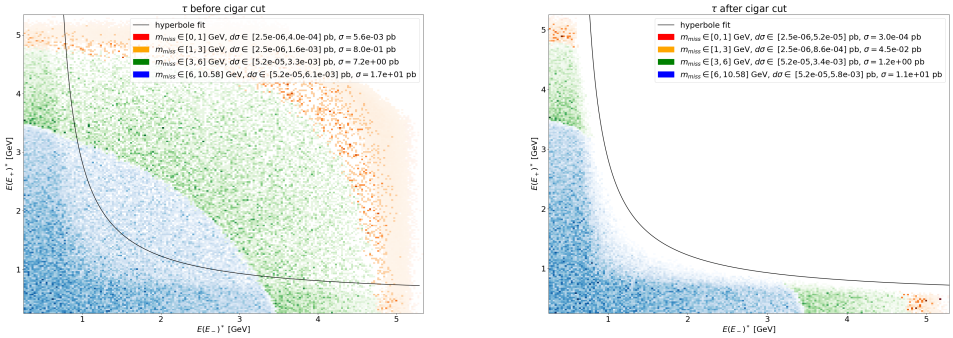

Figure 4.4. Simulated τ backgrounds before (left) and after (right) applying the signal region selections (cigar cut). Darker bins correspond to higher cross sections; the black hyperbole is defined in 4.1.6. Only events under this line survive.

Large mass

In regards to high masses, we exploit the fact that the τs are considerably boosted in the CoM frame, implying that they produce their decays products within a cone along their direction of flight. In simulations the above observation on the hyperbole is not effective. Still, we can rely on angular correlations of the e^+ and e^- due to the boost of the $\tau\tau$ events. In particular, we found the distribution of the cosine of the angle between e^+ and e^- in the CoM, c_{ee}, always starts from -1 regardless of the m_{miss} selection; if small and intermediate masses are selected, the distribution is peaked around -1 and has a tail toward $c_{ee} \to 1$. The bigger the selected mass, the further this tail manages to reach. We claim this behaviour can be explained through this simplified scattering $e^+e^- \to \tau^+\tau^-, \tau^{\pm} \to e^{\pm}N^{\pm}$ we are considering. The boost on $e^{\pm}$ projects the $[0, \pi]$ domain of their angles in $\tau^{\pm}$ rest frame non linearly in a $[0, \pi]$ image, such that $e^{\pm}$ and $N^{\pm}$ tend to be emitted close to the $\tau^{\pm}$ axis; hence, the cosine of the angle between e^+ and e^- in the CoM tends to be close to -1, as depicted in 4.5. In this figure, we we call $\mathcal{F}^{\pm}$ the rest frame of $\tau^{\pm}$; $\cos\theta_{-}^{\mathcal{F}^-}$

is the cosine of the electron polar angle in the τ^- rest frame; $\cos\theta^*_-$ instead is the cosine of the electron polar angle in the Belle II CoM frame. In both cases, the polar angle is measured from the τ line of flight. In order to go from a frame to the other, we perform a Lorentz boost along the z axis, with $\beta = 0.94$, obtained from the explicit values of m_τ and $\sqrt{s}$ at Belle II. The blue line of fig. 4.5 represents the mapping of $\cos\theta^{\mathcal{F}^-}_-$ into $\cos\theta^*_-$ due to the Lorentz transformation, namely

$$\cos\theta^*_- = \frac{\cos\theta^{\mathcal{F}^-}_- + \beta}{\beta\cos\theta^{\mathcal{F}^-}_- + 1}. \tag{4.62}$$

An analogous result holds for the e^+ angles, which are depicted in the yellow line.

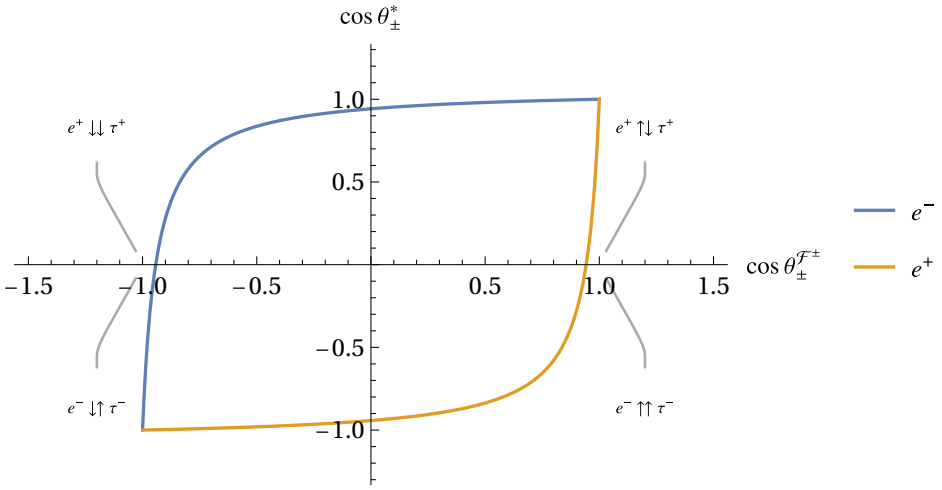

Figure 4.5. Map between the polar angle of the e^+ in the τ^+ rest frame and the polar angle in the Belle II COM for $\beta = 0.94$, see eq. 4.62.

Since we are neglecting the $\tau^- \to e^-\nu_e\bar{\nu}_\tau$ matrix element for this section, we can pretend $\cos\theta^{\mathcal{F}^-}_-$ is uniformly distributed. It follows that the mean $\cos\theta^*_-$ is

$$\langle\cos\theta^*_-\rangle = \frac{\beta_- - \epsilon^2\,\mathrm{arctanh}\beta_-}{\beta_-^2} \tag{4.63}$$

$$= 1 + \epsilon^2\left(\frac{1}{2} + \log\frac{\epsilon}{2}\right) + \mathcal{O}(\epsilon^4\log(\epsilon)) \tag{4.64}$$

$$\epsilon^2 := \frac{4m_\tau^2}{s} = 0.11 \tag{4.65}$$

$$\beta_- := \sqrt{1-\epsilon^2} \tag{4.66}$$

In numbers, $\langle\cos\theta^*_+\rangle = +0.84$, $\langle\cos\theta^*_-\rangle = -0.84$, which means the final electrons tend to be aligned to their parent. Since the τs are back to back, $\langle c_{ee}\rangle \sim -1$.

The missing mass under the assumption of $\mu^\pm = 0$ is

$$m^2_{\text{miss}} = 2p(N^-)\cdot p(N^+) = 2E(N^-)E(N^-)(1 - c_{NN}), \tag{4.67}$$

which is maximal when the neutral bodies energies $E(N^\pm)$ are big and they fly in opposite directions ($c_{NN} \to -1$). Both of these properties can be obtained if we

align each $N^{\pm}$ to the parent $\tau^{\pm}$ direction of flight: in this way the boost form the τ rest frame to the CoM keeps them back to back and maps their energies onto their CoM maximum. Consequently, $e^{\pm}$ fly in opposite directions with respect to their parent τ, and the boost will make their energy small in the CoM. Although small angle windows in the $\mathcal{F}^{\pm}$ frames are allowed to $e^{\pm}$ in order to get a big mass, the big boost projects them onto almost all the $[0, \pi]$ domain. This explains why bigger c_{ee} are reached when we ask for larger masses and why the peak on $c_{ee} \sim -1$ broadens. Our simulations show that these effects are enhanced by the SM matrix element, therefore in next section we use as a selection rule

$$c_{ee} > 0.4 \tag{4.68}$$

for large values of M_a.

4.1.6 Event selection

We divide our analysis in three regimes with different selections: one for small masses ($m_{\text{miss}} < 6$ GeV), one for high masses ($m_{\text{miss}} \in [6, 8]$ GeV), one for ultra-high masses ($m_{\text{miss}} > 8$ GeV). This splitting is necessary because the inaccessible region for the background closes around $m_{\text{miss}} \sim 6$ GeV. On the other hand, the higher we push m_{miss}, the more similar signal and background become, so our selections become less and less refined.
In the following paragraphs we will always deal with smeared events; for an overview of our smearing procedure, see the appendix A.3.

Small mass analysis

The first selection we impose is the signal region cut, also called cigar cut, described in eq. (4.7). It must be included in the Fortran file "cuts.f" when simulating events in MadGraph, in order to avoid generating useless events that will be cut a posteriori.

The hyperbole cut implemented to completely kill the $\tau\tau$ background only involves the final electron energies; it is applied after the MC events are generated, and only allows for events above the positive branch to pass the cut. Numerically,

$$E_+^* > 0.5 \text{ GeV} + \frac{1.06 \text{ GeV}^2}{E_-^* - 0.54 \text{ GeV}}. \tag{4.69}$$

In fig. 4.4 we can see that the area around the boundary imposed by the signal region cut is appropriately populated, so that we can be sure that when we claim to be background free it is not an artefact of poor MC simulations.

Finally, we apply a parabolic cut to kill the QED background after the signal region selection is applied.

High mass analysis

For high enough masses, the smearing procedure still allows us to select events based on the missing mass. For each nominal ALP mass, we select an interval $[m_{low}, m_{high}]$ such that

$$m_{low} \leq m_{\text{miss}} \leq m_{high}. \tag{4.70}$$

M_a[GeV]	m_{low} GeV	m_{high} GeV
6.31	5.94	6.68
6.50	6.14	6.86
7.00	6.69	7.31
7.5	7.17	7.83
8.00	7.73	8.27
8.50	8.24	8.76
9.00	8.76	9.24
9.50	9.30	9.70

Table 4.1. Optimized missing mass selections for both high and ultra-high mass searches. On both signal and background we set $m_{low} \leq m_{\text{miss}} \leq m_{high}$.

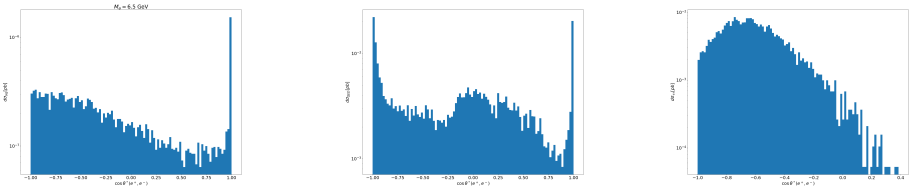

(a) Signal **(b)** QED **(c)** $\tau\tau$

Figure 4.6. Cross section distributions with respect to the **angular distance among final electrons** ($c_{ee} := \cos\theta_{ee}$) in the CoM frame. The benchmark MC mass is 6.5 GeV, and we can clearly see the peak in the signal around $c_\pm \to 1$. When $M_a \to \sqrt{s}$, the enhancement around $c_\pm \to -1$ becomes more and more important. In the background we select missing masses in the interval 6.3 GeV $\leq m_{\text{miss}} \leq$ 6.7 GeV. We can see how $c_\pm < 0$ values are preferred, both in the QED and in the $\tau\tau$ case

The values of m_{low}, m_{high} are taken from fig. 4.1b, and are reported in table 4.1.

Another selection in the high mass regime comes from the angular distance between final electrons. As anticipated, we select events having

$$c_\pm := \cos\theta(e^+, e^-)^* \geq 0.4. \tag{4.71}$$

This selection is also corroborated by what can be seen in figs. 4.6a, 4.6b,4.6c, where we see how the signal is peaked around $c_\pm \sim 1$ while most of the QED and τ backgrounds are cut away.

Finally, since the backgrounds don't have any particular feature in the missing rapidity distribution, while the signal prefers central missing rapidities, we impose a rapidity cut of the form

$$-0.5 \leq \eta^*_{\text{miss}} \leq 0.5. \tag{4.72}$$

The distributions in rapidity for the signal and both the backgrounds are represented in figs. **??**, **??**,**??**

4.2 Results

With all the selections explained in the previous section, we are finally able to plot our results in fig. 4.8. In this case, the reach is obtained in two different ways. For

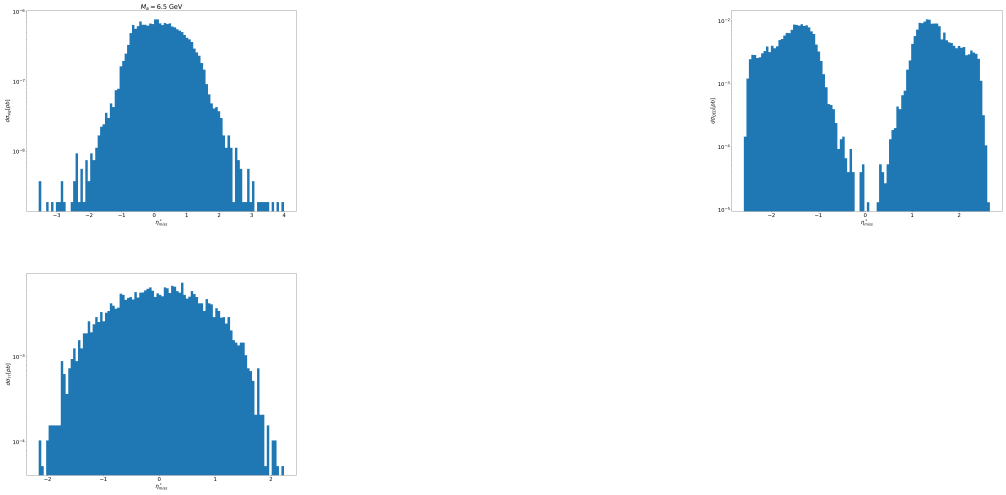

Figure 4.7. Cross section distributions with respect to the **missing rapidity** (η_{miss})in the CoM frame. In the **left** picture we plot the signal, in the **middle** picture the QED background, in the **right** picture the $\tau\tau$ background. The benchmark MC mass is 6.5 GeV. For the background, we select missing masses in the interval 6.3 GeV $\leq m_{\text{miss}} \leq$ 6.7 GeV.

low masses, when we are able to render all the backgrounds negligible, we compute the 95% exclusion on $g_{a\gamma\gamma}$ by imposing $S = 3$. For large masses, when we are dealing again with a background much larger than the signal, we recur again to computing the 95% exclusion bound on $g_{a\gamma\gamma}$ from the equation $S/\sqrt{B} = 2$.
We can see how, even if our signal cross section is much smaller than the mono-γ search of [40], we can still obtain a competitive reach by selecting only the regions inaccessible to backgrounds. For low masses, we are able to propose a **high purity** search, opposed to the *high statistics* of [40]. Moreover, even when higher masses prevents us to use the high purity search, VBF processes should still be able to probe ALP masses close to $\sqrt{s}$ without any problems, while the mono-γ search is limited by photon triggers to ALP masses below 8.6 GeV [40].

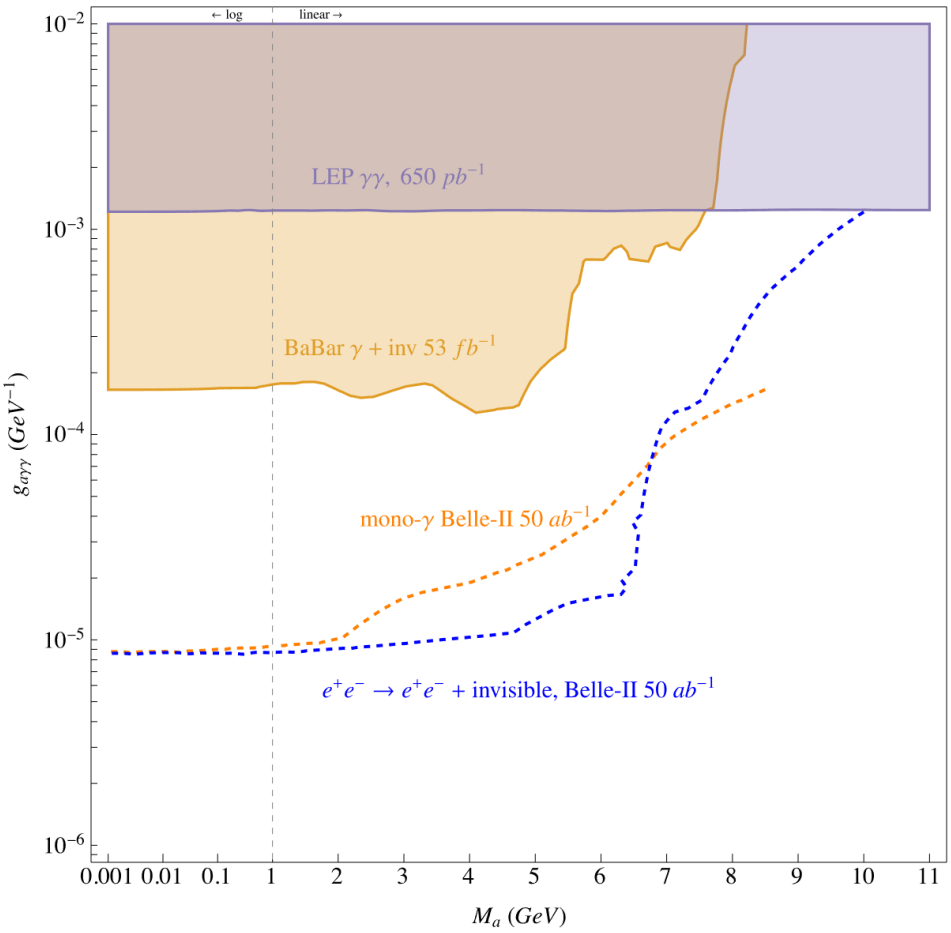

Figure 4.8. Belle II sensitivity to invisible decay of an ALP (blue). The orange dashed line is taken from figure 4 in [40], where the signal is defined by the process $e^+e^- \to \gamma a$, $a \to$ invisible.

Chapter 5

Conclusion

In this thesis we studied the production of Axion-Like Particles (ALP) from e^+e^- scattering at Belle II, and in particular we focused on the Vector Boson Fusion (VBF) production channel. This process was often neglected in the literature, and we wanted to investigate if the claim of this process being subdominant was actually true.
The first step was to compute the production cross section, in the most analytical way possible, so that we could compare this result to the approximate results one obtains when implementing the Equivalent Photon Approximation (EPA). In chapter 2, after a brief review of the origins and the more recent developments of this approximation, we tackled the task of comparing the full and approximate cross section for the ALP production via VBF. Very soon we realized that the usual methods of integrating the phase space via polar coordinates would not work. In fact, even with the simplification of a completely scalar theory, when considering massive particle it was not possible to have a fully analytical result for the cross section appendix A.
For this reason we reprised an old technique for computing cross sections: Gram Determinants. These mathematical quantities were mostly used in mesons scattering in the '60s and '70s, but are particularly useful in all kinds of processes. Even if we limited ourselves to the case study of a $2 \to 3$ process, these variables can be used for any generic $m \to n$ process with some degree of complication. After relating the usual observables in polar coordinates (like energy and polar angles of particles) to combinations of Gram Determinants in section 2.3.2, we showed how the phase space behaves in our process, and we were able to identify the regions in the phase space which are most populated and contribute the most to the cross section in section 2.3.3. As we expected, in these regions the initial and final leptons are mostly collinear and with similar energies, which is exactly where the EPA is supposed to work.
With this, we were able to finally compute and compare the cross sections for the full process and the approximated one. Given that we were working in the toy scalar theory, we derived the PDF for an "Equivalent Scalar Approximation", with the claim that it is not the Lorentz nature of the particle that decides where the approximation holds (section 2.5). The results showed that the EPA holds up to very high values of the ALP mass, even when very close to $\sqrt{s}$. In fact, in sec-

tion 2.4, we were able to show that as long as the final leptons are ultra-relativistic, there will still be a preference for collinearity, and this property only gets lost when the allowed phase space is so small that the final leptons are non relativistic. This result allows us to extend the range of validity of the EPA in terms of the mass of the produced particle; our result can be combined with the results of Frixione *et al.* in [47], which expressed the goodness of this approximation in terms of the deflection angle of the final leptons with respect to the beam pipe.
Another important conclusion of this first part is that the ALP will mainly be produced at rest, no matter its mass; this is topical for the phenomenological part of this work, focused on the actual production of such a particle at Belle II.

In chapter 3 we started by reproducing the state of the art for ALP searches at Belle II; this work was useful not only to cross check the published results, but also to get a better understanding of the complicated experimental setup; in turn, this preliminar study would become useful when trying to exploit the detector properties (or blind spots, depending on who you ask). After that, in section 3.2 we computed the exclusion bounds for a VBF produced ALP decaying into visible particles. Due to the ECL design, the VBF cross section is actually subleading at Belle II, and the exclusions we obtained were competitive with the state of the art only for very low or very high ALP masses. This is caused by the detector shape: it has a large hole around forward rapidities, basically cutting out the most important region contributing to the VBF. The ALP-strahlung cross section will however decrease faster than the VBF one (and that is why for very large ALP masses we see an increase in sensitivity), and will also be cut by the ECL at very low ALP masses, due to the produced photon being so boosted that they are almost collinear, and not identifiable by the ECL.
Our proposal then is to improve the ECL in order to expand the angular acceptance of leptons, via the use of roman pots for example, that would be able to measure leptons very close to the beam pipe. With this improvement, the VBF exclusion would soon become dominant due to the collinearity enhancement, even with very small efforts in the event selection, as shown in section 3.2.1.
Finally, we studied the decay of a VBF produced ALP into invisible particles (possibly Dark Matter). For this search, we used a **high purity** approach, rather than the high statistics approach used in the literature. In fact, we showed in section 4.1.4 how some cuts in missing energy and rapidity generate a region of the phase space which is inaccessible to the QED background until very high orders in perturbation theory. Combining these cuts with a cut in the final electrons mass m_{ee} allows us to cancel completely also the background coming from $e^+e^- \to \tau^+\tau^-$ (section 4.1.5). This allowed us to obtain background-free exclusion bounds, with the results exposed in section 4.2 and in [61].
This methodology could be extended also to other searches at Belle II, *i.e.* the dark photon, γ'. Some other extensions of this work could come from considering the main peculiarity of Belle II, namely the asymmetricity of the beam energies, used to produce a boosted $\Upsilon(4s)$ in the CoM. In any case, the same high purity search in VBF processes can be conducted at different e^+e^- colliders too; some differences may appear due to the presence of electroweak bosons, if the CoM energy is high enough. All of these interesting investigations however require more time, and will be left to future work.

Appendices

Appendix A

VBF analytical cross section in polar coordinates

Let us expand on the argument of analytical integration of the cross section in eq. (2.38). We arrived at a cross section of the form

$$\begin{aligned}\sigma &= \frac{1}{16sM(2\pi)^4}\int \mathrm{d}\cos\theta_3\mathrm{d}\cos\theta_4\mathrm{d}E_3\mathrm{d}E_4\delta(2m(1+\alpha)-E_3-E_4)\times \\ &\times \frac{p_3}{(2m^2-\sqrt{s}(E_3-\cos\theta_3 p_3\beta))^2}\frac{p_5}{(2m^2-\sqrt{s}(E_4+\cos\theta_4 p_5\beta))^2} = \\ &= \int \mathrm{d}\cos\theta_3\mathrm{d}\cos\theta_4\mathrm{d}E_3 \frac{p_3\sqrt{(2(\alpha+1)m-E_3)^2-m^2}}{256\pi^4 s\left(\sqrt{s}-2(\alpha+1)m\right)\left(2m^2-\sqrt{s}(E_3-\beta\cos\theta_3 p_3)\right)^2}\times \\ &\times \frac{1}{\left(2m^2-\sqrt{s}\left(\beta\cos\theta_4\sqrt{(2(\alpha+1)m-E_3)^2-m^2}-E_3+2(\alpha+1)m\right)\right)^2},\end{aligned} \tag{A.1}$$

where we first integrated in ϕ (integrates to 2π since it does not appear in the integrand) and then we integrated the delta of the energy, substituting $E_4 = 2m(1+\alpha)-E_3$. Remembering that $p_3 = \sqrt{E_3^2-m^2}$, we have in and an irrational integrand in E_3, and the result of this integration is far from trivial. In order to mantain our goal of keeping the calculation as analytical as possible, we refer to the table of integrals [52], in order to see if there are analytical solutions to this integral. An important thing to notice is that in both of the square roots present in the integrand, the argument can be written as a trinomial $a+bE_3+cE_3^2$; in this case, the authors suggest to use the so called "Euler substitutions" in order to get to a rational integral. However, since we have two different square roots, we have to choose which one we want to substitute.
For example, let's keep the simpler square root coming from $p_3 = \sqrt{E_3^2-m^2}$ and let's use the second Euler substitution:

$$\sqrt{(2(\alpha+1)m-E_3)^2-m^2} = \sqrt{A-BE_3+E_3^2},\ A = 4m^2(1+\alpha)^2-m^2,\ B = 4m(1+\alpha) \tag{A.2}$$

$$\sqrt{A-BE_3+E_3^2} = t+E_3 \Rightarrow\ E_3 = \frac{A-t^2}{B+2t},\ \mathrm{d}E_3 = -\frac{2A+2Bt+2t^2}{(B+2t)^2}\mathrm{d}t \tag{A.3}$$

Using this substitution, our integrand function becomes

$$\sigma = \int \mathrm{d}\cos\theta_3 \mathrm{d}\cos\theta_4 \mathrm{d}t \frac{-(A+t(B+t))^2\sqrt{(A-t^2)^2 - m^2(B+2t)^2}}{128\pi^4\left(s^{3/2}-2(\alpha+1)ms\right)} \times$$
$$\times \frac{1}{\left(\beta\cos\theta_3\sqrt{s}\sqrt{(A-t^2)^2 - m^2(B+2t)^2} - A\sqrt{s} + 2Bm^2 + 4m^2t + \sqrt{s}t^2\right)^2} \times$$
$$\times \frac{1}{\left(A\sqrt{s}(\beta\cos\theta_4 - 1) + B\left(\beta\cos\theta_4\sqrt{s}t - 2m^2 + 2(\alpha+1)m\sqrt{s}\right) + t\left(\sqrt{s}t(\beta\cos\theta_4+1) - 4m^2 + 4(\alpha+1)m\sqrt{s}\right)\right)^2} \tag{A.4}$$

Now we are left with only one irrational function; we may think to reapply another Euler substitution to finally reduce to a completely rational function that can then be integrated analytically. The problem is that now the polynomial under the square root is no longer a trinomial, but it is of degree greater than 3. In particular, as explained in [52], if the polynomial under the square root is of degree 3 or 4, the integral can be reduced with some appropriate algebra and substitutions to elliptic integrals; however, this clashes with our original goal: elliptic integrals do not have an analytic form, and can only be evaluated numerically once we specify the integration region.
The reason why we are stuck does not come from the choice of the function to substitute: as we can see in A.3, this substitution doubles the degree of the polynomial under the square root. This means that no matter what we want to substitute, the other root becomes automatically a source for the presence of elliptic integrals, which means that this procedure cannot work for a fully analytical computation of the differential cross section in terms of the angles of the outgoing electrons.

A.1 Expansion for non relativistic electrons

We can also try another route for the analytical integration, which is to start again from 2.38 and to expand the integrand for non relativistic electrons. In order to make as carefully as possible these expansions, let us redefine the integrand by substituting the momentum p_3 with the adimensional quantity

$$q = p_3/m \tag{A.5}$$

This is nothing else but $\beta\gamma$, and since $\gamma \approx 1$ in this context, $q \sim \beta$. Now, if we choose accurately the value of the ALP mass M, we can get to a situation in which this parameter is small and the non relativistic expansion is actually sensible. In particular, we know that in a three body final space the maximal energy for one of the bodies is [62]:

$$E_3^{max} = \frac{s + m^2 - (M+m)^2}{2\sqrt{s}}. \tag{A.6}$$

Now if we consider the electron to be non relativistic, the first order expansion of its energy is

$$E_3 \approx m + \frac{p_3^2}{2m} = m\left(1 + \frac{p_3^2}{2m^2}\right) = m\left(1 + \frac{q^2}{2}\right), \tag{A.7}$$

where we used the definition of eq. (A.5). Finally, we can compare the last two equation, rewriting $M = \sqrt{s} - 2m(1+\alpha)$ and we can find which value of α, and hence of M, allows the outgoing electrons to be non relativistic; namely, we can set for example $q_{max} = 0.1$ and find that $\alpha = 2.5 \cdot 10^{-3}$ (in order for the electrons

to be non relativistic, the alp mass must be different from $\sqrt{s} - 2m$ by less than a hundredth of an electron mass). This shows how close to the end of the phase space one needs to go to have the EPA fail completely.
Now that we have the numerical values, we can substitute every energy with the adimensional small parameter q and then expand the result. It is important to note that in expanding the electron energy at first order, we are neglecting everything that is of $\mathcal{O}\left(\frac{p^4}{m^4}\right) = \mathcal{O}(q^4)$, which means that we can only expand the integrand up to q^3 in order to be sure of the result. After the substitution of eq. (A.7), the integral for the cross section of eq. (A.4) becomes

$$\sigma = \int \mathrm{d}\cos\theta_3 \mathrm{d}\cos\theta_4 \mathrm{d}q \frac{1}{32\pi^4\left(s^{3/2} - 2(\alpha+1)ms\right)} \times \frac{q^2}{\left(\sqrt{s}\left(-2\beta\cos\theta_3 q + q^2 + 2\right) - 4m\right)^2} \times$$
$$\times \frac{\sqrt{m^2\left(16(\alpha+1)\alpha + q^4 - 4(2\alpha+1)q^2\right)}}{\left(\beta\cos\theta_4\sqrt{s}\sqrt{m^2\left(16(\alpha+1)\alpha + q^4 - 4(2\alpha+1)q^2\right)} - 4m^2 + m\sqrt{s}\left(4\alpha - q^2 + 2\right)\right)^2} \tag{A.8}$$

Now we can expand in the small parameter q: notice that A.8 contains q^2 in the numerator by itself, so the leading order of this expansion is $\mathcal{O}(q^2)$. If we plot the behaviour of the differential cross section as a function of the outgoing angles, result obtained after integrating in q the expanded cross section A.8, we get the following plots:

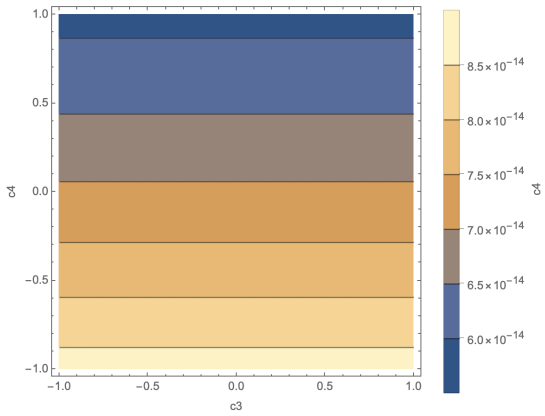

Figure A.1. $\mathcal{O}(q^2)$ expansion

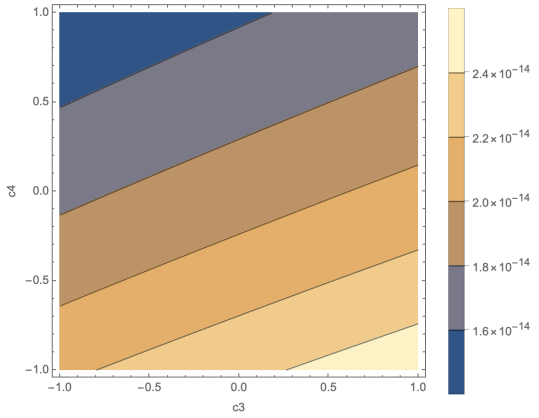

Figure A.2. $\mathcal{O}(q^3)$ expansion

On the two axes lie the values of the cosine of the outgoing angles, while the color stands for the amount of cross section there is in each point. At a first glance, it seems that at leading order there is a very big asymmetry between the two cosines: the cross section seems to be isotropic in $\cos\theta_3$ but not in $\cos\theta_4$. This however is unavoidable, because we chose to integrate away E_4 with the delta, so $\cos\theta_4$ in the propagator now multiplies a different term than $\cos\theta_3$ (see for example in A.8), and this means that in the expansion there will be different powers of q multiplying the two cosines.
This situation should however go away when considering higher powers of the expansion, and looking at the next order it actually seems the case (as shown in fig. A.2). There is nevertheless a bigger problem lurking: if we look at the values

of the cross section for the "leading order" and for the next correction, there is basically a factor of 4 of difference between the two of them: this is not a good sign, because the truncation of the series makes sense only if the remainder of said series is much smaller than the terms that are kept. This sudden change has an easy explanation: going back to A.8, we can see that under the square root that we are expanding, the coefficient of q^0 is $16\alpha(\alpha+1) \sim 10 \times \mathcal{O}(\alpha)$, while the coefficient of q^2 is $4(1+2\alpha) \sim \mathcal{O}(1)$. But with our numerical values, $q^2_{max} \sim 10\alpha$: this means that the expansion of the square root truncated at low orders is a very bad approximation of said square root, hence the bad results for the series.
To try and avoid this result, we should go to higher orders in the expansion; in order to do so, we also need to expand the non relativistic energy of the electron to higher orders. But this is not all: in fact, to mitigate this kind of behavior, we can also "avoid" the region of the phase space which can cause troubles. Practically, we can choose to integrate q only around its median value instead that in all of the region: since this cancellation happens only when q is close to its maximum, we can restrict the integration region from $[0, q_{max}]$ to $\left[\frac{q_{max}}{4}, \frac{3q_{max}}{4}\right]$. This is analogous to the situation in which our detector can only reveal particles in a certain range of energy, or in which we have a cut in the energy of the final leptons.
For the sake of brevity, we will not rewrite here each of the expansions and the partial results; it is simply a matter of putting the initial function into `Mathematica` and make it expand up to the needed order. Instead, in the figures below, there will be posted the plots of the cross section for higher and higher orders; as we can see, after the expansion up to q^4 the series seems to behave better than before. However, the problem of the cancellations among the first two terms in the square root, that forces us to go to such high orders, makes this kind of computation not so advantageous.

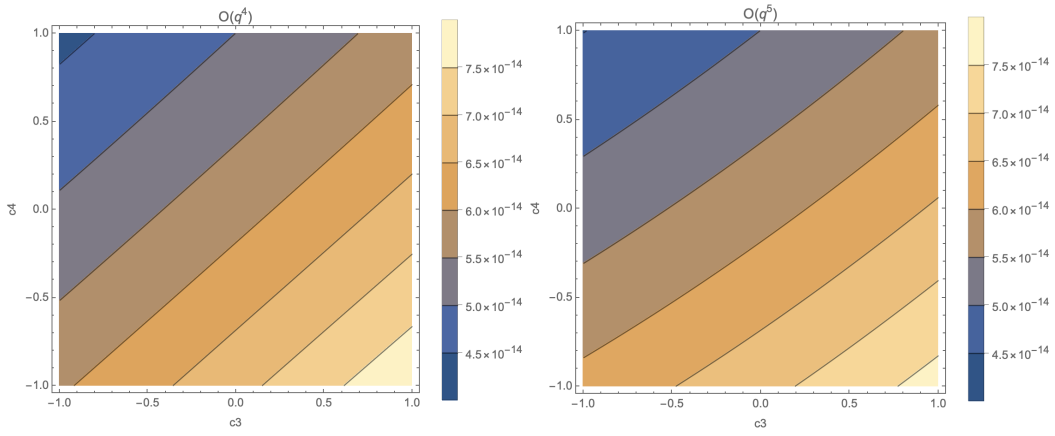

Figure A.3. $\mathcal{O}(q^4)$ expansion

Figure A.4. $\mathcal{O}(q^5)$ expansion

A.2 Ultrarelativistic electrons, non relativistic ALP

Since the electrons are so light, and, as we saw, in order to make them non relativistic the mass of the alp must almost close completely the phase space; we can

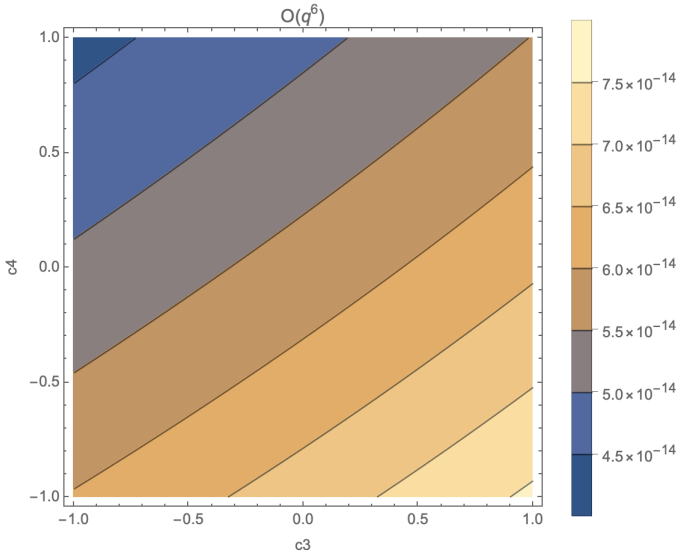

Figure A.5. $\mathcal{O}(q^6)$ expansion

also consider a less narrow region of the phase space in which the alp is still non relativistic, but the final state electrons are, and as so we can consider them to be massless. In order to get to the differential cross section we can do exactly the same procedure as before, just putting $m = 0$. Then, in the end, we get to

$$\frac{\mathrm{d}\sigma}{\mathrm{d}\cos\theta_3 \mathrm{d}\cos\theta_4 \mathrm{d}E_3} = \frac{1}{256\pi^4 E_3 M s^3 (\beta\cos\theta_3 - 1)^2 (\beta\cos\theta_4 + 1)^2 \left(\sqrt{s} - E_3 - M\right)}. \tag{A.9}$$

This is a simple rational integral; however, it is clearly divergent for $E_3 = 0$, which is the well known soft divergence. In order to avoid it, without computing any of the following orders corrections, let us put a cutoff on the electron energy and reintroduce by hand the mass of the electron: now the minimal energy is m, and the divergence in energy no longer exists.

$$\frac{\mathrm{d}\sigma}{\mathrm{d}\cos\theta_3 \mathrm{d}\cos\theta_4} = \log\left(\frac{\left(s-2mM-M^2\right)\left(s-2m\sqrt{s}-M^2\right)}{4m^2 M\sqrt{s}}\right) \times \tag{A.10}$$

$$\times \frac{1}{128\pi^4(\cos\theta_3-1)^2(\cos\theta_4+1)^2 s^3 (s-M^2)} \tag{A.11}$$

As expected, since this case can be assimilated to the EPA framework, there is a clear, strong preference for the collinearity of the final state electrons to the beam axis, namely

$$c_3 \to 1,\ c_4 \to -1. \tag{A.12}$$

A.3 Smearing algorithm

If we want to analyze events containing missing particles, we need to include detector effects into our computations. For a process of the type

$$e^+e^- \to e^+e^- + \text{ inv}, \tag{A.13}$$

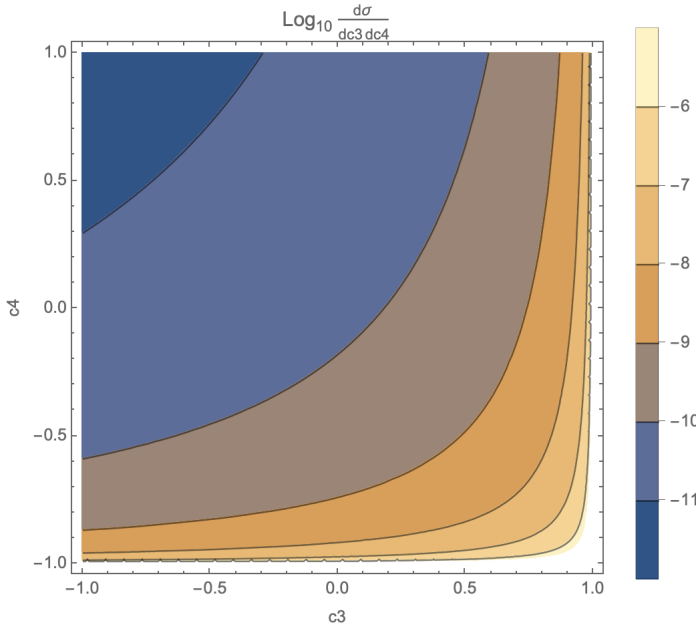

Figure A.6. Non relativistic ALP with ultrarelativistic electrons

the visible leptons have MC generated energy and momentum with "infinite" precision. This is not the case for a real detector; in particular, we can expect some uncertainty in the measurements of the energy and the angle of visible particles. After generating the MC events, we apply the following algorithm to our data:

- Only the final leptons are smeared in energy, polar angle and azimuthal angle. Each MC generated quantity x, with $x \in [E, \theta, \phi]$ becomes a smeared quantity x^s extracted randomly from a normal distribution of mean value x and standard deviation σ_x.

- We assume the uncertainty on the angles to be small and constant, namely

$$\sigma_\theta = \sigma_\phi = 10^{-3}. \tag{A.14}$$

  The uncertainty on the energy comes from the ECL, and reads

$$\frac{\sigma_E}{E} = \sqrt{\left(\frac{0.066\%}{E}\right)^2 + \left(\frac{0.81\%}{\sqrt[4]{E}}\right)^2 + (1.34\%)^2}. \tag{A.15}$$

  Using the smeared x^s, we write the smeared lepton 4-momenta and check that these are still inside the acceptance of Belle II (we need them to be visible). After this check, we can write the smeared visible total momentum,

$$p^s_{vis} = p^s_{e^+} + p^s_{e^-} \tag{A.16}$$

- We define an invisible event assuming total 4-momentum conservation (and using the original incoming 4-momenta):

$$p_{inv} = p_{in} - p^s_{vis}. \tag{A.17}$$

Since the smearing is a probabilistic process, it may happen that a kinematic point originally outside of our cuts fluctuates inside the acceptance region. For this reason, our MC generation will use some broader cuts than the actual Belle II acceptance; after the smearing procedure, we will only retain events that actually are insibe of Belle II acceptance.

Bibliography

[1] **ATLAS** Collaboration, G. Aad et al., *Observation of a new particle in the search for the Standard Model Higgs boson with the ATLAS detector at the LHC*, *Phys. Lett.* **B716** (2012) 1–29, [arXiv:1207.7214].

[2] **CMS** Collaboration, S. Chatrchyan et al., *Observation of a new boson at a mass of 125 GeV with the CMS experiment at the LHC*, *Phys. Lett.* **B716** (2012) 30–61, [arXiv:1207.7235].

[3] S. L. Glashow, *Partial Symmetries of Weak Interactions*, *Nucl. Phys.* **22** (1961) 579–588.

[4] A. Salam, *Weak and Electromagnetic Interactions*, *Conf. Proc.* **C680519** (1968) 367–377.

[5] S. Weinberg, *A Model of Leptons*, *Phys. Rev. Lett.* **19** (1967) 1264–1266.

[6] R. J. Crewther, P. Di Vecchia, G. Veneziano, and E. Witten, *Chiral Estimate of the Electric Dipole Moment of the Neutron in Quantum Chromodynamics*, *Phys. Lett. B* **88** (1979) 123. [Erratum: Phys.Lett.B 91, 487 (1980)].

[7] L. D. Luzio, M. Giannotti, E. Nardi, and L. Visinelli, *The landscape of QCD axion models*, *Physics Reports* **870** (jul, 2020) 1–117.

[8] A. Hook, *Tasi lectures on the strong cp problem and axions*, 2021.

[9] R. D. Peccei and H. R. Quinn, *CP Conservation in the Presence of Instantons*, *Phys. Rev. Lett.* **38** (1977) 1440–1443.

[10] S. Weinberg, *A new light boson?*, *Phys. Rev. Lett.* **40** (Jan, 1978) 223–226.

[11] F. Wilczek, *Problem of Strong P and T Invariance in the Presence of Instantons*, *Phys. Rev. Lett.* **40** (1978) 279–282.

[12] J. E. Kim, *Weak Interaction Singlet and Strong CP Invariance*, *Phys. Rev. Lett.* **43** (1979) 103.

[13] M. A. Shifman, A. I. Vainshtein, and V. I. Zakharov, *Can Confinement Ensure Natural CP Invariance of Strong Interactions?*, *Nucl. Phys. B* **166** (1980) 493–506.

[14] M. Dine, W. Fischler, and M. Srednicki, *A Simple Solution to the Strong CP Problem with a Harmless Axion*, *Phys. Lett. B* **104** (1981) 199–202.

[15] A. R. Zhitnitsky, *On Possible Suppression of the Axion Hadron Interactions. (In Russian)*, *Sov. J. Nucl. Phys.* **31** (1980) 260.

[16] C. O'Hare, "cajohare/axionlimits: Axionlimits." `https://cajohare.github.io/AxionLimits/`, July, 2020.

[17] D. Cadamuro and J. Redondo, *Cosmological bounds on pseudo nambu-goldstone bosons*, *Journal of Cosmology and Astroparticle Physics* **2012** (feb, 2012) 032–032.

[18] P. Arias, D. Cadamuro, M. Goodsell, J. Jaeckel, J. Redondo, and A. Ringwald, *WISPy cold dark matter*, *Journal of Cosmology and Astroparticle Physics* **2012** (jun, 2012) 013–013.

[19] F. Chadha-Day, J. Ellis, and D. J. E. Marsh, *Axion dark matter: What is it and why now?*, 2022.

[20] M. J. Dolan, F. Kahlhoefer, C. McCabe, and K. Schmidt-Hoberg, *A taste of dark matter: Flavour constraints on pseudoscalar mediators*, *JHEP* **03** (2015) 171, [`arXiv:1412.5174`]. [Erratum: JHEP 07, 103 (2015)].

[21] Y. Nomura and J. Thaler, *Dark Matter through the Axion Portal*, *Phys. Rev. D* **79** (2009) 075008, [`arXiv:0810.5397`].

[22] C. Boehm, M. J. Dolan, C. McCabe, M. Spannowsky, and C. J. Wallace, *Extended gamma-ray emission from Coy Dark Matter*, *JCAP* **05** (2014) 009, [`arXiv:1401.6458`].

[23] M. Millea, L. Knox, and B. D. Fields, *New bounds for axions and axion-like particles with keV-GeV masses*, *Physical Review D* **92** (jul, 2015).

[24] M. Giannotti, I. Irastorza, J. Redondo, and A. Ringwald, *Cool WISPs for stellar cooling excesses*, *JCAP* **05** (2016) 057, [`arXiv:1512.08108`].

[25] K. Mimasu and V. Sanz, *ALPs at Colliders*, *JHEP* **06** (2015) 173, [`arXiv:1409.4792`].

[26] J. Jaeckel and M. Spannowsky, *Probing MeV to 90 GeV axion-like particles with LEP and LHC*, *Phys. Lett. B* **753** (2016) 482–487, [`arXiv:1509.00476`].

[27] B. Döbrich, J. Jaeckel, F. Kahlhoefer, A. Ringwald, and K. Schmidt-Hoberg, *ALPtraum: ALP production in proton beam dump experiments*, *JHEP* **02** (2016) 018, [`arXiv:1512.03069`].

[28] E. Izaguirre, T. Lin, and B. Shuve, *Searching for Axionlike Particles in Flavor-Changing Neutral Current Processes*, *Phys. Rev. Lett.* **118** (2017), no. 11 111802, [`arXiv:1611.09355`].

[29] S. Knapen, T. Lin, H. K. Lou, and T. Melia, *Searching for Axionlike Particles with Ultraperipheral Heavy-Ion Collisions*, *Phys. Rev. Lett.* **118** (2017), no. 17 171801, [`arXiv:1607.06083`].

[30] I. Brivio, M. B. Gavela, L. Merlo, K. Mimasu, J. M. No, R. del Rey, and V. Sanz, *ALPs Effective Field Theory and Collider Signatures*, *Eur. Phys. J. C* **77** (2017), no. 8 572, [arXiv:1701.05379].

[31] M. Bauer, M. Neubert, and A. Thamm, *Collider Probes of Axion-Like Particles*, *JHEP* **12** (2017) 044, [arXiv:1708.00443].

[32] M. Bauer, M. Neubert, and A. Thamm, *LHC as an Axion Factory: Probing an Axion Explanation for $(g-2)_\mu$ with Exotic Higgs Decays*, *Phys. Rev. Lett.* **119** (2017), no. 3 031802, [arXiv:1704.08207].

[33] K. Choi, S. H. Im, C. B. Park, and S. Yun, *Minimal Flavor Violation with Axion-like Particles*, *JHEP* **11** (2017) 070, [arXiv:1708.00021].

[34] D. Chang, W.-F. Chang, C.-H. Chou, and W.-Y. Keung, *Large two loop contributions to g-2 from a generic pseudoscalar boson*, *Phys. Rev. D* **63** (2001) 091301, [hep-ph/0009292].

[35] W. J. Marciano, A. Masiero, P. Paradisi, and M. Passera, *Contributions of axionlike particles to lepton dipole moments*, *Phys. Rev. D* **94** (2016), no. 11 115033, [arXiv:1607.01022].

[36] T. Flacke, C. Frugiuele, E. Fuchs, R. S. Gupta, and G. Perez, *Phenomenology of relaxion-Higgs mixing*, *JHEP* **06** (2017) 050, [arXiv:1610.02025].

[37] P. W. Graham, D. E. Kaplan, and S. Rajendran, *Cosmological Relaxation of the Electroweak Scale*, *Phys. Rev. Lett.* **115** (2015), no. 22 221801, [arXiv:1504.07551].

[38] A. Arvanitaki, S. Dimopoulos, S. Dubovsky, N. Kaloper, and J. March-Russell, *String axiverse*, *Physical Review D* **81** (jun, 2010).

[39] B. Bellazzini, A. Mariotti, D. Redigolo, F. Sala, and J. Serra, *R-axion at colliders*, *Physical Review Letters* **119** (oct, 2017).

[40] M. J. Dolan, T. Ferber, C. Hearty, F. Kahlhoefer, and K. Schmidt-Hoberg, *Revised constraints and Belle II sensitivity for visible and invisible axion-like particles*, *JHEP* **12** (2017) 094, [arXiv:1709.00009]. [Erratum: JHEP 03, 190 (2021)].

[41] T. e. a. Abe, *Belle ii technical design report*, 2010.

[42] E. Fermi, *On the theory of collisions between atoms and electrically charged particles*, *Nuovo Cimento* **2** (05, 2002) [0205086v1].

[43] C. F. von Weizsacker, *Radiation emitted in collisions of very fast electrons*, *Z. Phys.* **88** (1934) 612–625.

[44] E. J. Williams, *Correlation of certain collision problems with radiation theory*, *Kong. Dan. Vid. Sel. Mat. Fys. Med.* **13N4** (1935), no. 4 1–50.

[45] R. H. Dalitz and D. R. Yennie, *Pion production in electron-proton collisions*, *Physical Review* **105** (1957), no. 5 1598–1615.

[46] V. M. Budnev, I. F. Ginzburg, G. V. Meledin, and V. G. Serbo, *The Two photon particle production mechanism. Physical problems. Applications. Equivalent photon approximation*, *Phys. Rept.* **15** (1975) 181–281.

[47] S. Frixione, M. L. Mangano, P. Nason, and G. Ridolfi, *Improving the Weizsacker-Williams approximation in electron - proton collisions*, *Phys. Lett. B* **319** (1993) 339–345, [hep-ph/9310350].

[48] K. Kajantie and P. Lindblom, *Physical region on the plane of two invariant momentum transfers for a reaction with three particles in the final state*, *Phys. Rev.* **175** (Nov, 1968) 2203–2213.

[49] E. Byckling and K. Kajantie, *Particle Kinematics: (Chapters I-VI, X)*. University of Jyvaskyla, Jyvaskyla, Finland, 1971.

[50] N. BYERS and C. N. YANG, *Physical regions in invariant variables for n particles and the phase-space volume element*, *Rev. Mod. Phys.* **36** (Apr, 1964) 595–609.

[51] M. E. Peskin and D. V. Schroeder, *An Introduction to Quantum Field Theory*. Westview Press, 1995. Reading, USA: Addison-Wesley (1995) 842 p.

[52] I. S. Gradshteyn, I. M. Ryzhik, D. Zwillinger, and V. Moll, *Table of integrals, series, and products; 8th ed.* Academic Press, Amsterdam, Sep, 2014.

[53] E. K. et al., *The belle II physics book*, *Progress of Theoretical and Experimental Physics* **2019** (dec, 2019).

[54] V. Aulchenko, A. Bobrov, A. Bondar, B. Cheon, S. Eidelman, D. Epifanov, Y. Garmash, Y. Goh, S. Kim, P. Krokovny, A. Kuzmin, I. Lee, D. Matvienko, K. Miyabayashi, I. Nakamura, V. Shebalin, B. Shwartz, Y. Unno, and V. Zhulanov, *Electromagnetic calorimeter for belle ii*, *Journal of Physics: Conference Series* **587** (02, 2015).

[55] A. Alloul, N. D. Christensen, C. Degrande, C. Duhr, and B. Fuks, *FeynRules 2.0 — a complete toolbox for tree-level phenomenology*, *Computer Physics Communications* **185** (aug, 2014) 2250–2300.

[56] J. Alwall, R. Frederix, S. Frixione, V. Hirschi, F. Maltoni, O. Mattelaer, H.-S. Shao, T. Stelzer, P. Torrielli, and M. Zaro, *The automated computation of tree-level and next-to-leading order differential cross sections, and their matching to parton shower simulations*, *Journal of High Energy Physics* **2014** (jul, 2014).

[57] U. Amaldi et al., *Measurements of the proton proton total cross-sections by means of Coulomb scattering at the Cern intersecting storage rings*, *Phys. Lett. B* **43** (1973) 231–236.

[58] S. A. K. et al., *The alfa roman pot detectors of atlas*, *Journal of Instrumentation* **11** (nov, 2016) P11013.

[59] K. A. et al., *Lhc forward physics*, *Journal of Physics G: Nuclear and Particle Physics* **43** (oct, 2016) 110201.

[60] T. Han, I.-W. Kim, and J. Song, *Kinematic cusps: Determining the missing particle mass at colliders*, *Physics Letters B* **693** (oct, 2010) 575–579.

[61] F. Acanfora, R. Franceschini, A. Mastroddi, and D. Redigolo, *Fusing photons into nothing, a new search for invisible ALPs and Dark Matter at Belle II*, `arXiv:2307.06369`.

[62] T. HAN, *COLLIDER PHENOMENOLOGY: BASIC KNOWLEDGE AND TECHNIQUES*, in *Physics In D ≥ 4 Tasi 2004*, WORLD SCIENTIFIC, jul, 2006.